BIOPHYSICAL CHARACTERIZATION OF ZIKA VIRUS TERMINAL REGION INTERACTIONS

LIAM ANDREW KERR
Bachelor of Science, University of Lethbridge, 2023

A thesis submitted
in partial fulfilment of the requirements for the degree of

MASTER OF SCIENCE

in

BIOCHEMISTRY

Department of Chemistry and Biochemistry
University of Lethbridge
LETHBRIDGE, ALBERTA, CANADA

BIOPHYSICAL CHARACTERIZATION OF ZIKA VIRUS TERMINAL REGION INTERACTIONS

LIAM KERR

Date of Defence: August 5, 2025

Dr. Trushar Patel	Professor	Ph.D.
Thesis Supervisor		
Dr. Borries Demeler	Professor	Ph.D.
Thesis Examination Committee Member		
Dr. Steve Wiseman	Associate Professor	Ph.D.
Thesis Examination Committee Member		
Dr. Dylan Girodat	Assistant Professor	Ph.D.
Chair, Thesis Examination Committee		

Abstract

Recent viral threats have intensified research into viral mechanisms and the various interactions during their viral life cycle. Viruses such as Zika virus have continued to threaten healthcare systems around the globe, with large outbreaks affecting over 3 million people within the last decade. While viral proteins have received significant attention, the untranslated terminal regions (TRs) flanking the single-stranded RNA genome play crucial roles in the viral life cycle. These TRs facilitate replication through interactions with host/viral proteins and through self-association via cyclization, which regulates transcription and translation. This thesis characterizes the biophysical and cellular properties of this cyclization interaction and the TRs interaction with the host protein FXR1. Using size exclusion multi-angle light scattering and analytical ultracentrifugation, we defined the hydrodynamic profiles of the TRs and FXR1. Microscale thermophoresis quantified the affinity and specificity of the TRs cyclization interaction, as well as the affinity of FXR1 for the TRs. Cellular studies further demonstrated that TR mutations disrupting cyclization drastically reduce viral replication. Collectively, this work identifies a sequence specific interaction governing Zika virus replication and establishes a foundation for characterizing the TR-FXR1 interaction, offering potential targets for future therapeutic development.

Contribution of Authors

Chapter 2 is a collaborative manuscript prepared for journal submission. The work for the chapter was contributed by Danielle Gemmill, Dr. Higor Pereira, Dr. Michael Wolfinger, and Dr. Trushar. I conducted all wet laboratory experiments and cellular studies, as well as designing of constructs and replicon mutations. Danielle Gemmill assisted in the construction design and initial interaction studies. Dr. Pereira assisted in cellular studies, while Dr. Wolfinger performed the *in silico* analysis of the terminal regions. I wrote the manuscript with input and editing assistance from Dr. Pereira, Dr. Wolfinger, and Dr. Patel.

Chapter 3 contains unpublished work completed with assistance from Sierra Mazurek, Aysha Demeler, and Dr. Trushar Patel. I performed all wet laboratory experiments with assistance from Sierra Mazurek. AUC experiments were performed and analysed by Aysha Demeler. Jack Moore at the Alberta Proteomics and Mass Spectrometry Facility at the University of Alberta performed Mass spectroscopy analysis for verification. I have written the manuscript with the assistance of editing from Dr. Patel.

Acknowledgements

I would like to thank my supervisor, Dr. Trushar Patel, for the opportunity to conduct this research, which I have come to love. Especially for taking me in as an undergraduate student when I was uncertain about my scientific future, the opportunity you provided me, both as an undergraduate and now as a master's student, has made me certain and confident in my future as a researcher. Thank you to all the Patel lab members and L9Q1, you have been a great support and made work such a great place to be. I'm very thankful for the friendships I have made during my time here, they are some I will cherish and remember forever. Especially thanks to Sierra Mazurek, who was a huge help and dedicated during the endless protein purifications.

Thank you to my committee members, Dr. Borries Demeler and Dr. Steve Wiseman, for the advice and encouragement.

Thank you to everyone who has provided me with help and mentorship. Specifically, Danielle Gemmill, you taught me so much during my undergraduate studies, and I know that without the knowledge I gained from you, I wouldn't be where I am as a researcher today. Thank you to Jason Luddu and Dr. Higor Pereria for teaching me the ways of cell culturing.

A special thank you to my parents, who have always supported me and been so encouraging. A huge thank you to my friends, particularly Tyler and Sam, who have been there to put up with me getting snacks late at night since the beginning of my undergraduate studies. Lastly, to SarahAnn, Jason, Aysha, Ash, and Reece, your friendship and support have done more for me than you will ever know. I thank you all from the bottom of my heart and can't wait to see where we all end up in life. You all made my time during my master's better than I ever could have imagined.

Table of Contents **Page**

List of Tables **Page**

List of Figures **Page**

List of Abbreviations

(+)ssRNA	single stranded positive-sense RNA
3' SL	3' stem loop
AUC	analytical ultracentrifugation
AUG	translational start codon
C	capsid
cHP	capsid coding region hair pin
Comp	compensatory
CS	cyclization sequence
DAR	downstream AUG region
DENV	Dengue virus
dn/dc	refractive index increment factor
DNA	deoxyribonucleic acid
E	envelope
EMSA	electrophoretic mobility shift assay
ER	endoplasmic reticulum
FMRP	fragile X mental retardation protein 1
FXR1	fragile X-related protein 1
GTP	guanosine triphosphate
HPF	Zika virus Asian H/PF/2013 strain
Huh7	human hepatoma cell line
IFN	interferon
IPTG	isopropyl β-D-1-thiogalactopyranoside
IVT	in vitro transcritption
JAK	Janus associated kinases
JEV	Japanese Encephalitis virus
K_d	dissociation constant
LB	luria broth
LLPS	liquid-liquid phase seperation

LS	light scattering
M	membrane protein
mAU	milli absorbance units
miRNA	microRNA
MR766	Zika virus African MR766 strain
mRNA	messenger RNA
MST	microscale thermophoresis
Mut	mutant
Mw	molecular weight
NS	non-structural protein
nt	nucleotide
PAGE	polyacrylamide gel electrophoresis
PBS	phosphate buffered saline
PBST	phosphate buffered saline with tween
poly(U)	poly(uridine)
prM	pre-membrane
RI	refractive index
RLuc	*renilla* luciferase
RNA	ribonucleic acid
RO	replication organelle
rpm	revolutions per minute
S200	superdex 200 increase GL 10/300
SDS	sodium dodecyl sulfate
SEC	size exclusion chromatography
SEC-MALS	size exclusion multi-angle light scattering
sfRNA	subgenomic flaviviral RNA
siRNA	small interfering RNA
SLA	5' stem loop A
SLB	5' stem loop B
STAT	signal transducers and activation of transcription

SV- AUC	sedimentation velocity analytical ultracentrifugation
TAM	receptor tyrosine kinases, TYRO 3, AXL, and MER
TB	terrific broth
TIM	T- Cell immunoglobulin mucin
TR	terminal region
UAR	upstream AUG region
UTR	untranslated terminal region
WNV	West Nile virus
WT	wild-type
YFV	Yellow Fever virus
ZIKV	Zika virus

Chapter 1: Introduction and Background to Zika Virus

1.1- Flaviviruses

Flaviviruses are single-stranded positive-sense RNA (+ssRNA) viruses that belong to the *Flaviviridae* family, which replicate within arthropods as well as vertebrates such as monkeys and humans (1). With various prominent viruses such as Zika (ZIKV), Dengue (DENV), West Nile (WNV), Japanese Encephalitis (JEV), and Yellow Fever (YFV), being circulated widely across the globe, the chance of contracting one of these flaviviruses is high (2). This is further exacerbated by increasing global temperatures, which enable the primary vector of mosquitoes to migrate further north, thereby increasing the risk to more countries. These viruses pose ongoing global health threats due to the ease of transmission from their mosquito reservoirs, as well as the lack of effective therapeutics or antivirals available (3).

Flaviviruses have an ssRNA genome of approximately 10,000 - 11,000 nucleotides (nts) in length, which is enclosed within a glycoprotein envelope and an icosahedral capsid. Located at either the 5' or 3' end of the genome are the untranslated terminal regions (TR), with a 5′ methyl cap (4). These two TRs flank the coding region for a polyprotein that produces the 3 structural proteins in order of the capsid (C), pre-membrane (prM), and envelope (E), as shown in **Figure 1.1** (5, 6). It also encodes the 7 non-structural proteins (NS1, NS2A, NS2B, NS3, NS4A, NS4B, NS5)(5). The C protein is responsible for forming the viral capsid, which protects the genome. In contrast, the prM, which then matures to membrane protein (M), acts as a chaperone to help fold and spatially organize the E protein, which then forms the final envelope to contain the capsid, as well as facilitating further cell entry (7, 8). This final envelope formation is crucial for producing infectious particles, and the capsid formation must select viral RNA to package while excluding other cellular RNA (9–11). Of these several non-structural proteins, different roles are attributed

to them during viral replication (12). The NS1 protein is a multifunctional component of viral replication, involved in both particle assembly and host immune evasion (13–16). Existing in various oligomeric states and, when in its dimeric form, it is often found to co-localize with double-stranded RNA, as well as other proteins such as NS4A and NS4B. This is believed to indirectly support viral replication, as it is separated from the replication machinery (13, 17). NS2A and NS2B have demonstrated an integral role in viral assembly. While both transmembrane proteins are found within replication organelles, they exhibit very different modes of action. Through recent studies, NS2A has been identified to recruit the C-prM-E polyproteins, viral RNA, and the NS2B-NS3 complex to virion assembly complexes (8, 18, 19). It is also believed that NS2A plays a crucial role in selecting viral RNA for packaging through interactions with the 3' TR (18, 19). NS2B is integral as it serves as a cofactor for NS3, which then allows NS3 to be anchored to the ER within the replication compartments. This forms the active complex of NS2B-NS3, where it is needed for RNA unwinding during replication (20). NS3 is a crucial multifunctional enzyme that is responsible for the proteolytic cleavage of the polyprotein with its serine protease at the N-terminal domain, as well as double-stranded RNA unwinding by its helicase domain located at the C-terminus (8, 20–23). While acting as a cofactor for NS3, NS2B also interferes with Janus Associated Kinases (JAK) and Signal Transducers and Activation of Transcription (STAT) or JAK/STAT signaling pathways by promoting JAK1 degradation through the NS2B-NS3 complex. Additionally, type I interferons (IFN) were found to target NS2B-NS3 for degradation, demonstrating its critical role during viral replication (24). NS4A and NS4B have been identified as the key proteins driving the formation of ER replication organelles, inducing curvature through the assistance of host proteins (25, 26). They have also exhibited immune-inhibitory properties, inhibiting IFN activity (8, 27–33). Lastly, NS5, the largest of the viral proteins and most conserved

across flaviviruses, contains two enzymatic domains, allowing it to act as an RNA-dependent RNA polymerase with its C-terminal domain. In contrast, its N-terminal domain functions as a methyltransferase that caps newly synthesized viral genomes (5, 34, 35). Additionally, NS5 actively inhibits immune response by targeting STAT2, a key signalling molecule in IFN pathways, for proteasomal degradation, which then inhibits IFN signalling and facilitates viral evasion of host immune responses (36, 37).

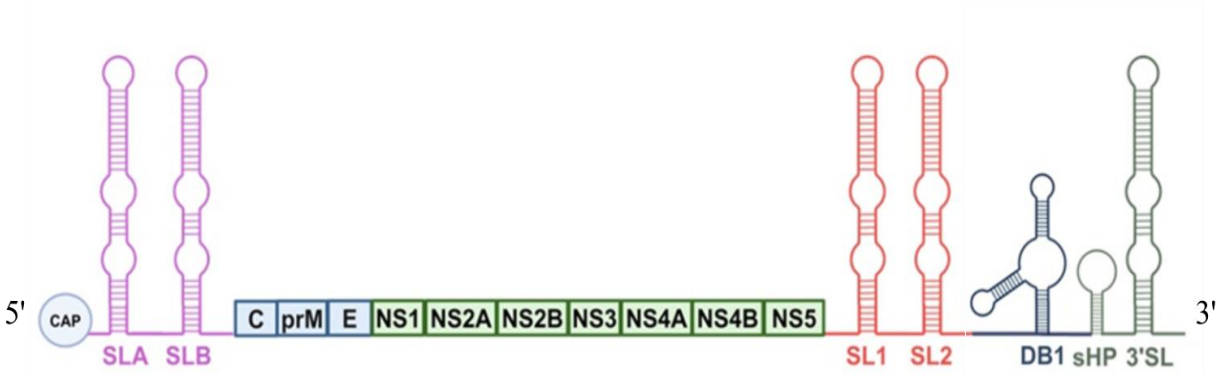

Figure 1.1: Representation of Flavivirus genome. The ~11knt genome is comprised of a single open reading frame flanked by the structural untranslated terminal regions. The three structural proteins highlighted in blue are the capsid (C), pre-membrane (prM) and envelope (E). While the 7 non-structural are highlighted in green.

1.2- Zika Virus

ZIKV is a neuroinvasive member of the flavivirus family, discovered in the Zika forest of Uganda in 1947. Like many other members, it is transmitted through mosquito vectors such as *Aedes aegypti* and *Aedes albopictus* (38, 39). ZIKV is divided into three main lineages based on the coding region: East African, West African, and Asian. Of these three, through whole-genome sequencing, the African strains can be grouped, producing two distinct lineages: the Asian and the African (39–42). Differences in replication and immune responses between the lineages have been observed to be linked to slight differences in structural genes, which have been speculated to be the basis of the higher virulence observed in African strains (43–45). Interestingly, of the most

recent epidemics of Yap State, French Polynesia, and Brazil in 2007, 2013, and 2015, respectively, were caused by strains from the Asian lineage, suggesting that increased virulence by the African lineages doesn't equate to higher epidemic potential by ZIKV (44–46). This is also evident in strains such as H/PF/2013, which demonstrates the ability to develop more severe congenital malformations than those of African lineages (47). During these epidemics, 11% of the population of French Polynesia, or roughly 30,000 people, sought medical treatment for ZIKV infection, while an estimated 1.3 million people contracted ZIKV during the epidemic in Brazil (38, 39, 48–54). Because *Aedes aegypti* and *Aedes albopictus* mosquitoes are present in 26 U.S. states, reaching as far north as Michigan, there is significant concern for autochthonous cases of ZIKV. Although secondary transmission has only been documented in Florida, changing climate conditions are increasing the potential for further spread (40, 49, 55). Using data provided from the Centers for Disease Control as of May 2024 (56), **Figure 1.2** represents a map of countries with current or

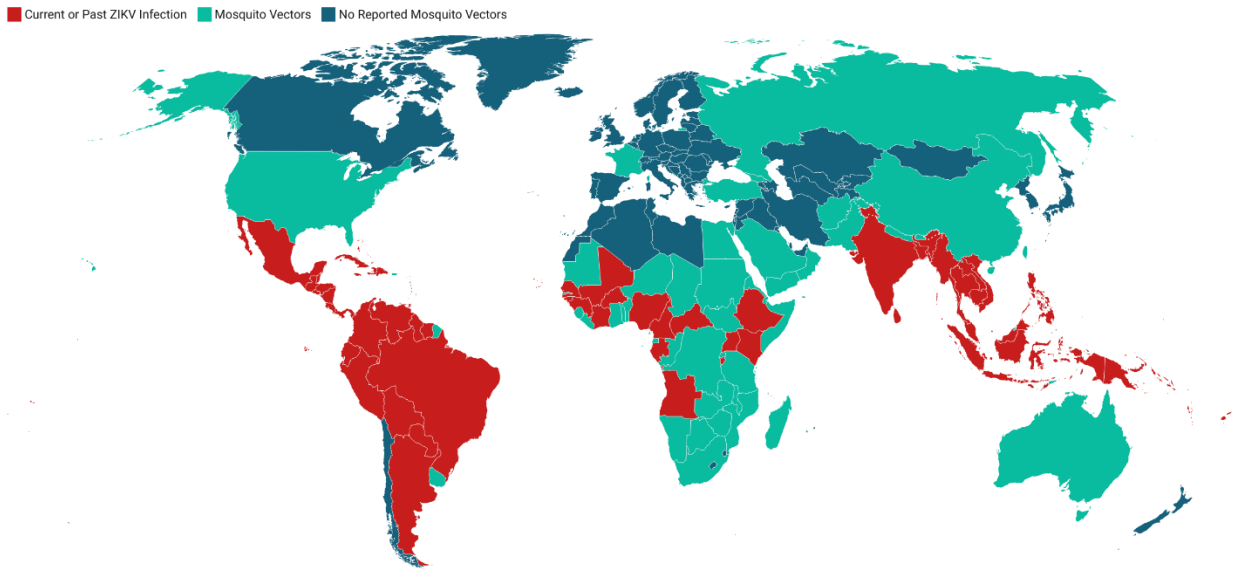

Figure 1.2: Global coverage of Zika infection and risk. Red depicts regions that have had current or past infection of Zika, while green represent regions where mosquito vectors have been identified, while blue has not reported any mosquito vectors. Source: Centers for Disease Control https://www.cdc.gov/zika/geo/index.html

previous infection as well as various other countries that are at risk due to known mosquito vectors within the country.

As previously mentioned, transmission occurs primarily through mosquito vectors. However, it can also be spread via sexual contact, blood transfusions, and, although uncommon, through other forms of direct skin contact or mucous membranes (39, 40, 52, 57). The viral genome is contained within an enveloped sphere with a diameter of approximately 50 nm (58–60). Once viral particles enter the bloodstream, a variety of cell types are susceptible to recognition and entry, including those in the reproductive tract, cerebral cortex, and hippocampus (57, 61, 62). Depending on the maturity of the viral particles, there is a difference in the cell receptors recognized by the envelope. Mature particles are found to bind to C-type lectin receptors for entry. In contrast, partially mature particles have been shown to recognize lipid receptors such as TIM (T-Cell immunoglobulin mucin) and TAM (receptor tyrosine kinases, TYRO 3, AXL, and MER) (63–65). Once bound to receptors, viral particles enter the cell through clathrin-mediated endocytosis (31, 39, 64, 66–68). Once inside the cell, a vesicle transports the viral particles to be delivered to endosomes. Through low pH changes within the endosome, a change in the envelope occurs, allowing for fusion with the endosome membrane and the subsequent release of viral RNA into the cytoplasm (31, 64, 67–69). Genomic RNA is then translated into the structural and non-structural proteins mentioned previously in Section **1.1**; these viral proteins facilitate further replication, immune evasion, and viral packaging, either directly or indirectly (5, 6, 38, 39, 70). Further replication of the viral genome occurs inside virus-induced compartments, also referred to as replication organelles, along the membrane of the endoplasmic reticulum (ER), where negative-sense strands are used as a template (6, 31, 38, 64, 70, 71). Once viral genomes accumulate, viral assembly occurs between the prM and E proteins, forming a heterodimer on the ER membrane and

allowing budding into the ER lumen and interaction with the C proteins. These proteins are then released in vesicles (31, 38, 70, 71). These vesicles subsequently enter the Golgi apparatus, where the immature viral particle is processed through furin cleavage (prM to M), producing mature virions that can then be released through exocytosis (31, 72–74).

Infection with ZIKV can manifest in a variety of symptoms. While many individuals may be asymptomatic, approximately 25% display typical flu-like symptoms, such as fever, rash, headache, and vomiting, and there is a potential for the development of severe cases (39, 40, 52). In these severe cases, ZIKV can cause serious neurological conditions such as Guillain-Barré syndrome, an autoimmune disease that damages the nervous system, causing muscle weakness, paralysis, and potentially death (39, 40, 52, 75–77). The ability for ZIKV to be passed vertically during infection to developing fetuses has also been observed, predominantly during the epidemic in Brazil, causing the development of gestational microcephaly, which leads to cranial abnormalities that are typically fatal (39, 40, 49, 52, 78). Further studies have been done on the effect ZIKV has within developing neuronal cells, it has been determined that ZIKV directly infects human progenitor cells, inducing cell death and halting cell cycle progression. It has also been found to infect cortical cell layers, disrupting the migration and maturation of neuronal cells (44, 79–82). With the rapid spread and potential development of these severe neurological syndromes, research has focused on the development of potential antiviral or therapeutic agents (3, 83). Various vaccines have begun clinical trials; however, there is currently no approved vaccine or treatment for ZIKV infection, as many animal models do not accurately recapitulate human responses (84–87).

1.3- Untranslated Terminal Regions

While structural and non-structural proteins play key roles within the viral life cycle, the untranslated terminal regions (TR) have crucial roles within regulation, virulence, host-specificity, and immune evasion (88, 89). These untranslated terminal regions consist of approximately 100 nts at the 5' TR and from 400 - 800nts at the 3' TR, depending on the flavivirus. These highly structured TRs exhibit common secondary structures among different family members, with variations in the number or position of these secondary structures, specifically in the 3' TR (90, 91). The 5' TR contains a stem loop A (SLA), a smaller stem loop B (SLB), as well as a capsid coding region hairpin (cHP), which is critical in translation and proper initiation (91, 92). Efficient replication is promoted by SLA, which is recognized by NS5 during transcription, with deletions of SLA abolishing replication due to failure of NS5's recognition and binding (93). Transcription is also influenced by SLB, which contains complementary regions to the 3' TR, such as the upstream AUG region (UAR) and downstream AUG region (DAR) (94–97). During transcription initiation, SLB undergoes structural remodelling, influencing the translocation of NS5 to the 3' TR initiation site for transcription (94, 95). Secondary structure present within the 3' TR differs more in the amount present, with a highly variable region directly after the stop codon, a moderately conserved region, and a highly conserved region (91). Typically, the 3' TR contains an array of simple and branched stem loops within the highly variable region, 1-2 dumbbells within the moderate, and a short hairpin and 3' Stem loop (3' SL) within the highly conserved region (91, 98–100). The 3'SL is highly conserved among all flaviviruses, with both deletions and mutations in the 3'SL being detrimental to viral replication. Disruption of the 3' SL impairs the ability of NS5 to translocate to the 3'TR, preventing the initiation of transcription (98, 101).

The cyclization sequence, an 11-nucleotide region found within both TRs, is a primary promoter of the cyclization interaction (89, 102, 103). This interaction entails the formation of a panhandle structure between the terminal regions that is stabilized through complementary base pairing (104, 105). This formation enables the virus to tightly control its transcription initiation, as both translation and transcription processes cannot occur simultaneously due to their opposing directions on the same genome (106–108). This cyclization thus regulates the on state of transcription. Once in the cyclized form, NS5 can translocate from the 5' TR to the 3' TR to begin transcription (108). Previous studies on flaviviruses, such as Dengue and Kunjin virus, have shown that mutations within the cyclization sequence abolish replication, while compensatory mutations can facilitate replication, albeit at reduced rates (102, 109). This decreased efficiency could be attributed to the disruption of secondary or tertiary structures by the change in nucleotide order. Given the Zika virus's growing public health threat and the limited understanding of its cyclization specificity, the determination if these interactions depend on strict sequence conservation is of interest. Since the cyclization sequence contributes to a critical regulatory step in the viral life cycle, identifying a key region to inhibit would be beneficial for future therapeutic strategies.

1.3.1- Host proteins and their interactions with Zika Virus terminal regions

During Zika infection, viral proteins facilitate many of the functions required for viral replication through interactions with a variety of host proteins, with many of these interactions also serving to evade immune responses (110, 111). While these interactions contribute a large portion of the replication life cycle, direct and indirect interactions between host proteins and ZIKV TRs are also crucial factors during replication (112). Various host proteins have been identified to interact with these terminal regions, performing functions such as unwinding structural regions to facilitate transcription or acting as chaperones to aid in the formation of

replication complexes (113–115). Interactions between the TRs and host proteins have been shown also to facilitate viral evasion for Zika as well as other flaviviruses. Various anti-viral and immune response proteins have demonstrated a propensity for interactions with the TRs to signal degradation or inhibit viral replication (116, 117). Flaviviruses have evolved a mechanism to counteract these host immune responses by producing subgenomic flaviviral RNA (sfRNA), which functions as an immune evasion system (118). During infection, sfRNA accumulates within the cells due to the stalling of host exoribonucleases, specifically XRN-1, on stable secondary and tertiary structures within the 3' TR (119–121). This sfRNA accumulates, dysregulating cellular messenger RNA (mRNA) processing, interfering with RNA interference pathways by antagonizing small interfering RNA (siRNA) as well as microRNA (miRNA), and sequestering host immune proteins (121–123), collectively acting to evade host immune responses, enabling the viral genome replication to go unhindered. While the sfRNA-mediated mechanisms have been well studied, the specific host protein interactions with ZIKV TRs remain poorly characterized. Identifying these protein-RNA interactions is crucial to developing a deeper understanding of the ZIKV viral life cycle and the role of host proteins in facilitating its replication, which could lead to the identification of therapeutic targets through further investigation.

1.4- Thesis Objectives

With no approved treatments for Zika virus infection, research to determine an effective therapy is crucial as the threat of further spread increases. Current research has extensively characterized the structures present within the terminal regions, but understanding the interactions these terminal regions have with each other, as well as host proteins, is lacking. The main overall objective is to further explore the TRs of Zika, as this could lead to a better understanding of the interactions that occur during its viral life cycle and the specificity of these interactions.

The first sub-objective was to biophysically characterize the specificity of the cyclization interaction within ZIKV through *in vitro* assays. Chapter 2 details the use of biophysical methods, such as microscale thermophoresis (MST) and size exclusion multi-angle light scattering (SEC-MALS), in elucidating the effects of mutations within the cyclization sequence. These methods were subsequently used to verify the ability of a compensatory sequence to rescue the cyclization interaction. This mutation was then applied to cellular studies within mammalian liver cells to investigate its effects on replication under cellular conditions.

The second sub-objective was to investigate the potential interaction between the host translational regulator protein FXR1 and ZIKV 5' and 3' TRs. Through immunoprecipitation pulldown assays, the host protein FXR1 was identified as a potential interactor with the TRs of ZIKV. Chapter 3 describes the process of recombinantly expressing and purifying FXR1, followed by the use of biophysical methods, including analytical ultracentrifugation and SEC-MALS, to determine its purity and hydrodynamic properties. Following purification, through the use of biophysical methods, including MST and electrophoretic mobility shift assays, the interaction with ZIKV TRs was characterized, aiming to provide further understanding of this protein's role in the viral life cycle and its potential as a therapeutic target.

1.5- References

1. Y. J. S. Huang, S. Higgs, K. M. E. Horne, D. L. Vanlandingham, Flavivirus-Mosquito Interactions. *Viruses* **6**, 4703 (2014).
2. S. C. Weaver, C. Charlier, N. Vasilakis, M. Lecuit, Zika, Chikungunya, and Other Emerging Vector-Borne Viral Diseases. *Annu Rev Med* **69**, 395–408 (2018).
3. J. V. J. Silva, *et al.*, Current status, challenges and perspectives in the development of vaccines against yellow fever, dengue, Zika and chikungunya viruses. *Acta Trop* **182**, 257–263 (2018).
4. W. C. Ng, R. Soto-Acosta, S. S. Bradrick, M. A. Garcia-Blanco, E. E. Ooi, The 5′ and 3′ Untranslated Regions of the Flaviviral Genome. *Viruses* **9**, 137 (2017).
5. T. J. Chambers, C. S. Hahn, R. Galler, C. M. Rice, Flavivirus genome organization, expression, and replication. *Annu Rev Microbiol* **44**, 649–688 (1990).
6. M. A. Garcia-Blanco, S. G. Vasudevan, S. S. Bradrick, C. Nicchitta, Flavivirus RNA transactions from viral entry to genome replication. *Antiviral Res* **134**, 244–249 (2016).
7. X. Zhang, *et al.*, Structures and Functions of the Envelope Glycoprotein in Flavivirus Infections. *Viruses* **9**, 338 (2017).
8. T. R. Barnard, Q. H. Abram, Q. F. Lin, A. B. Wang, S. M. Sagan, Molecular Determinants of Flavivirus Virion Assembly. *Trends Biochem Sci* **46**, 378–390 (2021).
9. S. Sun, V. B. Rao, M. G. Rossmann, Genome packaging in viruses. *Curr Opin Struct Biol* **20**, 114–120 (2010).
10. L. Ye, *et al.*, RNA Structures and Their Role in Selective Genome Packaging. *Viruses* **13**, 1788 (2021).
11. J. D. Perlmutter, M. F. Hagan, Mechanisms of Virus Assembly. *Annu Rev Phys Chem* **66**, 217 (2014).
12. D. Bhella, Virus Proteins and Nucleoproteins: An Overview. *Subcell Biochem* **88**, 1–18 (2018).
13. D. A. Muller, P. R. Young, The flavivirus NS1 protein: Molecular and structural biology, immunology, role in pathogenesis and application as a diagnostic biomarker. *Antiviral Res* **98**, 192–208 (2013).
14. Q. Zeng, J. Liu, C. Hao, B. Zhang, H. Zhang, Making sense of flavivirus non-strctural protein 1 in innate immune evasion and inducing tissue-specific damage. *Virus Res* **336**, 199222 (2023).
15. J. Estévez-Herrera, *et al.*, Zika Virus Pathogenesis: A Battle for Immune Evasion. *Vaccines 2021, Vol. 9, Page 294* **9**, 294 (2021).
16. A. Latanova, E. Starodubova, V. Karpov, Flaviviridae Nonstructural Proteins: The Role in Molecular Mechanisms of Triggering Inflammation. *Viruses* **14**, 1808 (2022).

17. J. M. Mackenzie, M. K. Jones, P. R. Young, Immunolocalization of the Dengue Virus Nonstructural Glycoprotein NS1 Suggests a Role in Viral RNA Replication. *Virology* **220**, 232–240 (1996).

18. X. Zhang, *et al.*, Zika virus NS2A-mediated virion assembly. *mBio* **10** (2019).

19. X. Xie, *et al.*, Dengue NS2A Protein Orchestrates Virus Assembly. *Cell Host Microbe* **26**, 606-622.e8 (2019).

20. Z. Zhang, *et al.*, crystal structure of unlinked NS2B-NS3 protease from Zika virus. *Science (1979)* **354**, 1597–1600 (2016).

21. K. E. Du Pont, M. McCullagh, B. J. Geiss, Conserved motifs in the flavivirus NS3 RNA helicase enzyme. *Wiley Interdiscip Rev RNA* **13** (2022).

22. S. Xu, *et al.*, Zika virus NS3 is a canonical RNA helicase stimulated by NS5 RNA polymerase. *Nucleic Acids Res* **47**, 8693–8707 (2019).

23. D. Luo, *et al.*, Insights into RNA unwinding and ATP hydrolysis by the flavivirus NS3 protein. *EMBO Journal* **27**, 3209–3219 (2008).

24. Y. Wu, *et al.*, Zika virus evades interferon-mediated antiviral response through the co-operation of multiple nonstructural proteins in vitro. *Cell Discov* **3**, 1–14 (2017).

25. M. Verhaegen, K. Vermeire, The endoplasmic reticulum (ER): a crucial cellular hub in flavivirus infection and potential target site for antiviral interventions. *npj Viruses 2024 2:1* **2**, 1–17 (2024).

26. E. Morita, Y. Suzuki, Membrane-Associated Flavivirus Replication Complex—Its Organization and Regulation. *Viruses 2021, Vol. 13, Page 1060* **13**, 1060 (2021).

27. R. Boytz, K. Keita, J. B. Pawlak, M. Laurent-Rolle, Flaviviruses manipulate mitochondrial processes to evade the innate immune response. *npj Viruses 2024 2:1* **2**, 1–9 (2024).

28. J. L. Muñoz-Jordán, G. G. Sánchez-Burgos, M. Laurent-Rolle, A. García-Sastre, Inhibition of interferon signaling by dengue virus. *Proc Natl Acad Sci U S A* **100**, 14333–14338 (2003).

29. J. Morrison, S. Aguirre, A. Fernandez-Sesma, Innate immunity evasion by dengue virus. *Viruses* **4**, 397–413 (2012).

30. N. A. Dalrymple, V. Cimica, E. R. Mackow, Dengue virus NS proteins inhibit RIG-I/MAVS signaling by blocking TBK1/IRF3 phosphorylation: Dengue virus serotype 1 NS4A is a unique interferon-regulating virulence determinant. *mBio* **6**, 1–12 (2015).

31. K. Van Den Elsen, J. P. Quek, D. Luo, Molecular insights into the flavivirus replication complex. *Viruses* **13** (2021).

32. P. Klaitong, D. R. Smith, Roles of Non-Structural Protein 4A in Flavivirus Infection. *Viruses* **13**, 2077 (2021).

33. Q. Li, C. Kang, Dengue virus NS4B protein as a target for developing antivirals. *Front Cell Infect Microbiol* **12** (2022).

34. J. Z. H. Goh, L. De Hayr, A. A. Khromykh, A. Slonchak, The Flavivirus Non-Structural Protein 5 (NS5): Structure, Functions, and Targeting for Development of Vaccines and Therapeutics. *Vaccines 2024, Vol. 12, Page 865* **12**, 865 (2024).

35. T. Fajardo, *et al.*, The flavivirus polymerase NS5 regulates translation of viral genomic RNA. *Nucleic Acids Res* **48**, 5081–5093 (2020).

36. W. Ren, *et al.*, Zika virus NS5 protein inhibits type I interferon signaling via CRL3 E3 ubiquitin ligase-mediated degradation of STAT2. *Proc Natl Acad Sci U S A* **121** (2024).

37. A. Grant, *et al.*, Zika Virus Targets Human STAT2 to Inhibit Type i Interferon Signaling. *Cell Host Microbe* **19**, 882–890 (2016).

38. S. I. Yun, Y. M. Lee, Zika virus: An emerging flavivirus. *Journal of Microbiology* **55**, 204–219 (2017).

39. B. H. Song, S. I. Yun, M. Woolley, Y. M. Lee, Zika virus: History, epidemiology, transmission, and clinical presentation. *J Neuroimmunol* **308**, 50–64 (2017).

40. D. Musso, D. J. Gubler, Zika Virus. *Clin Microbiol Rev* **29**, 487–524 (2016).

41. R. S. Lanciotti, A. J. Lambert, M. Holodniy, S. Saavedra, L. del Carmen Castillo Signor, Phylogeny of Zika Virus in Western Hemisphere, 2015. *Emerg Infect Dis* **22**, 933–935 (2016).

42. S. J. Hung, S. W. Huang, Contributions of Genetic Evolution to Zika Virus Emergence. *Front Microbiol* **12** (2021).

43. P. Österlund, *et al.*, Asian and African lineage Zika viruses show differential replication and innate immune responses in human dendritic cells and macrophages. *Scientific Reports 2019 9:1* **9**, 1–15 (2019).

44. Q. Shao, *et al.*, The African Zika virus MR-766 is more virulent and causes more severe brain damage than current Asian lineage and dengue virus. *Development* **144**, 4114 (2017).

45. B. T. D. Nunes, *et al.*, Zika structural genes determine the virulence of African and Asian lineages. *Emerg Microbes Infect* **9**, 1023 (2020).

46. M. R. Duffy, *et al.*, Zika Virus Outbreak on Yap Island, Federated States of Micronesia. *New England Journal of Medicine* **360**, 2536–2543 (2009).

47. F. R. Cugola, *et al.*, The Brazilian Zika virus strain causes birth defects in experimental models. *Nature* **534**, 267 (2016).

48. A. Gulland, Zika virus is a global public health emergency, declares WHO. *BMJ* **352**, i657 (2016).

49. R. Lowe, *et al.*, The zika virus epidemic in brazil: From discovery to future implications. *Int J Environ Res Public Health* **15** (2018).

50. D. Musso, E. J. Nilles, V. M. Cao-Lormeau, Rapid spread of emerging Zika virus in the Pacific area. *Clinical Microbiology and Infection* **20**, O595–O596 (2014).

51. D. Musso, *et al.*, Potential for Zika virus transmission through blood transfusion demonstrated during an outbreak in French Polynesia, November 2013 to February 2014. *Eurosurveillance* **19**, 20761 (2014).

52. V. Sharma, *et al.*, Zika virus: An emerging challenge to public health worldwide. *Can J Microbiol* **66**, 87–98 (2020).

53. R. S. Lanciotti, *et al.*, Genetic and serologic properties of Zika virus associated with an epidemic, Yap State, Micronesia, 2007. *Emerg Infect Dis* **14**, 1232–1239 (2008).

54. N. R. Faria, *et al.*, Zika virus in the Americas: Early epidemiological and genetic findings. *Science (1979)* **352**, 345–349 (2016).

55. C. Fellner, Zika in America: The Year in Review. *Pharmacy and Therapeutics* **41**, 778 (2016).

56. Countries & Territories at Risk for Zika | Zika Virus | CDC. Available at: https://www.cdc.gov/zika/geo/index.html [Accessed 27 May 2025].

57. A. Wang, S. Thurmond, L. Islas, K. Hui, R. Hai, Zika virus genome biology and molecular pathogenesis. *Emerg Microbes Infect* **6** (2017).

58. D. Sirohi, *et al.*, The 3.8 Å resolution cryo-EM structure of Zika virus. *Science* **352**, 467–470 (2016).

59. M. Sevvana, *et al.*, Refinement and Analysis of the Mature Zika Virus Cryo-EM Structure at 3.1 Å Resolution. *Structure* **26**, 1169-1177.e3 (2018).

60. A. Du Toit, Zika virus structure, epidemiology and evolution. *Nat Rev Microbiol* **14**, 267–267 (2016).

61. H. M. Lazear, *et al.*, A mouse model of Zika virus pathogenesis. *Cell Host Microbe* **19**, 720–730 (2016).

62. J. Govero, *et al.*, Zika virus infection damages the testes in mice. *Nature 2016 540:7633* **540**, 438–442 (2016).

63. Z. Y. Wang, *et al.*, Axl is not an indispensable factor for zika virus infection in mice. *Journal of General Virology* **98**, 2061–2068 (2017).

64. A. Agrelli, R. R. de Moura, S. Crovella, L. A. C. Brandão, ZIKA virus entry mechanisms in human cells. *Infection, Genetics and Evolution* **69**, 22–29 (2019).

65. A. Roy, Q. Liu, Y. Yang, A. K. Debnath, L. Du, Envelope Protein-Targeting Zika Virus Entry Inhibitors. *Int J Mol Sci* **25** (2024).

66. S. A. Mousavi, L. Malerød, T. Berg, R. Kjeken, Clathrin-dependent endocytosis. *Biochemical Journal* **377**, 1–16 (2004).

67. J. Mercer, M. Schelhaas, A. Helenius, Virus entry by endocytosis. *Annu Rev Biochem* **79**, 803–833 (2010).

68. J. L. Goldstein, R. G. W. Anderson, M. S. Brown, Coated pits,coated vesicles,and receptor-mediated endocytosis. *Nature* **279**, 679–685 (1979).

69. A. Helenius, I. Mellman, D. Wall, A. Hubbard, Endosomes. *Trends Biochem Sci* **8**, 245–250 (1983).

70. G. Sager, S. Gabaglio, E. Sztul, G. A. Belov, Role of Host Cell Secretory Machinery in Zika Virus Life Cycle. *Viruses 2018, Vol. 10, Page 559* **10**, 559 (2018).

71. S. Apte-Sengupta, D. Sirohi, R. J. Kuhn, Coupling of replication and assembly in flaviviruses. *Curr Opin Virol* **9**, 134–142 (2014).

72. K. Stadler, S. L. Allison, J. Schalich, F. X. Heinz, Proteolytic activation of tick-borne encephalitis virus by furin. *J Virol* **71**, 8475–8481 (1997).

73. F. X. Heinz, *et al.*, Structural changes and functional control of the tick-borne encephalitis virus glycoprotein E by the heterodimeric association with protein prM. *Virology* **198**, 109–17 (1994).

74. F. Guirakhoo, F. X. Heinz, C. W. Mandl, H. Holzmann, C. Kunz, Fusion activity of flaviviruses: Comparison of mature and immature (prM-containing) tick-borne encephalitis virions. *Journal of General Virology* **72**, 1323–1329 (1991).

75. P. Brasil, *et al.*, Guillain-Barré syndrome associated with Zika virus infection. *The Lancet* **387**, 1482 (2016).

76. F. Krauer, *et al.*, Zika Virus Infection as a Cause of Congenital Brain Abnormalities and Guillain–Barré Syndrome: Systematic Review. *PLoS Med* **14** (2017).

77. V. M. Cao-Lormeau, *et al.*, Guillain-Barré Syndrome outbreak associated with Zika virus infection in French Polynesia: A case-control study. *The Lancet* **387**, 1531–1539 (2016).

78. S. A. Rasmussen, D. J. Jamieson, M. A. Honein, L. R. Petersen, Zika Virus and Birth Defects — Reviewing the Evidence for Causality. *New England Journal of Medicine* **374**, 1981–1987 (2016).

79. N. Zhang, *et al.*, Zika Virus Disrupts Neural Progenitor Development and Leads to Microcephaly in Mice. *Cell Stem Cell* **19**, 120–126 (2016).

80. H. Tang, *et al.*, Zika Virus Infects Human Cortical Neural Progenitors and Attenuates Their Growth. *Cell Stem Cell* **18**, 587–590 (2016).

81. I. Gladwyn-Ng, *et al.*, Stress-induced unfolded protein response contributes to Zika virus-associated microcephaly. *Nat Neurosci* **21**, 63–73 (2018).

82. D. Xu, C. Li, C. F. Qin, Z. Xu, Update on the Animal Models and Underlying Mechanisms for ZIKV-Induced Microcephaly. *Annu Rev Virol* **6**, 459–479 (2019).

83. N. Camacho-Concha, *et al.*, Insights into Zika Virus Pathogenesis and Potential Therapeutic Strategies. *Biomedicines* **11** (2023).

84. M. A. McArthur, Zika Virus: Recent Advances towards the Development of Vaccines and Therapeutics. *Viruses* **9** (2017).

85. C. Shan, *et al.*, A live-attenuated Zika virus vaccine candidate induces sterilizing immunity in mouse models. **23** (2017).

86. M. V. Mancini, *et al.*, Evaluation of an Engineered Zika Virus-Like Particle Vaccine Candidate in a Mosquito-Mouse Transmission Model. *mSphere* **8** (2023).

87. B. H. Song, *et al.*, Comparison of Three Chimeric Zika Vaccine Prototypes Developed on the Genetic Background of the Clinically Proven Live-Attenuated Japanese Encephalitis Vaccine SA14-14-2. *Int J Mol Sci* **26** (2024).

88. P. Li, *et al.*, Integrative Analysis of Zika Virus Genome RNA Structure Reveals Critical Determinants of Viral Infectivity. *Cell Host Microbe* **24**, 875-886.e5 (2018).

89. X.-D. Li, C.-L. Deng, Z.-M. Yuan, H.-Q. Ye, B. Zhang, Different Degrees of 5'-to-3' DAR Interactions Modulate Zika Virus Genome Cyclization and Host-Specific Replication. *J Virol* **94** (2020).

90. M. A. Brinton, J. H. Dispoto, Sequence and secondary structure analysis of the 5′-terminal region of flavivirus genome RNA. *Virology* **162**, 290–299 (1988).

91. C. Mazeaud, W. Freppel, L. Chatel-Chaix, The Multiples Fates of the Flavivirus RNA Genome During Pathogenesis. *Front Genet* [Preprint] (2018).

92. M. A. Brinton, J. H. Dispoto, Sequence and secondary structure analysis of the 5′-terminal region of flavivirus genome RNA. *Virology* **162**, 290–299 (1988).

93. K. H. Choi, The Role of the Stem-Loop A RNA Promoter in Flavivirus Replication. *Viruses* **13**, 1107 (2021).

94. S. Sharma, G. Varani, NMR structure of Dengue West Nile Viruses stem-loop B: a key cis-acting element for Flavivirus Replication. *Biochem Biophys Res Commun* **531**, 522 (2020).

95. Z. Y. Liu, *et al.*, Viral RNA switch mediates the dynamic control of flavivirus replicase recruitment by genome cyclization. *Elife* **5** (2016).

96. P. Friebe, E. Harris, Interplay of RNA Elements in the Dengue Virus 5′ and 3′ Ends Required for Viral RNA Replication. *J Virol* **84**, 6103 (2010).

97. Y. Song, J. A. Mugavero, C. B. Stauft, E. Wimmer, Dengue and Zika Virus 5' Untranslated Regions Harbor Internal Ribosomal Entry Site Functions. *mBio* **10** (2019).

98. G. P. Göertz, S. R. Abbo, J. J. Fros, G. P. Pijlman, Functional RNA during Zika virus infection. *Virus Res* [Preprint] (2018).

99. B. Cerikan, *et al.*, A Non-Replicative Role of the 3′ Terminal Sequence of the Dengue Virus Genome in Membranous Replication Organelle Formation. *Cell Rep* **32**, 107859 (2020).

100. M. T. Wolfinger, R. Ochsenreiter, I. L. Hofacker, Functional RNA Structures in the 3'UTR of Mosquito-Borne Flaviviruses. (2021).

101. L. G. Gebhard, C. V. Filomatori, A. V. Gamarnik, Functional RNA Elements in the Dengue Virus Genome. *Viruses 2011, Vol. 3, Pages 1739-1756* **3**, 1739–1756 (2011).

102. A. A. Khromykh, H. Meka, K. J. Guyatt, E. G. Westaway, Essential Role of Cyclization Sequences in Flavivirus RNA Replication. *J Virol* **75**, 6719 (2001).

103. C. S. Hahn, *et al.*, Conserved elements in the 3' untranslated region of flavivirus RNAs and potential cyclization sequences. *J Mol Biol* **198**, 33–41 (1987).

104. D. E. Alvarez, M. F. Lodeiro, S. J. Ludueña, L. I. Pietrasanta, A. V. Gamarnik, Long-Range RNA-RNA Interactions Circularize the Dengue Virus Genome. *J Virol* **79**, 6631 (2005).

105. R. G. Huber, *et al.*, Structure mapping of dengue and Zika viruses reveals functional long-range interactions. *Nature Communications 2019 10:1* **10**, 1–13 (2019).

106. D. E. Alvarez, A. L. De Lella Ezcurra, S. Fucito, A. V. Gamarnik, Role of RNA structures present at the 3′UTR of dengue virus on translation, RNA synthesis, and viral replication. *Virology* **339**, 200–212 (2005).

107. T. J. Sanford, H. V. Mears, T. Fajardo, N. Locker, T. R. Sweeney, Circularization of flavivirus genomic RNA inhibits de novo translation initiation. *Nucleic Acids Res* **47**, 9789–9802 (2019).

108. A. V. Gamarnik, R. Andino, Switch from translation to RNA replication in a positive-stranded RNA virus. *Genes Dev* **12**, 2293 (1998).

109. W.-W. Chiu, R. M. Kinney, T. W. Dreher, Control of Translation by the 5′- and 3′-Terminal Regions of the Dengue Virus Genome. *J Virol* **79**, 8303 (2005).

110. A. T. Fishburn, O. H. Pham, M. W. Kenaston, N. S. Beesabathuni, P. S. Shah, Let's Get Physical: Flavivirus-Host Protein–Protein Interactions in Replication and Pathogenesis. *Front Microbiol* **13**, 847588 (2022).

111. V. A. Golubeva, *et al.*, Network of Interactions between ZIKA Virus Non-Structural Proteins and Human Host Proteins. *Cells* **9**, 153 (2020).

112. P. S. Shah, *et al.*, Comparative Flavivirus-Host Protein Interaction Mapping Reveals Mechanisms of Dengue and Zika Virus Pathogenesis. *Cell* **175**, 1931-1945.e18 (2018).

113. C. Nelson, *et al.*, Human DDX3X Unwinds Japanese Encephalitis and Zika Viral 5 Terminal Regions Human DDX3X Unwinds Japanese. *Terminal Regions. Int. J. Mol. Sci* **2021**, 413 (2021).

114. D. L. Gemmill, *et al.*, The 3′ terminal region of Zika virus RNA contains a conserved G-quadruplex and is unfolded by human DDX17. *Biochemistry and Cell Biology* **102**, 96–105 (2024).

115. S. Taguwa, *et al.*, Zika Virus Dependence on Host Hsp70 Provides a Protective Strategy against Infection and Disease. *Cell Rep* **26**, 906 (2019).

116. H.-P. Chiu, *et al.*, Inhibition of Japanese encephalitis virus infection by the host zinc-finger antiviral protein. (2018). https://doi.org/10.1371/journal.ppat.1007166.

117. S. Chattopadhyay, *et al.*, Zinc Finger CCCH-Type Antiviral Protein 1 Restricts the Viral Replication by Positively Regulating Type I Interferon Response. (2020). https://doi.org/10.3389/fmicb.2020.01912.

118. R. Delli Ponti, A. Vandelli, G. G. Tartaglia, Subgenomic flaviviral RNAs and human proteins: in silico exploration of anti-host defense mechanisms. *Comput Struct Biotechnol J* **23**, 3527–3536 (2024).

119. A. Slonchak, *et al.*, Structural analysis of 3'UTRs in insect flaviviruses reveals novel determinants of sfRNA biogenesis and provides new insights into flavivirus evolution. *Nat Commun* **13** (2022).

120. H. M. Pallarés, *et al.*, Zika Virus Subgenomic Flavivirus RNA Generation Requires Cooperativity between Duplicated RNA Structures That Are Essential for Productive Infection in Human Cells. *J Virol* **94** (2020).

121. A. Slonchak, A. A. Khromykh, Subgenomic flaviviral RNAs: What do we know after the first decade of research. *Antiviral Res* **159**, 13–25 (2018).

122. X. Chen, *et al.*, The subgenomic flaviviral RNA suppresses RNA interference through competing with siRNAs for binding RISC components. *J Virol* **98** (2024).

123. D. Michalski, *et al.*, Zika virus noncoding sfRNAs sequester multiple host-derived RNA-binding proteins and modulate mRNA decay and splicing during infection. *Journal of Biological Chemistry* **294**, 16282–16296 (2019).

Chapter 2: Circle of "Life": Zika Virus genomic cyclization is controlled by sequence specificity

2.1- Foreword

This chapter consists of a manuscript that has been submitted to the *Journal of Virology*. Work was performed in collaboration with Danielle Gemmill, Dr. Higor Pereira, Dr. Michael Wolfinger, and Dr. Trushar Patel. I conducted all wet laboratory experiments and cellular studies, as well as designing a variety of constructs and replicon mutations. Danielle Gemmill assisted in the construction design of 5' and 3' terminal regions and initial interaction studies. Dr. Pereira assisted in cellular studies, while Dr. Wolfinger performed the *in-silico* analysis of the terminal regions. I wrote the manuscript with input and editing assistance from Dr. Pereira, Dr. Wolfinger, and Dr. Patel.

2.2- Abstract

The Zika Virus (ZIKV), a neuroinvasive flavivirus transmitted by mosquitoes, continues to pose a global threat to healthcare systems, as 89 countries are currently at risk of transmission, with an expanding area of infection due to global warming. The positive-sense single-stranded RNA genome must effectively regulate its transcription and translation, with both processes occurring on the same molecule. Through a unique cyclization mechanism mediated by a conserved 11-nucleotide complementary sequence present in the 5′-3′ untranslated terminal regions of the genome, the virus can regulate the initiation of these processes. Using biophysical methods such as microscale thermophoresis, size exclusion multi-angle light scattering, and cell culturing replicon assays, we demonstrate that this cyclization interaction is specific to the conserved 11-nucleotide sequence. By mutating the cyclization sequence alongside compensatory mutations, we have shown that complementary base pairing alone is inadequate for efficient cyclization; secondary or tertiary structures influenced by the specific 11-nucleotide sequence are essential for effective cyclization and replication. This finding could pave the way for the development of therapeutics targeting this conserved sequence within the viral genome, as blocking it can lead to disruption of crucial transcription initiation. This also allows for application to other members of the Flavivirus family due to the conserved nature of the sequence.

2.3- Introduction

Flaviviruses, such as Zika virus (ZIKV), are significant pathogens of concern, infecting many individuals and imposing substantial social and economic burdens in recent years (1–4). Zika virus is a neuroinvasive arbovirus primarily transmitted through *Aedes aegypti* and *Aedes albopictus* mosquitoes, which belong to the *Flaviviridae* family, alongside notable members like Dengue, Japanese encephalitis, and West Nile virus (5–7). As of 2024, there are 89 countries susceptible to ZIKV infection. Recent outbreaks, including one in 2015 in Brazil that infected 1.5 million people and a more recent one in 2024 in India, have placed a burden on healthcare systems (3, 4, 8, 9). With no vaccine or antiviral treatment available, ZIKV remains an ongoing concern for these healthcare systems (10–14). Infection with ZIKV can present varying symptoms, ranging from asymptomatic cases to severe neurological syndromes, such as Guillain-Barré syndrome, which causes damage to nerve cells, leading to muscle weakness or paralysis (15, 16). Another serious neurological syndrome of great concern is gestational microcephaly, which may occur if a woman with a developing fetus is infected by ZIKV; this syndrome results in permanent cranial abnormalities in developing fetuses in *utero* (17–19). Given the potential for these profound syndromes to arise from infection, medical research has focused on developing potential therapeutics in hopes of limiting these potential afflictions.

ZIKV is similar to other flaviviruses, being an enveloped virus that contains a single-stranded positive-sense RNA genome of approximately 11,000 nucleotides (nts) in length. ZIKV's genome features two untranslated terminal regions (TR) at the 5′ and 3′ ends, measuring 107 nts and 428 nts, respectively, which flank the open reading frame that encodes a single polyprotein (20–22). Although these terminal regions cannot encode viral proteins, these non-coding RNAs can fold into secondary structures that influence virulence and the ability to produce subgenomic

flaviviral RNA, which is critical for immune evasion and suppression (21, 23–26). Secondary structures within the TRs are highly conserved across Zika isolates and other flaviviruses, indicating considerable selective pressure to maintain these features, and they have been shown to be crucial factors in the replication and transmission of the virus (21, 27). The processes of translation and transcription are tightly regulated through cyclization, which occurs via long-range intra-genomic RNA-RNA interactions between the TRs. The interaction among these terminal regions forms a stabilized panhandle structure; a visual representation of this formation can be seen in **Figure 2.1** (28–31). This interaction mediates the genome's transcription by the viral RNA-dependent RNA polymerase NS5, altering the secondary structure of the TRs during cyclization (32). Removing regions within the TRs or deleting specific secondary structures, primarily the 3′ SL, can be detrimental to replication in mammalian and mosquito vectors, respectively (33). This cyclization interaction is thought to be facilitated by a conserved cyclization sequence (CS) located just downstream of the 5′ TR and within the 3′ TR. Previous research has indicated that modifying the region downstream of the AUG start codon affects cyclization within mosquito vectors (34). While earlier studies have highlighted the significance of the cyclization sequence (28), little is known about the specificity of the cyclization sequence in ZIKV itself.

Through this study, we employ computational, biophysical, and cellular studies using a replicon system to investigate the cyclization interaction and the specificity of CS (35). We selected the Asian H/PF/2013 (HPF) and the African MR766 (MR766) strains to compare the specificity of CS across lineages, as these exhibit variance in virulence (36). First, employing computational methods, we determined the interaction energies of the TRs of various ZIKV strains through co-folding. From these strains, we mutated the CS of the 5′ TR and the 3′ TR to eliminate any base pairing. Using the mutated 5′ TR, we generated a compensatory sequence for the 3′ TR

to restore the base pairing of all 11 nucleotides with the mutated 5′ TR, aiming to establish if base pairing is sufficient for promoting the cyclization interaction. We then demonstrated through biophysical methods, such as multi-angle light scattering and microscale thermophoresis, that both strains interact with a 1:1 stoichiometry and exhibit nanomolar affinities. While mutations within the cyclization sequence abolished the interaction, a compensatory mutation did not restore it. We further substantiated our *in vitro* biophysical characterization by showing that the mutation within the cyclization sequence significantly reduces the replication of ZIKV using a replicon system in mammalian cells. These findings lead us to conclude that the cyclization interaction is facilitated by sequence specificity within the cyclization sequence across strains and kinetic favourability; and the use of cellular studies strengthens the *in vitro* findings, thus demonstrating this characterization is aptly applied. The specificity of this interaction could hopefully guide the future development of antivirals designed to target this cyclization sequence and disrupt the virus's ability to replicate. Through this study, we demonstrate that this cyclization interaction is promoted by sequence specificity using various biophysical methods as well as a cellular replicon system.

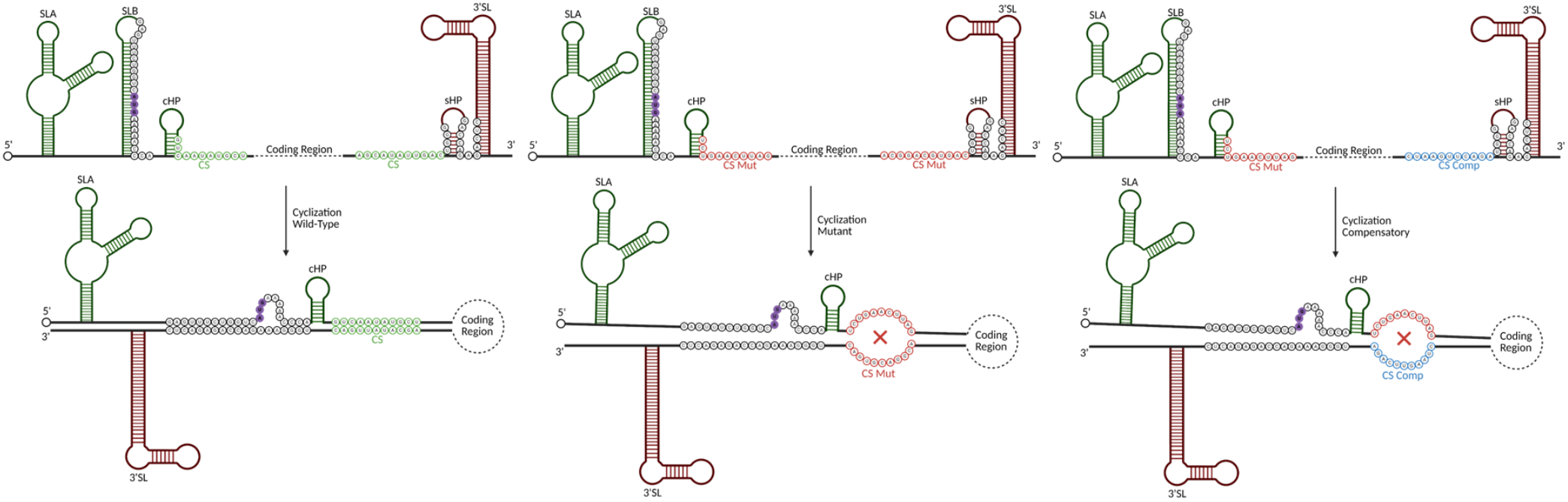

Figure 2.1: Visual representation of the cyclization interaction between TRs. With the wild-type cyclization sequence highlighted in green. The cyclization mutant sequence depicted in red lacks base pairing, thereby disrupting the interaction. While the compensatory sequence highlighted in blue has the proper complementarity for base pairing, the interaction is abolished due to sequence changes. The 5′ TR and 3′ TR are represented by the dark green and dark red secondary structures, respectively; the AUG start codon is highlighted in purple.

2.4- Methods

2.4.1- Computational Prediction of Cyclization Propensities

The interaction energies between the 5′ and 3′ TRs of the ZIKV MR766 and H/PF/2013 genomes were computed using RNAcofold from the ViennaRNA Package v2.7.0 (37).

2.4.2- Purification of ZIKV MR766 and HPF2013 Terminal Regions

Based on the high and low propensities for cyclization from computational determinations, constructs were designed using the ZIKV MR766 genome (genebank ID: NC_012532.1) and the H/PF/2013 genome (genebank ID: KJ776791.2), respectively, with the 5′ TRs and 3′ TRs being 210 nts and 221 nts, respectively. These TRs contained an extension to include the CS on the 5′TR, as well as a mutant CS and compensatory elements. The wild-type sequence of both TRs' cyclization sequences was mutated while maintaining A:U C:G content to abolish any base pairing. MR766 was mutated to UCUGAACUUAG and ACGGACGUGAG for the 5′ and 3′ TR, respectively, while HPF was mutated to GUCAAUAUGCU and AGCAUAUUGAC for the 5′ and 3′ TR, respectively. They were placed into pUC-GW-Kan constructs designed by Genewiz® (Azenta), with the addition of a T7 promoter at the beginning and an XbaI restriction cut site at the end of the transcript sequence; these complete sequences can be seen in the **supplemental Table 2.1**. These plasmids were then transformed into NEB5α *E. coli* cells, provided by New England Biolabs®. The expression plasmids were purified using a Thermo Scientific™ GeneJET Plasmid Maxiprep kit, followed by XbaI digestion for 4 hours at 37°C to linearize the plasmid. This linearized plasmid was then used for *in vitro* transcription (IVT), which was incubated at 37°C for 4 hours and treated with DNase for 1 hour at 37°C. After this incubation, RNA was purified using size-exclusion chromatography (SEC) on a Superdex 200 Increase GL 10/300

(S200) (Global Life Science Solutions USA LLC, Marlborough, MA, USA) in Bis-Tris RNA Buffer (10 mM Bis-Tris pH 5.5, 100 mM NaCl, 15 mM KCl, 5 mM MgCl2, 5% glycerol) via an ÄKTA pure FPLC (Global Life Science Solutions USA LLC, Marlborough, MA, USA) (35). The fractions determined to have RNA based on the chromatogram were run on a TAE 3% agarose gel for 30 minutes at 100V and stained with Sybersafe™ to ensure homogeneity. The pure fractions were collected, vitrified in liquid nitrogen, and stored at -80 °C until downstream experiments.

2.4.3- Size-Exclusion Chromatography Interaction Studies

To determine the initial interaction after obtaining purified RNA of ZIKV 5′ and 3′ TRs, a 1:1 interaction with a final concentration of 500 nM of each species was incubated for 1 hour at 25 °C. This interaction was then subjected to SEC again on a Superdex S200 (Cytiva), while recording the absorbance at 260 nm to visualize the shifting of elution peaks based on size. These interaction studies were subsequently performed with purified 5′ and 3′ mutant sequences, as well as 5′ mutant and 3′ compensatory sequences. The results observed through SEC were then also recapitulated through electrophoretic mobility shift assays observed in **Supplemental Figure 2.1**.

2.4.4- Size-Exclusion coupled to Multi-Angle Light Scattering

Size-exclusion coupled with multi-angle light scattering (SEC-MALS) was employed to determine the homogeneity and monodispersity of individual RNA samples, as well as the stoichiometry of the interaction. RNA samples were concentrated to 1.2 mg/mL for the individual interaction and 1.0 mg/mL for the complex interaction, respectively, and were centrifuged at 10,000 xg for 2 minutes to remove any potential aggregates. The interaction was also mixed at a 1:1 ratio. These samples were subsequently loaded into a Thermofisher Scientific Vanquish HPLC, connected to a KW403.5-4F Shodex column used for separation. Following size exclusion,

samples were passed through a Wyatt Dawn® (Wyatt Technology Corporation, Santa Barbara, CA, USA) MALS detector with 18 detector angles and a 658 nm laser. The refractive index was measured using an Optilab® refractometer (Wyatt Technology Corporation, Santa Barbara, CA, USA). The molecular weight of the RNA was determined using the Astra v8.0.0.25 software with the Debye model, excluding the second virial coefficient, A2 term, as the sample is dilute, as shown in Eq 1.

$$M_w = \frac{R(\theta)}{K*c} \quad (1)$$

Where K is the polymer constant Eq 2:

$$K = \frac{4\pi^2 n_0^2 (dn/dc)^2}{\lambda_0^4 N_A} \quad (2)$$

Where R(θ) is the Rayleigh Ratio of scattered light at an angle θ=0, c is the concentration of the solute in mg/mL determined from the refractive index, n is the refractive index of the solvent, λ0 is the wavelength of the laser, NA is Avogadro's number, and dn/dc is the change in refractive index due to the change in concentration. A value of 0.19 mL/g was used for this determination (38, 39).

2.4.5- Fluorescent Labelling of RNA

Fluorescent labelling was performed using reactive 5′ phosphate ends with an Alexa 488 fluorophore, as previously noted (40, 41). Briefly, RNAs were resuspended in 7.5 µL of Bis-Tris RNA buffer, concentrated to about 100 µM via ethanol precipitation. Following this, 20 µL of 0.1 M imidazole (pH 6), 1.25 mg of 1-ethyl-3-(3-dimethylamino) propyl carbodiimide hydrochloride, and 10 µL of Alexa 488 hydrazide were added to the resuspended RNA and incubated at room temperature for 4 hours. The RNA was then purified using SEC on an S200 column. Labeled

species were purified from unused fluorophore and degraded RNA, and pure, labeled RNA was stored at -80 °C until experimentation. The RNA labeling was tested with the Nanotemper Technologies Monolith®NT.115 (Nanotemper Technologies, Munich, Germany) using auto excitation power to ensure sufficient fluorescence was observed at the RNA concentrations employed for microscale thermophoresis assays.

2.4.6- Microscale Thermophoresis (MST)

A two-fold serial dilution of the various 3′TR RNA was conducted using 1x Bis-Tris RNA buffer, starting at 2.5 μM and continuing until the final concentration reached 0.076 nM. A constant volume of the various fluorescent 5′ TR RNA at a concentration of 100 nM was added to each serial dilution of the 3′ RNA. The reaction was subsequently incubated for one hour at 25 °C and then loaded into the Nanotemper Technologies Monolith® NT.115 instrument (Nanotemper Technologies, Munich, Germany) using standard capillaries for MST. Thermophoresis was performed at 80% excitation power with medium MST IR laser power. Fluorescent migration, used to determine $K_{d,}$ was measured from 1.5 to 2.5 seconds and normalized to the initial fluorescence. The assay was performed in triplicate (42, 43).

2.4.7- Cellular Replicon Assay

The replicon assays were conducted using ZIKV MR766 and H/PF/2013 replicon RLuc reporter systems provided by the Bartenschlager Lab (Heidelberg, Germany). To mutate the 5′ cyclization sequence within the replicon, restriction digestion and sticky-end cloning were employed. Constructs containing MluI and NotI restriction digest sites with identical 5′ TR of each strain, except for mutations in the cyclization sequences matching that of the designed mutants, were ordered from Genewiz. These constructs were then transformed into NEB DH5α cells and

purified using a Maxiprep kit. The isolated plasmid was subjected to double digestion with MluI and NotI for 4 hours at 37 °C. After incubation, the samples were assessed on a 1% agarose gel for 30 minutes and subsequently stained with Sybersafe™ to visualize the separate digested backbone and insert fragments. Once the insert and backbone were identified, the bands were excised and purified using a Monarch Gel extraction kit (New England Biolabs). Purified fragments were then utilized for further ligation. After both the replicon backbone and the mutated insert were purified, the fragments were mixed, and T4 DNA ligase was added and incubated for 2 hours at 37 °C to facilitate the ligation of the insert into the replicon backbone. The sample was then transformed into NEB5α cells, and any colonies that grew were selected and purified through New England Biolabs Monarch® miniprep kits. Sequencing was performed to ensure proper mutation of the CS.

Next, Huh7 cells were transfected with the replicons through electroporation, as previously described (44, 45). Replicon RNA was produced through the previously mentioned *in vitro* transcription (IVT) protocol, with the addition of 5 mM GTP. Purification of replicon RNA can be seen in **Supplemental Figure 2.2**. A 5′-methylcap analog was used at a concentration of 10 mM during the IVT reaction. RNA produced through the IVT was purified using a New England Biolabs RNA cleanup kit, and purity was checked on a 1% agarose gel. For electroporation, subconfluent and trypsinized cells were collected in DMEM, washed once with PBS and resuspended in cytomix buffer (120 mM KCl, 0.15 mM CaCl2, 10 mM potassium phosphate buffer, 25 mM HEPES (pH 7.6), 2 mM EGTA, 5 mM MgCl2, freshly supplemented with 2 mM ATP) at a concentration of 1×10^7 cells/mL for Huh7. Four hundred µL of the cell suspension was mixed with 10 µg of in vitro transcribed RNA, transferred into an electroporation cuvette (Invitrogen™, ThermoScientific, MA, USA; 0.4-cm gap width), and pulsed once with a Gene

Pulser Xcell system (Bio-Rad) at 975 μF and 270 V. Finally, 100 μL of the cells were transferred into 6 mL of pre-warmed DMEM. For replication assays, Huh7 cells transfected with replicon RNAs were seeded into 6-well plates at a density of 4×10^5 cells/well, and for the negative control, NITD008 was added to the cells at a concentration of 5 μM. After 48 hours, cells were lysed by the addition of 350 μL luciferase lysis buffer (25 mM Glycine-Glycine (pH 7.8), 15 mM $MgSO_4$; 4 mM EGTA, 10% (v/v) glycerol, 0.1% (v/v) Triton X-100, freshly added 1 mM DTT) to each well. Repeated freeze-thaw cycles were performed, and the lysates were stored at −80 ◦C until use for luciferase assays. Luciferase activity was determined with a SpectraMax® i3x microplate reader (Molecular Devices, San Jose, USA). For each sample, 20 μL of cell lysate was mixed with 100 μL freshly prepared luciferase assay buffer (25 mM Glycine-Glycine (pH 7.8), 15 mM K4PO4 buffer (pH 7.8), 15 mM MgSO4, 4 mM EGTA, 7.42 μM coelenterazine), assay was performed in triplicate (46). Replication efficiency was reported as a percentage of replication relative to wild-type, and an unpaired t-test was used to determine significance.

2.5- Results

2.5.1- Computational Analysis of Cyclization Propensities

After performing the computational analysis on the minimum free energy TRs, models representing the terminal region interactions were generated and are shown in **Figure 2.2**, with the 5′ TR in green and the 3′ TR in red. Differences in the total amount of base pairing once co-folded produced variations in the free energy of binding between the strains. The free energies of the interactions determined through energy minimization are represented as -15.59 for H/PF/2013 and -18.50 for MR766, demonstrating a variation in the free energy.

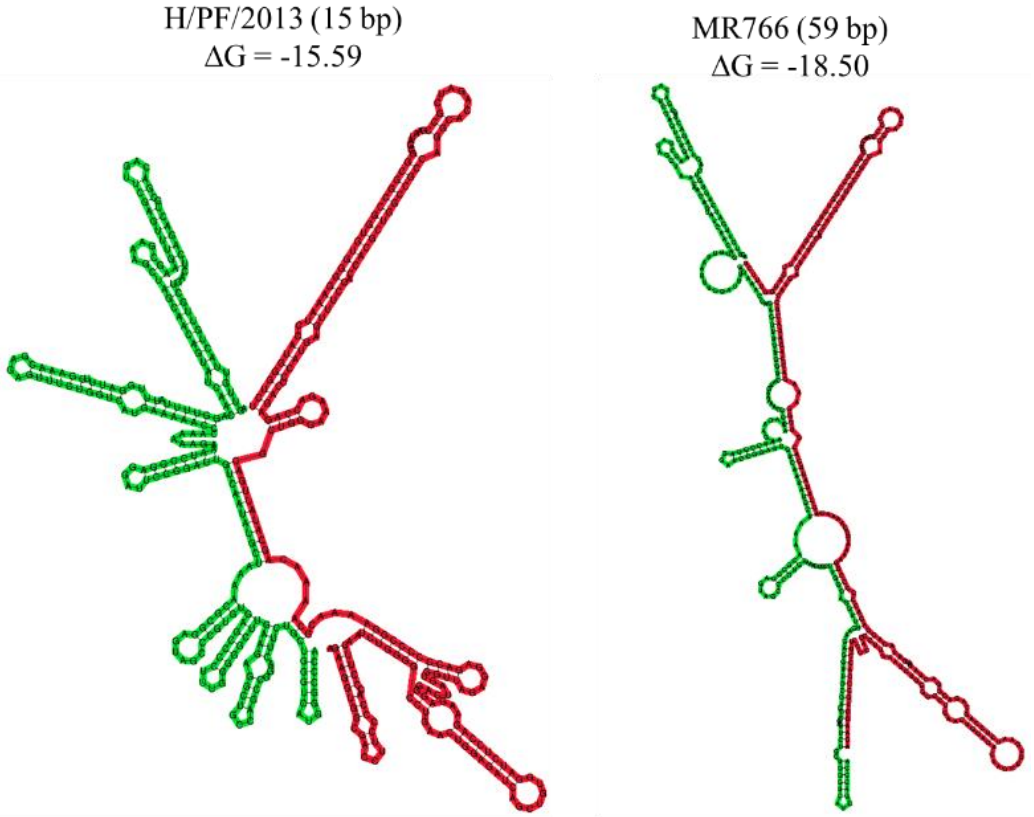

Figure 2.2: Visual representation of predicted long-range interactions between the terminal regions of ZIKV. The 5′ terminal region (green) and the 3′ terminal region (red) are shown based on Co-folded minimum free energy structures. The reported ΔG values represent the binding free energy, calculated as the difference between the free energies of the individually folded regions and the co-folded dimer structure.

2.5.2- Purification of ZIKV Terminal Regions for Interaction Studies Through *in vitro* Transcription

After IVTs were performed, RNA was purified using SEC. The elution profiles for individual RNA species are shown in **Figures 2.3A and 3C** for MR766 and HPF, respectively. These profiles indicate that RNA elutes at approximately 11-12 mL as a distinct RNA species, as the nucleotides of both the 5′TRs and 3′TRs are of similar nucleotide length; the elution peaks at this range for all species are expected. For the 3′WT of MR766 (**Figure 2.3A**, teal), it is observed that a plasmid or oligomerized species appears to elute at 10 mL; these fractions were excluded

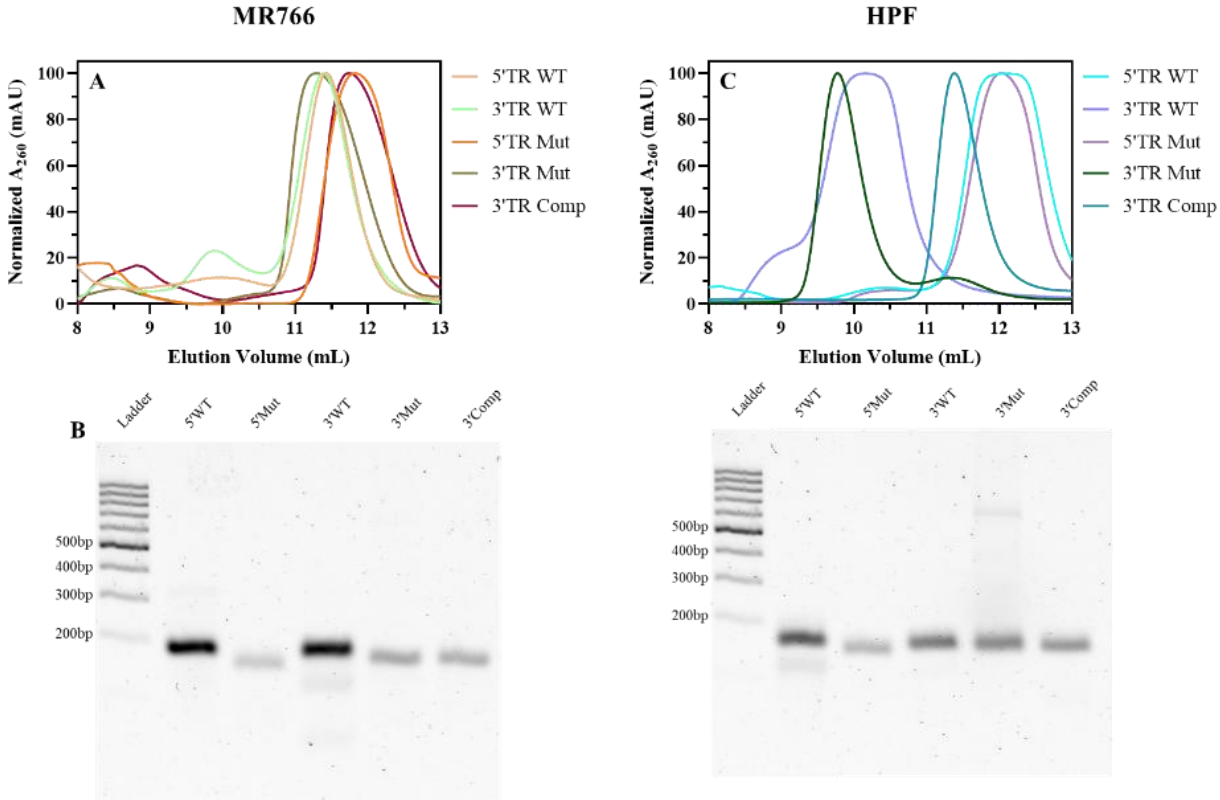

Figure 2.3: Purification of ZIKV TRs. After conducting *in vitro* transcription, RNA was purified using a Superdex 200 increase GL 10/300 column, and the elution profiles during purification can be observed in **(A)** for MR766 and **(C)** for HPF. For MR766, RNA was collected from 11.5 -12 mL for further experiments to avoid oligomerized states. HPF samples were collected at 12 mL for the 5′TR, 11.5 mL for the 3′Comp, and 10 mL for the 3′TR and Mut. All 3′ species of HPF were treated with DNase to remove residual DNA that was not removed during size exclusion. A 3% agarose gel of **(B)** MR766 and **(D)** HPF ZIKV sequences selected from the elution peaks was used to demonstrate the purity of the produced RNA. Single-size RNA can be seen around the 200 bp mark of the 100- 1000 bp DNA marker (BioBasic, Canada) as the transcripts are 210 nts and 221 nts for the 5′ and 3′ species, respectively.

from any downstream experimentation. For the 3′TRs of HPF, they elute at an earlier volume of 10 mL; this elution aligns with the elution of plasmid template and necessitated DNase treatments to eliminate any DNA from the RNA samples. Even with these DNase treatments, RNA elution for the 3′TRs of HPF occurred at an earlier volume compared to other 3′ species. Purified RNA species are visualized in **Figures 2.3B and 2.3D**, exhibiting single bands at the correct nucleotide size, indicating a homogeneous sample.

2.5.3- In Solution Characterization of 5′-3′ Interaction

Initial interaction studies were conducted using SEC as an initial method for determining binding. After incubating the various RNA pairings together at a 1:1 ratio and running the sample through size exclusion again, any interaction would be expected to produce a larger species, shifting the elution profile. These interactions are illustrated in **Figures 2.4A and B** for the MR766 and HPF interactions, respectively. From these elution traces, it is observed that the wild-type MR766 and HPF interactions produced a prominent peak prior to the typical elution volume of ~12 mL for MR766, and a peak eluting earlier than 10 mL for HPF. Analysis of RNA species was performed using SEC-MALS to confirm that the RNA is indeed monodispersed at high concentrations. **Figures 2.5A, B, D, and E** represent the individual RNA species of MR766 and HPFs 5′WT and 3′WT, respectively. From these MALS traces, a molecular weight can be determined through (Eq 1) at every scattering collection point. This molecular weight is then plotted as a black line, and a weight-average molecular weight is calculated. These weight averages correspond with the theoretical weight determined through programs such as Quest Calculate RNA

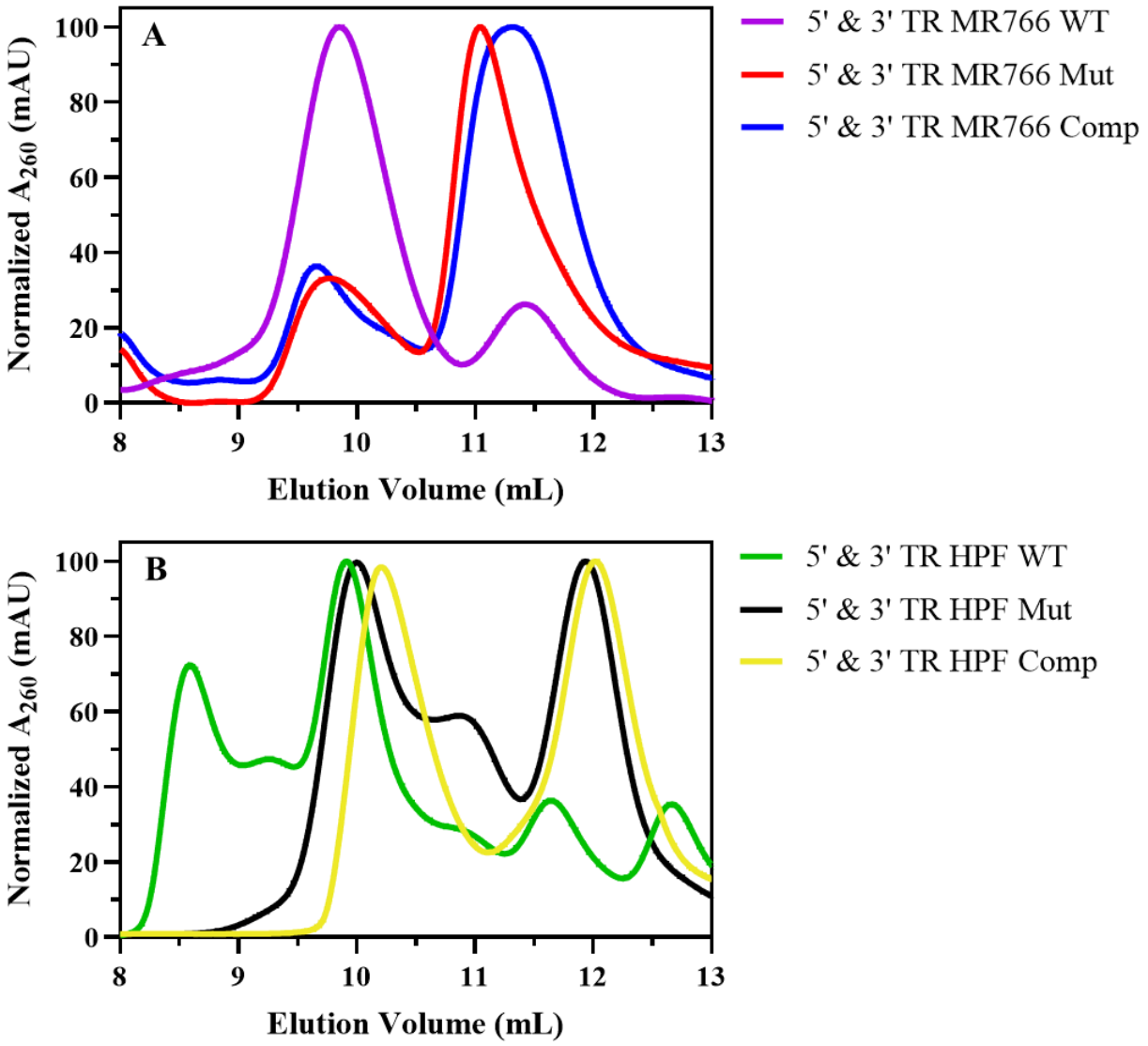

Figure 2.4: Initial interaction tested through size-exclusion chromatography. Elution profiles through the same Superdex 200 column demonstrate interactions for **(A)** MR766 and **(B)** HPF. Interaction studies were conducted at a 1:1 concentration of 500 nM for each species of RNA, and the interaction was then incubated for 1 hour at 25 °C. The appearance of an elution peak for the wild-type interactions to the left, around 10 mL for MR766 (purple) and 8.5 mL for HPF (green), indicates the formation of a larger species due to the interaction of the TRs. Elution profiles for both the mutant and compensatory interactions coincide with those of the individual species, indicating no complex formation occurred and the individual RNAs were able to be resolved through SEC.

Molecular Weight Calculator. Due to the weight determination matching that of a singular species, it can be concluded that the RNA exists in a monomeric form at concentrations as high as 1 mg/mL. This ensures that during further assays, these species will maintain their monomeric form, as the required concentrations are lower than 1 mg/mL. The interaction was subsequently investigated

through SEC-MALS, which enabled the calculation of the molecular weight of the interacting species, as shown in **Figures 2.5C and F**. The calculated molecular weight is close to the theoretical molecular weight of the complex, indicating a 1:1 stoichiometric interaction.

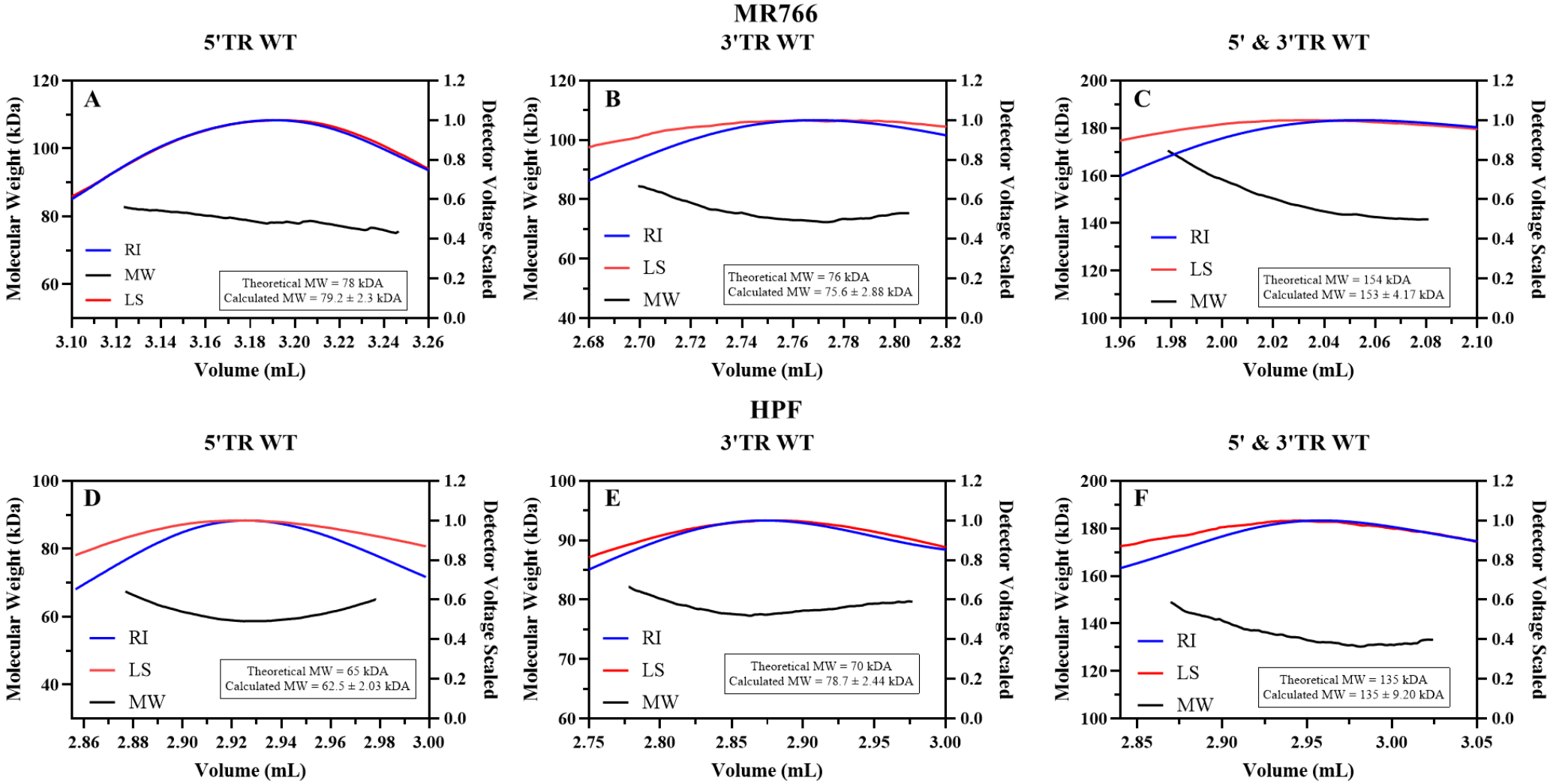

Figure 2.5: Absolute molecular weight determination of individual TRs as well as the interaction stoichiometries using SEC-MALS. The absolute molecular weight distribution across the elution peak of the individual species is shown for the **(A)** 5′ TR MR766, **(B)** 3′ TR MR766, **(C)** 5′ TR HPF, and **(D)** 3′ TR HPF. The experimentally determined molecular weight values align with those derived from the nucleotide sequences, indicating that the TRs we prepared are monomeric in solution. The interaction of the wild-type species was conducted with a 1:1 concentration of RNA and incubated for 1 hour at 25 °C. The absolute molecular weights for the interaction of the MR766 TRs **(C)** and HPF TRs **(D)** was determined using SEC-MALS. The calculated molecular weights of these interactions correspond to a 1:1 stoichiometry of interaction for these RNA species.

Following the determination of a 1:1 stoichiometry, we were then able to further assess the binding affinity of the interaction through MST. After performing the MST assay, we determined the Kd values of the MR766 and HPF wild-type interactions to be 26 nM and 157 nM, respectively. The MST traces for the MR766 interactions are shown in **Figure 2.6A**, while **6B** represents the HPF interactions with the wild-type, demonstrating full fraction bound. When

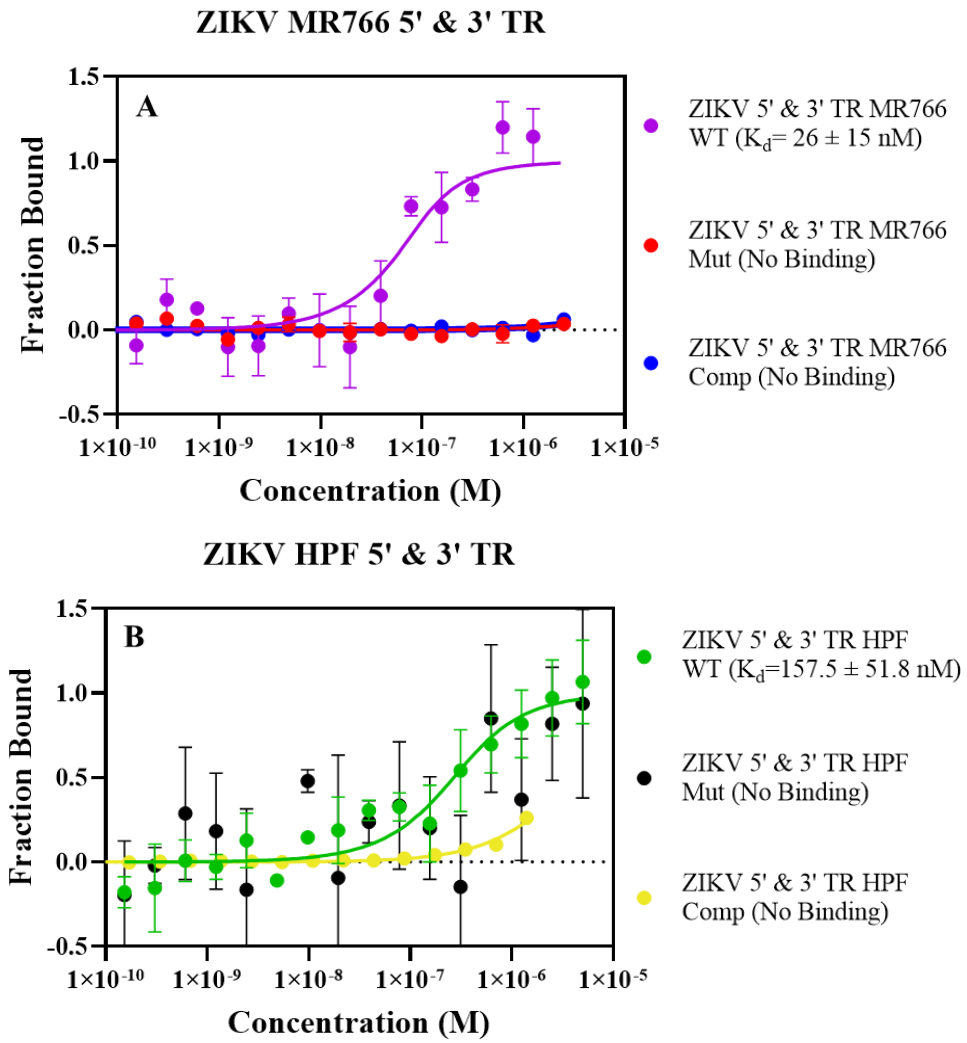

Figure 2.6: Affinity analysis of the TR cyclization interaction performed with MST. The microscale thermophoresis measurements are depicted through **(A)** representing the interaction of the TRs for the MR766 strains, while **(B)** depicts the interactions of the HPF strains. Fluorescently labelled 5′ TRs was used at a concentration of 100 nM and titrated against the 3′ TRs using a 2-fold serial dilution series from 76 pM to 2.5 µM. Dissociation constants were determined using the MST analysis software, determining that only wild-type interactions of MR766 (purple) and HPF (green) exhibit a binding interaction, while no dissociation constant can be determined from the mutant MR766 (red), mutant HPF (black) and compensatory interactions of MR766 (blue) and compensatory HPF (yellow).

examining the binding traces of the mutant and compensatory interactions in both, it can be seen that neither the mutant nor compensatory interactions produce sigmoidal profiles indicative of binding, as the MR766 species produces no curve, and the HPF curves contain too much noise to conclude binding.

2.5.4- Mutational Effects Exhibited Through Cellular Replicon Assays

After mutating the 5′ cyclization sequence within the replicon through cloning and producing replicon RNA, as shown in **Supplemental Figure 2.2**, the Huh7 cells were transfected with both the wild-type replicon and the mutant. The replication effects were observed in **Figure 2.7**. The replication of the RNA is normalized to the total luminescence of RLuc observed from the WT replicon, the mutant, and the negative control of NITD. It is then reported as a percentage of their replication efficiency. The adenosine analogue NITD was used as a negative control due to its inhibitory effects on the viral polymerase NS5. By incorporating during viral synthesis, further elongation cannot be performed, resulting in incomplete RNA transcripts. The wild-type exhibited high total luminescence, indicating effective replication, whereas the negative control with NITD008 showed lower total luminescence due to inhibition by the additive. Finally, when examining the mutant MR766 and HPF, it is evident that for both replicon strains, the total replication was significantly decreased ($p<0.0001$) in comparison to that of the wild-type, even more so than in the NITD additive conditions.

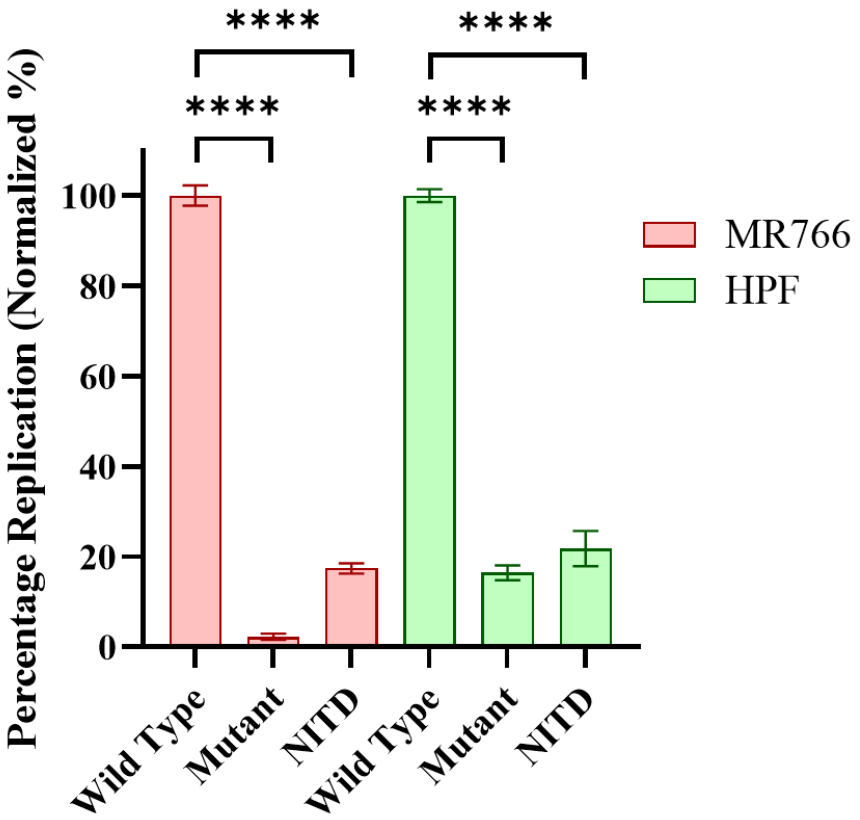

Figure 2.7: Replication efficiency of the TRs. Assessed using Huh7 mammalian cells and ZIKV MR766 and HPF replicon systems. Capped RNA was generated through *in vitro* transcription of replicon plasmids, and Huh7 cells were transfected through electroporation. Cells were lysed after 48 hours, and luciferase activity (RLuc) was determined through total luminescence. We normalized total RLuc values to that of the wild-type replication efficiency, presenting it as a percentage of replication. The NITD negative control shows a significant decrease in replication (****, $p<0.0001$) due to the incorporation halting further transcription. Meanwhile, the mutants display a drastic reduction (****, $p<0.0001$) in replication efficiency because of their inability to cyclize and initiate transcription.

2.6- Discussion & Conclusion

Initial computational analyses of interaction energies revealed that the Zika virus strain, MR766, exhibits a higher cyclization propensity, as indicated by a lower free energy value. In contrast, the Zika virus strain H/PF/2013 shows a lower cyclization propensity due to a higher free energy. While the overall RNA structural organization present within the terminal regions is conserved between strains, subtle nucleotide variations between them likely alter the number of thermodynamically favourable base-pairing interactions. These nucleotide variations could give rise to the increased number of base pairs observed for the co-folded MR766 TR interaction.

Additionally, these energy differences may stem from strain-specific genome-wide pairing patterns that influence cyclization dynamics and indicate cyclization propensity (29). Given these differences in cyclization propensities, we selected both strains to investigate whether the cyclization sequence plays a critical role in each case; if so, it would demonstrate a higher specificity. Demonstrating specificity in the interaction despite these energy differences would underscore the importance of the cyclization sequence.

Initial SEC interaction studies showed a leftward shift in elution volume for the wild-type RNA species **(Figure 2.4A and B)**, indicating the formation of larger complexes. This shift confirms successful interaction between the two wild-type terminal regions. In contrast, the elution profiles for the mutant and compensatory RNA species maintain peaks coinciding with those of the individual RNAs, showing no peak shifts. This indicates that these mutant species remained monomeric throughout incubation and were effectively resolved by size-exclusion chromatography (SEC). Using SEC-MALS, we determined that the interaction occurs with a 1:1 stoichiometry, as evidenced by the molecular weight calculations shown in **Figure 2.5C and F** (47). This finding is critical since these terminal regions originate from the same genome and must interact intramolecularly to achieve proper cyclization (29, 34, 48). Confirming a 1:1 stoichiometry is especially important for future kinetic assays because the presence of higher-order complexes would complicate the determination of kinetic constants such as binding affinity due to multi-step binding mechanisms (49, 50). Following stoichiometric confirmation, we measured the binding affinities using MST, a method well-suited for this type of interaction (42, 43, 51). The experimentally determined dissociation constants (K_d) align well with our *ab initio* modelling: MR766 exhibits a higher affinity and greater potential for cyclization compared to H/PF/2013, which shows lower affinity and has a lower potential for cyclization. These results correlate with

previous research indicating that the MR766 strain exhibits higher virulence compared to H/PF/2013, as well as differences in replication efficiency and innate immune response activation in human cells between both strains (36, 52). The higher affinity for cyclization in MR766 may contribute to increased virulence and variations in replication and immune outcomes. With the binding affinities of the wild-type interactions determined, we next assessed the significance and specificity of the cyclization sequence by analyzing mutant and compensatory interactions **(Figure 2.6 B)**. Both mutants and compensatory mutants showed no detectable interaction. This was demonstrated by MR766 mutants and HPF compensatory mutants, which exhibited no sigmoidal binding curve even at high concentrations. In contrast, the H/PF/2013 mutant displayed a high error between replicates with a weak signal below the threshold for reliable interaction detection (42). This error between replicates could be due to slight interactions influenced by the capillary; the addition of detergents, such as Tween-20, can reduce this capillary effect. Overall, this suggests that sequence changes disrupt the terminal region interaction, and compensatory base pairing is insufficient to restore the interaction, indicating that base pairing alone is inadequate to promote the interaction. Thus, the wild-type sequence is essential for facilitating cyclization.

Furthermore, replication assays using mutant MR766 and H/PF/2013 replicons demonstrated a significant decrease in overall replication efficiency, surpassing the inhibitory effect observed with the NITD additive. This inhibition exceeds that of the NITD control, which may be attributed to the inhibition method. The incorporation of NITD halts further RNA synthesis, necessitating the random chance of the analog being present near NS5 during the synthesis process. If the analog is absent, complete transcription can occur; this contrasts with the inhibition caused by mutations within the CS. Should these mutations disrupt the cyclization interaction, transcription cannot be initiated, which could lead to lower replication efficiency

compared to the negative control. These findings align with previous studies indicating that mutations within the CS impede replication, confirming that our selected mutations exhibit the same influence (53). Research has also demonstrated that mutations within the CS of Dengue don't impact the translational efficiency, indicating these observed effects are due to genome replication differences (54). The replication defects correlate well with the loss of binding affinity observed in MST, underscoring the critical role of the cyclization sequence in viral replication. Through this study, we have employed a combination of biophysical techniques (SEC, MALS, MST) and cell culture assays to demonstrate that the sequence specificity of the cyclization interaction between the terminal regions of two ZIKV strains is mediated by a conserved sequence that is specific to the 11-nucleotide cyclization sequence. Initial studies have suggested that this cyclization is enhanced through specific base pairing interactions, facilitating the formation of the panhandle (28, 31). Our data suggest that not only is primary base pairing essential, but also that secondary or tertiary structures influenced by the nucleotide order are crucial for cyclization. This contrasts with previous findings in other flaviviruses like Kunjin, where base pair order was less significant for cyclization but did reduce overall efficiency (28).

Overall, our results establish that for the Zika virus, the precise order of base pairs is a key determinant of interaction specificity. Cell culture assays further confirmed that mutations disrupting the cyclization sequence impair viral replication, which is consistent with prior findings (53). These insights enhance our understanding of the regulatory mechanisms controlling ZIKV replication. Given the conservation of cyclization sequences across flaviviruses, these findings could guide the development of broad-spectrum antiviral therapeutics targeting this critical interaction. We hope this work encourages further research into inhibiting cyclization as a strategy to disrupt viral replication.

2.7- Supplemental Data

Supplemental Table 2.1: **Complete sequences of each transcript of RNA.** Each sequence contains a T7 promoter highlighted in green, and a XbaI cut site highlighted in red. The cyclization sequence of each transcript is highlighted in blue.

Transcript	5'WT MR766	3'WT MR766	5'Mut MR766	3'Mut MR766	3'Comp MR766
Sequence	TAATACGACTCACTATAGGGAGT TGTTGATCTGTGTGAGTCAGACT GCGACAGTTCGAGTCTGAAGCGA GAGCTAACAACAGTATCAACAG GTTTAATTTGGATTTGGAAACGA GAGTTTCTGGTCATGAAAAACCC CAAAGAAGAAATCCGGAGGATC CGGATTGTCAATATGCTAAAACG CGGAGTAGCCCGTGTAAACCCCT TGGGAGGTTTGAAGAGGTTGCCA GCCGGACTTCTGCTGGGTCATGG ACCCATCTAGA	TAATACGACTCACTATAGGGAGA AGGTGGCGACCTTCCCCACCCTT CAATCTGGGGCCTGAACTGGAGA CTAGCTGTGAATCTCCAGCAGAG GGACTAGTGGTTAGAGGAGACC CCCCGGAAAACGCAAAACAGCA TATTGACGTGGGAAAGACCAGA GACTCCATGAGTTTCCACCACGC TGGCCGCCAGGCACAGATCGCC GAACTTCGGCGGCCGGTGTGGGG AAATCCATGGTTTCTTCTAGA	TAATACGACTCACTATAGGGAGT TGTTGATCTGTGTGAGTCAGACT GCGACAGTTCGAGTCTGAAGCGA GAGCTAACAACAGTATCAACAG GTTTAATTTGGATTTGGAAACGA GAGTTTCTGGTCATGAAAAACCC CAAAGAAGAAATCCGGAGGATC CGGATTTCTGAACTTAGAAAACG CGGAGTAGCCCGTGTAAACCCCT TGGGAGGTTTGAAGAGGTTGCCA GCCGGACTTCTGCTGGGTCATGG ACCCATCTAGA	TAATACGACTCACTATAGGGAGA AGGTGGCGACCTTCCCCACCCTT CAATCTGGGGCCTGAACTGGAGA CTAGCTGTGAATCTCCAGCAGAG GGACTAGTGGTTAGAGGAGACC CCCCGGAAAACGCAAAACAAAC TAGTGCTGTGGGAAAGACCAGA GACTCCATGAGTTTCCACCACGC TGGCCGCCAGGCACAGATCGCC GAACTTCGGCGGCCGGTGTGGGG AAATCCATGGTTTCTTCTAGA	TAATACGACTCACTATAGGGAGA AGGTGGCGACCTTCCCCACCCTT CAATCTGGGGCCTGAACTGGAGA CTAGCTGTGAATCTCCAGCAGAG GGACTAGTGGTTAGAGGAGACC CCCCGGAAAACGCAAAACCTAA GTTCAGAGTGGGAAAGACCAGA GACTCCATGAGTTTCCACCACGC TGGCCGCCAGGCACAGATCGCC GAACTTCGGCGGCCGGTGTGGGG AAATCCATGGTTTCTTCTAGA
Transcript	**5'WT HPF**	**3'WT HPF**	**5'Mut HPF**	**3'Mut HPF**	**3'Comp HPF**
Sequence	TAATACGACTCACTATAGGGAGT TGTTGATCTGTGTGAATCAGACT GCGACAGTTCGAGTTTGAAGCGA AAGCTAGCAACAGTATCAACAG GTTTTATTTTGGATTTGGAAACGA GAGTTTCTGGTCATGAAAAACCC AAAAAAGAAATCCGGAGGATTC CGGATTGTCAATATGCTAAAACG CGGAGTAGCCCGTGTGAGCCCCT TTGGGGGCTTGAAGAGGCTGCCA GTCTAGA	TAATACGACTCACTATAGGGAGA AGGTGGCGACCTTCCCCACCCTT TAATCTGGGGCCTGAACTGGAGA TTAGCTGTGAATCTCCAGCAGAG GGACTAGTGGTTAGAGGAGACC CCCCGGAAAACGCAAAACAGCA TATTGACGCTGGGAAAGACCAG AGACTCCATGAGTTTCCACCACG CTGGCCGCCAGGCACAGATCGC CGAATAGCGGCGGCCAGTGTGG GGAAATCCATGGGTCTTCTAGA	TAATACGACTCACTATAGGGAGT TGTTGATCTGTGTGAATCAGACT GCGACAGTTCGAGTTTGAAGCGA AAGCTAGCAACAGTATCAACAG GTTTTATTTTGGATTTGGAAACGA GAGTTTCTGGTCATGAAAAACCC AAAAAAGAAATCCGGAGGATTC CGGATTCATTGATACTCAAAACG CGGAGTAGCCCGTGTGAGCCCCT TTGGGGGCTTGAAGAGGCTGCCA GTCTAGA	TAATACGACTCACTATAGGGAGA AGGTGGCGACCTTCCCCACCCTT TAATCTGGGGCCTGAACTGGAGA TTAGCTGTGAATCTCCAGCAGAG GGACTAGTGGTTAGAGGAGACC CCCCGGAAAACGCAAAACTCTTC GAACTAGCTGGGAAAGACCAGA GACTCCATGAGTTTCCACCACGC TGGCCGCCAGGCACAGATCGCC GAATAGCGGCGGCCAGTGTGGG GAAATCCATGGGTCTTCTAGA	TAATACGACTCACTATAGGGAGA AGGTGGCGACCTTCCCCACCCTT TAATCTGGGGCCTGAACTGGAGA TTAGCTGTGAATCTCCAGCAGAG GGACTAGTGGTTAGAGGAGACC CCCCGGAAAACGCAAAACGAGT ATCAATGGCTGGGAAAGACCAG AGACTCCATGAGTTTCCACCACG CTGGCCGCCAGGCACAGATCGC CGAATAGCGGCGGCCAGTGTGG GGAAATCCATGGGTCTTCTAGA

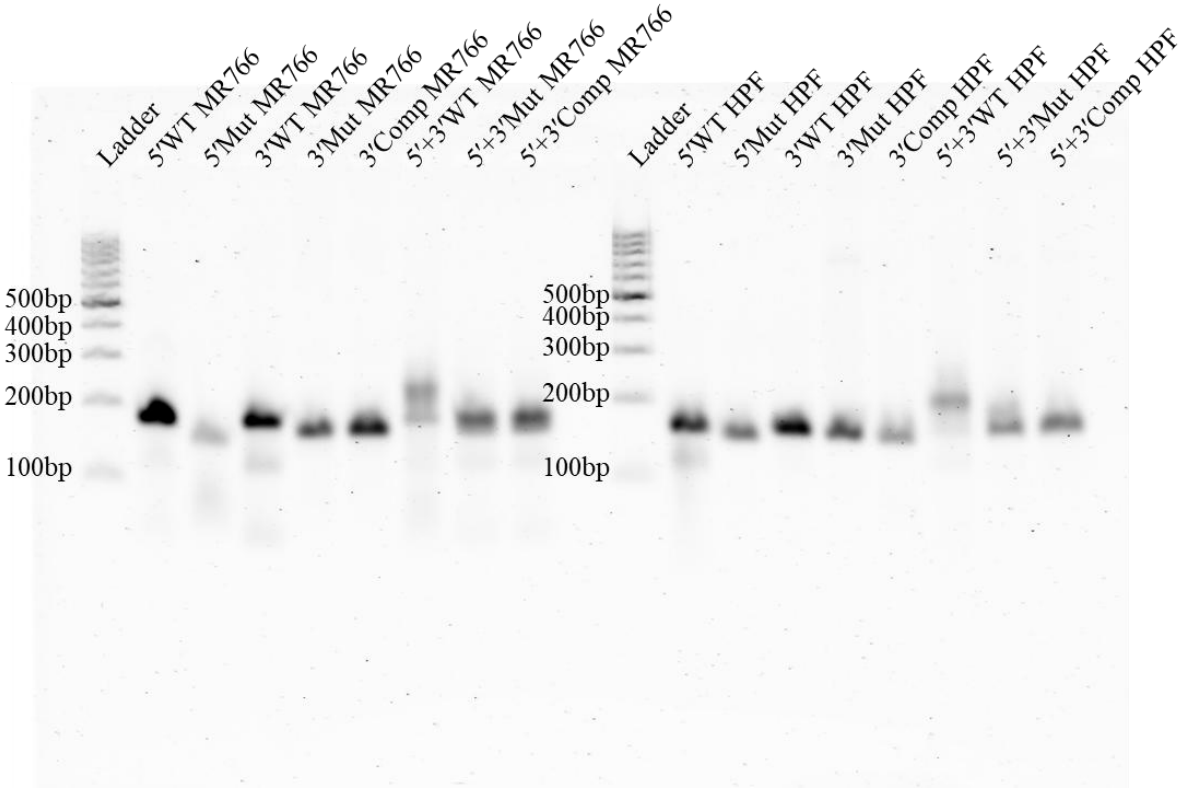

Supplemental Figure 2.1: Electrophoretic Mobility Shift assay of the ZIKV TR interactions. Performed on a 3% TB agarose gel run at 100V for 50 minutes. Interactions were mixed at a 1:1 ratio with a final concentration of 500 nM and incubated for 1 hour at 25 °C. All individual RNA species were run at a 1 μM concentration. Shift in migration of 5′+3′WT TRs when compared to individual species is indicative of interaction between two RNA components**.**

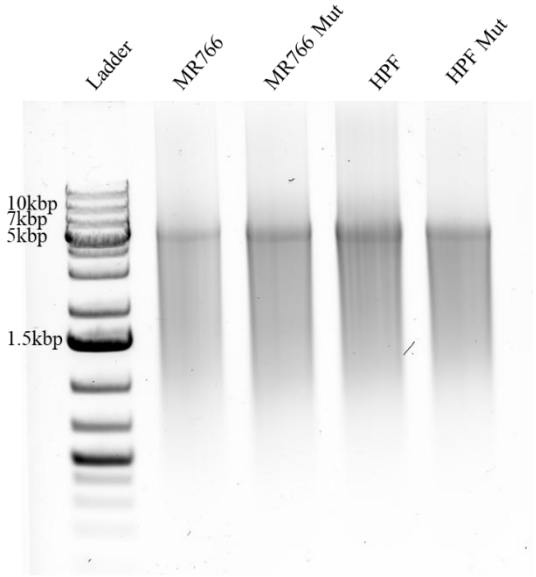

Supplemental Figure 2.2: Purification of ZIKV Replicon RNA. A 1% agarose gel after *in vitro* transcription of the ZIKV replicons, RNA was purified through the use of New England Biolabs RNA cleanup kit. Mutations of the replicon plasmid were performed in the 5'CS through cloning and confirmed through Sanger sequencing.

2.8- References

1. S. I. Yun, Y. M. Lee, Zika virus: An emerging flavivirus. *Journal of Microbiology* **55**, 204–219 (2017).
2. D. Musso, E. J. Nilles, V. M. Cao-Lormeau, Rapid spread of emerging Zika virus in the Pacific area. *Clinical Microbiology and Infection* **20**, O595–O596 (2014).
3. R. Lowe, *et al.*, The zika virus epidemic in brazil: From discovery to future implications. *Int J Environ Res Public Health* **15** (2018).
4. A. Gulland, Zika virus is a global public health emergency, declares WHO. *BMJ* **352**, i657 (2016).
5. D. Musso, D. J. Gubler, Zika Virus. *Clin Microbiol Rev* **29**, 487–524 (2016).
6. B. H. Song, S. I. Yun, M. Woolley, Y. M. Lee, Zika virus: History, epidemiology, transmission, and clinical presentation. *J Neuroimmunol* **308**, 50–64 (2017).
7. Y. J. S. Huang, S. Higgs, K. M. E. Horne, D. L. Vanlandingham, Flavivirus-Mosquito Interactions. *Viruses* **6**, 4703 (2014).
8. V. Sharma, *et al.*, Zika virus: An emerging challenge to public health worldwide. *Can J Microbiol* **66**, 87–98 (2020).
9. Zika virus disease – India. Available at: https://www.who.int/emergencies/disease-outbreak-news/item/2025-DON549 [Accessed 28 May 2025].
10. M. A. McArthur, Zika Virus: Recent Advances towards the Development of Vaccines and Therapeutics. *Viruses* **9** (2017).
11. C. Shan, *et al.*, A live-attenuated Zika virus vaccine candidate induces sterilizing immunity in mouse models. **23** (2017).
12. B. H. Song, *et al.*, Comparison of Three Chimeric Zika Vaccine Prototypes Developed on the Genetic Background of the Clinically Proven Live-Attenuated Japanese Encephalitis Vaccine SA14-14-2. *Int J Mol Sci* **26** (2024).
13. M. V. Mancini, *et al.*, Evaluation of an Engineered Zika Virus-Like Particle Vaccine Candidate in a Mosquito-Mouse Transmission Model. *mSphere* **8** (2023).
14. Y. Wang, A. Marin-Lopez, J. Jiang, M. Ledizet, E. Fikrig, Vaccination with aedes aegypti agbr1 delays lethal mosquito-borne zika virus infection in mice. *Vaccines (Basel)* **8** (2020).
15. P. Brasil, *et al.*, Guillain-Barré syndrome associated with Zika virus infection. *The Lancet* **387**, 1482 (2016).
16. F. Krauer, *et al.*, Zika Virus Infection as a Cause of Congenital Brain Abnormalities and Guillain–Barré Syndrome: Systematic Review. *PLoS Med* **14** (2017).
17. N. Zhang, *et al.*, Zika Virus Disrupts Neural Progenitor Development and Leads to Microcephaly in Mice. *Cell Stem Cell* **19**, 120–126 (2016).

18. I. Gladwyn-Ng, *et al.*, Stress-induced unfolded protein response contributes to Zika virus-associated microcephaly. *Nat Neurosci* **21**, 63–73 (2018).

19. D. Xu, C. Li, C. F. Qin, Z. Xu, Update on the Animal Models and Underlying Mechanisms for ZIKV-Induced Microcephaly. *Annu Rev Virol* **6**, 459–479 (2019).

20. P. Li, *et al.*, Integrative Analysis of Zika Virus Genome RNA Structure Reveals Critical Determinants of Viral Infectivity. *Cell Host Microbe* **24**, 875-886.e5 (2018).

21. W. C. Ng, R. Soto-Acosta, S. S. Bradrick, M. A. Garcia-Blanco, E. E. Ooi, The 5′ and 3′ Untranslated Regions of the Flaviviral Genome. *Viruses* **9**, 137 (2017).

22. M. A. Garcia-Blanco, S. G. Vasudevan, S. S. Bradrick, C. Nicchitta, Flavivirus RNA transactions from viral entry to genome replication. *Antiviral Res* **134**, 244–249 (2016).

23. A. Slonchak, *et al.*, Structural analysis of 3'UTRs in insect flaviviruses reveals novel determinants of sfRNA biogenesis and provides new insights into flavivirus evolution. *Nat Commun* **13** (2022).

24. Y. Song, J. A. Mugavero, C. B. Stauft, E. Wimmer, Dengue and Zika Virus 5' Untranslated Regions Harbor Internal Ribosomal Entry Site Functions. *mBio* **10** (2019).

25. X. Chen, *et al.*, The subgenomic flaviviral RNA suppresses RNA interference through competing with siRNAs for binding RISC components. *J Virol* **98** (2024).

26. D. E. Alvarez, A. L. De Lella Ezcurra, S. Fucito, A. V. Gamarnik, Role of RNA structures present at the 3′UTR of dengue virus on translation, RNA synthesis, and viral replication. *Virology* **339**, 200–212 (2005).

27. M. T. Wolfinger, R. Ochsenreiter, I. L. Hofacker, Functional RNA Structures in the 3'UTR of Mosquito-Borne Flaviviruses. (2021).

28. A. A. Khromykh, H. Meka, K. J. Guyatt, E. G. Westaway, Essential Role of Cyclization Sequences in Flavivirus RNA Replication. *J Virol* **75**, 6719 (2001).

29. R. G. Huber, *et al.*, Structure mapping of dengue and Zika viruses reveals functional long-range interactions. *Nature Communications 2019 10:1* **10**, 1–13 (2019).

30. C. Mazeaud, W. Freppel, L. Chatel-Chaix, The Multiples Fates of the Flavivirus RNA Genome During Pathogenesis. *Front Genet* [Preprint] (2018).

31. C. S. Hahn, *et al.*, Conserved elements in the 3' untranslated region of flavivirus RNAs and potential cyclization sequences. *J Mol Biol* **198**, 33–41 (1987).

32. G. P. Göertz, S. R. Abbo, J. J. Fros, G. P. Pijlman, Functional RNA during Zika virus infection. *Virus Res* [Preprint] (2018).

33. T. Fajardo, *et al.*, The flavivirus polymerase NS5 regulates translation of viral genomic RNA. *Nucleic Acids Res* **48**, 5081–5093 (2020).

34. X.-D. Li, C.-L. Deng, Z.-M. Yuan, H.-Q. Ye, B. Zhang, Different Degrees of 5'-to-3' DAR Interactions Modulate Zika Virus Genome Cyclization and Host-Specific Replication. *J Virol* **94** (2020).

35. T. Mrozowich, *et al.*, Investigating RNA-RNA interactions through computational and biophysical analysis. *Nucleic Acids Res* **51**, 4588–4601 (2023).

36. Q. Shao, *et al.*, The African Zika virus MR-766 is more virulent and causes more severe brain damage than current Asian lineage and dengue virus. *Development* **144**, 4114 (2017).

37. R. Lorenz, *et al.*, ViennaRNA Package 2.0. *Algorithms for Molecular Biology* **6** (2011).

38. J. Stetefeld, S. A. McKenna, T. R. Patel, Dynamic light scattering: a practical guide and applications in biomedical sciences. *Biophys Rev* **8**, 409–427 (2016).

39. P. J. Wyatt, Light scattering and the absolute characterization of macromolecules. *Anal Chim Acta* **272**, 1–40 (1993).

40. D. L. Gemmill, *et al.*, The 3′ terminal region of Zika virus RNA contains a conserved G-quadruplex and is unfolded by human DDX17. *Biochemistry and Cell Biology* **102**, 96–105 (2024).

41. R. F. Johnson, S. E. McCarthy, P. J. Godlewski, R. N. Harty, Ebola virus VP35-VP40 interaction is sufficient for packaging 3E-5E minigenome RNA into virus-like particles. *J Virol* **80**, 5135–5144 (2006).

42. T. Mrozowich, V. Meier-Stephenson, T. R. Patel, Microscale thermophoresis: warming up to a new biomolecular interaction technique. *Biochem (Lond)* **41**, 8–12 (2019).

43. M. Jerabek-Willemsen, *et al.*, MicroScale Thermophoresis: Interaction analysis and beyond. *J Mol Struct* **1077**, 101–113 (2014).

44. A. Kumar, *et al.*, Nuclear Localization of Dengue Virus Nonstructural Protein 5 Does Not Strictly Correlate with Efficient Viral RNA Replication and Inhibition of Type I Interferon Signaling. *J Virol* **87**, 4545–4557 (2013).

45. M. Münster, *et al.*, A reverse genetics system for Zika virus based on a simple molecular cloning strategy. *Viruses* **10** (2018).

46. A. Kumar, *et al.*, Nuclear Localization of Dengue Virus Nonstructural Protein 5 Does Not Strictly Correlate with Efficient Viral RNA Replication and Inhibition of Type I Interferon Signaling. *J Virol* **87**, 4545 (2013).

47. D. Some, Light-scattering-based analysis of biomolecular interactions. *Biophys Rev* **5**, 147 (2013).

48. D. E. Alvarez, M. F. Lodeiro, S. J. Ludueña, L. I. Pietrasanta, A. V. Gamarnik, Long-Range RNA-RNA Interactions Circularize the Dengue Virus Genome. *J Virol* **79**, 6631 (2005).

49. F. Battiston, *et al.*, The physics of higher-order interactions in complex systems. *Nature Physics 2021 17:10* **17**, 1093–1098 (2021).

50. Y. Deng, A. K. Efremov, J. Yan, Modulating binding affinity, specificity, and configurations by multivalent interactions. *Biophys J* **121**, 1868 (2022).

51. C. Nelson, *et al.*, Human DDX3X Unwinds Japanese Encephalitis and Zika Viral 5 Terminal Regions Human DDX3X Unwinds Japanese. *Terminal Regions. Int. J. Mol. Sci* **2021**, 413 (2021).

52. P. Österlund, *et al.*, Asian and African lineage Zika viruses show differential replication and innate immune responses in human dendritic cells and macrophages. *Scientific Reports 2019 9:1* **9**, 1–15 (2019).

53. T. J. Sanford, H. V. Mears, T. Fajardo, N. Locker, T. R. Sweeney, Circularization of flavivirus genomic RNA inhibits de novo translation initiation. *Nucleic Acids Res* **47**, 9789–9802 (2019).

54. W.-W. Chiu, R. M. Kinney, T. W. Dreher, Control of Translation by the 5′- and 3′-Terminal Regions of the Dengue Virus Genome. *J Virol* **79**, 8303 (2005).

Chapter 3: Characterization of FXR1 protein and Zika Virus terminal RNA interactions

3.1- Foreword

This chapter is based on unpublished work performed with the help of Sierra Mazurek, Aysha Demeler, and Dr. Trushar Patel. I performed all wet laboratory experiments with assistance from Sierra Mazurek. AUC experiments were performed and analysed by Aysha Demeler. Jack Moore at the Alberta Proteomics and Mass Spectrometry Facility at the University of Alberta performed Mass spectroscopy analysis for verification. I have written the manuscript with the assistance of editing from Dr. Patel.

3.2- Introduction

3.2.1- Zika Virus

Zika virus (ZIKV) is a neurovirulent member of the *Flaviviridae* family, which in the last 10 years, has placed a heavy burden on health care systems across the globe. With outbreaks in Brazil affecting over 1.3 million people in 2015, and as recently as 2024, in India infecting 150, Zika currently threatens over 89 countries with potential transmission (1–3). This pressure is exacerbated by the potential for serious neurological syndromes, such as Guillain-Barré syndrome or gestational microcephaly, which cause damage to nerve cells, leading to potential muscle paralysis or abnormal cranial development within fetuses in *utero,* respectively (4–9). With no approved vaccine or therapy, there is high pressure to identify a potential treatment (10–12). During infection, the ZIKV genome, approximately 11,000 nucleotides (nt), is used to translate 3 structural and 7 non-structural proteins that aid in viral replication and packaging (13). During viral replication, ZIKV remodels the membrane of the endoplasmic reticulum (ER) to form a replication organelle (RO), which facilitates further genome replication and the packaging of viral capsids (14–16). The identification of other membrane-bound organelles in ZIKV and other members of the Flavivirus genus has been shown to be crucial to the virus replication (17, 18). A set of untranslated terminal regions (UTR) at the 5′ and 3′ end flank the coding region; in contrast, although unable to translate viral proteins, these regions are still influential in viral replication and immune evasion (19). Through interactions with themselves or interactions with various host and viral proteins, these TRs are crucial to the viral life cycle (20).

3.2.2- Host protein interactions re-exhibited

During viral infection, host proteins play a crucial role in facilitating viral replication by interacting with viral proteins and the viral genome. Viral proteins are produced to aid in the proliferation of the virus. These viral proteins can assist in viral replication in various ways, from performing transcription, facilitating viral packaging, and moonlighting as suppressors of immune response pathways (13, 21–25). However, various host proteins are often recruited to facilitate the function of these viral proteins, such as the RNA-dependent RNA polymerase NS5, which interacts with host nucleolin to increase replication (26). The number of viral proteins produced is also limited, and without cellular machinery hijacked from the host, replication is not possible (27–29). These host proteins have been found to facilitate the viral life cycle, ranging from cellular entry to viral replication, and finally egress (28, 29). This discovery has led researchers to investigate the potential proteins that act as proviral elements, furthering their understanding of the role our cellular machinery plays in the virus's infection. As discussed previously in **Chapter 1**, the interaction of host proteins with the TR of ZIKV plays a crucial role in the virus's ability to replicate, as well as a mechanism for immune evasion.

3.2.3- Role of FXR1

Fragile X-related protein 1 (FXR1) is a multi-functional RNA-binding protein that has been identified to regulate RNA metabolism through miRNA processing and maturation, transportation of mRNA between the nucleus and cytoplasm, and regulation of mRNA translation (30, 31). FXR1 has also demonstrated the ability to form liquid condensates through liquid-liquid phase separation (LLPS), which is promoted through the intrinsically disordered region of its C-terminal domain (32–34). The formation of these condensates by FXR1 has been shown to influence spatial localization and promote the translation of mRNA, as well as regulate the organization of

ribonucleoprotein complexes, and aid in RO formation, which is essential for coronaviruses (32, 33, 35). A study also demonstrated that FXR1 was an important proviral protein in the stability of Human Adenovirus mRNA, specifically the HAdV-5 major late transcription unit mRNA, which is necessary for producing capsid proteins from mRNA, highlighting its importance in viral replication (36). Part of the FXR family, FXR1 is a homolog of Fragile X mental retardation protein 1 (FMRP), which has been shown to play a crucial role in neuronal fragile X syndrome, a prominent factor in autism (30, 37, 38). These homologs have been identified to exhibit expression patterns in developing neurons, as well as FXR1, which controls protein synthesis at synapses within the central nervous system (31, 39). The recent findings underscore the significance of these proteins within the nervous system, and their direct or indirect association with various mental disorders or immune-related conditions (30, 40). Previous literature has also demonstrated that FMRP is antagonized during Zika infection by sfRNA, which acts as a means to interfere with FMRP, as it functions as a restriction factor for Zika (41). In comparison, literature has shown an interaction between the 3′ TR of Zika and FXR1, but no further studies have been performed to characterize the implications of this interaction further, as well as whether FXR1 interacts with the 5′ TR.

Throughout the chapter, we aim to determine if an interaction exists between FXR1 and ZIKV TRs and gain further insight into whether the interaction is crucial to the virus's life cycle. Through immunoprecipitation pulldown assays performed by our lab, FXR1 was identified as a possible binding protein to both terminal regions of ZIKV, and it was also shown to interact with the 3′ TR through literature (41). As FXR1 is a translational regulator, we hypothesize that its interaction with the TRs of ZIKV could lead to increased translation efficiency, potentially through influencing the formation or function of ROs. The importance of FXR1 within developing

neuronal cells and ZIKV's ability to disrupt neuronal growth is also an interesting potential correlation (9, 30). Through the purification of recombinantly expressed FXR1, we biophysically characterized our purified protein through size-exclusion multi-angle light scattering and analytical ultracentrifugation. Using the purified protein, the interaction with ZIKV TRs was investigated through electromobility shift assays and microscale thermophoresis to determine the presence of direct binding between FXR1 and ZIKV TRs. Following the confirmation of a direct binding interaction, future directions could be employed, such as knockdown assays, to determine if FXR1 plays a crucial role in ZIKV during viral replication. This determination could inform the development of a future therapeutic designed to target the interaction between FXR1 and ZIKV, thereby disrupting the viral replication process.

3.3- Materials and Methods

3.3.1- FXR1 Purification

The original purification protocol utilized a full-length FXR1 sequence, comprising amino acids 1-621, with a C-terminal hexa-histidine tag. This sequence was then placed in a pET-28a+ vector for expression (42). For optimized purification attempts, a truncated sequence of FXR1 containing amino acids 1-460 ($FXR1_{1-460}$), which maintained the KH domains, the RGG RNA-binding box, and an N-terminal hexa-histidine tag, was used for purification. The sequence was placed into a pET-28a+ vector for expression and synthesized commercially by Genewiz® (Azenta). Once the vector was received, it was then transformed into competent *E. coli* lemo21 cells, which were grown on LB plates containing two antibiotics: kanamycin (50 mg/mL) and chloramphenicol (100 mg/mL) for selection. From this plate, a single colony was selected and placed into 50 mL of LB medium containing both kanamycin and chloramphenicol, and left to grow for 12 hours at 37 °C. Following incubation, 25 mL was added to 500 mL of LB medium containing both kan and cam. Cells were then incubated at 37 ℃ until an optical density (OD_{600}) of approximately 0.6 was reached. For initial purification attempts, 1 mM isopropyl β-D-1-thiogalactopyranoside (IPTG) was used for induction; however, following optimization, a concentration of 0.1 mM was found to be more effective for inducing protein expression. Expression was tested under both autoinduction media and LB media, and the concentration of IPTG was varied to 1 mM and 0.25 mM. Time points were taken at 2, 4, 8, 14, and 20 hours post-induction. Samples were then pelleted at 10,000 xg for 10 minutes, followed by lysis of the pellet using lysis buffer (20 mM Tris pH 8, 15 mM Imidazole, 500 mM NaCl, 0.3% CHAPS) with the addition of lysozyme (10 mg/mL), as well as 200 units of DNase I (ThermoScientific), 2 mM PMSF and sodium deoxycholate (12mg/g) and left to incubate on an orbital shaker for 1 hour.

Lysed samples were then mixed with 6x sample-reducing dye and incubated at 95 °C for 5 minutes before being run on an SDS-PAGE gel (6% stacking, 12% resolving) for 65 minutes at 200V in 1x SDS running buffer. A BLUelf™ (FroggaBio, Buffalo NY, USA) pre-stained ladder was used for size determination. The gel was then transferred onto a nitrocellulose membrane using a transfer-Blot Turbo (BioRad) transfer system on a mixed molecular weight setting. The blot was placed in a transfer buffer (25 mM Tris base, pH 7.6, 192 mM glycine) and incubated with constant rocking for 15 minutes at room temperature. It was then washed with 5% skim milk dissolved in 1x PBS for 2 hours, followed by three 10-minute washes with 1x PBST and a final 10-minute wash with 1x PBS. Following the final wash step, 1x PBS containing 0.5% skim milk and a 1:1000 dilution of mouse anti-histag antibody was incubated for 2 hours, followed by the same PBS and PBST washes. Lastly, 1x PBS containing 0.5% skim milk and a 1:2000 dilution of goat anti-mouse horseradish peroxidase conjugate antibody was incubated for 1 hour. After incubation, the sample was washed three times for 5 minutes each with 1x PBST and once with 1x PBS for 5 minutes. The membrane was then incubated with Immobilon western HRP substrate and imaged using an Amersham Imager 600.

Following this expression screening, the optimal condition of TB media at 37 °C, followed by induction and incubation at 18 °C for 16 hours, was selected for further purification attempts. Following this incubation, cells were centrifuged at 5000 xg, at 4°C for 15 minutes. Next, the cells were resuspended and lysed using a lysis buffer, with the addition of lysozyme (10 mg/mL) as well as DNase (20 µL), PMSF (2mM), and sodium deoxycholate (12mg/mL), the lysate was then left to incubate for 20 minutes at 4°C. The suspended cells were then disrupted by sonication for approximately 10 minutes at 40 kHz with an amplitude of 60%. The lysate was clarified at 30,000 xg at 4°C for 45 minutes. The supernatant was then filtered through a 0.45 µm syringe filter. The

clarified supernatant was then purified using a 5mL His-Trap HP affinity column (Cytiva) on an ÄKTA start system (Global Life Science Solutions USA LLC, Marlborough, MA, USA). The column was then washed with 10 CV of lysis buffer, and the bound protein was eluted through a gradient of elution buffer (20 mM Tris, pH 7.5, 1 M Imidazole, 500 mM NaCl, 0.3% CHAPS) starting at 50 mM imidazole. Absorbance was recorded at 280 nm, and any fractions containing peaks were run on an SDS-PAGE (6% stacking, 12% resolving) as stated previously, using a molecular weight wide-range marker (116 kDa to 14.4 kDa from Bio Basic Inc., Markham, ON, Canada) for size determination.

Fractions that contained proper band sizes were collected and concentrated using a 30,000 MW cutoff Millipore centricon, anion exchange chromatography was then performed through a MonoQ anion exchange column (Cytiva) using an ÄKTA pure FPLC system (Global Life Science Solutions USA LLC, Marlborough, MA, USA) using FXR1 SEC buffer (20 mM Tris pH 7.5, 250 mM NaCl, 5mM MgCl2, 0.3% CHAPS, 3% Glycerol) for elution. Absorbance was recorded at 280 nm and 260 nm, and any fractions containing peaks with a 280 nm absorbance higher than a 260 nm absorbance were run on an SDS-PAGE at 200V for 60 minutes. Fractions containing bands that were ~53 kDa were collected for further downstream assays. Protein purification of the insoluble fraction was also performed, denaturing the pellet using protein denaturing buffer (6M GuHCl, 500 mM NaCl, 15 mM Imidazole). The denatured fraction was then manually passed through a 1 mL His-Trap HP column (Cytiva), followed by a refolding step using 2 column volumes of refolding buffer (2 M GuHCl, 500 mM NaCl, 15 mM imidazole). The protein was then eluted using 5 column volumes of elution buffer.

3.3.2- Size-exclusion Multi-angle Light Scattering

Size-exclusion coupled with multi-angle light scattering (SEC-MALS) was employed to determine the monodispersity of the purified $FXR1_{1\text{-}460}$. $FXR1_{1\text{-}460}$ was concentrated to 0.5 mg/mL and was centrifuged at 10,000 xg for 2 minutes to remove any potential aggregates. The protein was then loaded into a ThermoScientific Vanquish HPLC, connected to a KW403.5-4F Shodex column used for separation. Following size exclusion, protein was passed through a Wyatt Dawn® (Wyatt Technology Corporation, Santa Barbara, CA, USA) MALS detector with 18 detector angles and a 658 nm laser. The refractive index was measured using an Optilab® refractometer (Wyatt Technology Corporation, Santa Barbara, CA, USA). The molecular weight of the protein was determined using the Astra v8.0.0.25 software with the Debye model, as shown in Eq. 1.

$$M_w = \frac{R(\theta)}{K*c} \quad (1)$$

Where K is the polymer constant, Eq. 2:

$$K = \frac{4\pi^2 n_0^2 (dn/dc)^2}{\lambda_0^4 N_A} \quad (2)$$

Where R(θ) is the Rayleigh Ratio of scattered light at an angle θ=0, c is the concentration of the solute in mg/mL determined from the refractive index, n is the refractive index of the solvent, λ_0 is the wavelength of the laser, N_A is Avogadro's number, and dn/dc is the change in refractive index due to the change in concentration. A value of 0.185 mL/g was used for this determination (43–45).

3.3.3- Analytical Ultracentrifugation

Sedimentation velocity (SV- AUC) experiments were used to determine the sedimentation coefficient of purified $FXR1_{1\text{-}460}$ and to determine the homogeneity of the sample. Protein was concentrated, and an absorbance of 0.6 OD at 280nM (~15 μM) was measured with a

ThermoFisher Genesys 50S bench-top spectrophotometer in a 1 cm pathlength quartz cuvette. To remove any aggregates, the sample was spun in a microcentrifuge at 20,000 x g for 10 minutes, and a final absorbance of 0.55 OD was determined. Analytical Ultracentrifugation (AUC) was performed in a Beckman-Coulter Optima AUC centrifuge at the Canadian Center for Hydrodynamics with an AN50-Ti Rotor at 4 °C. 460 µL of clarified sample was loaded into an epon-2 channel centrepiece with quartz windows and measured at 35,000 revolutions per minute (rpm) at 280 nm. Using the UltraScan-III package, the sedimentation velocity data were analyzed (46). The van Holde-Weischet analysis provided the sedimentation distribution (47, 48). All hydrodynamic calculations were corrected to standard conditions at 20 ºC and water. Estimated hydrodynamic properties were calculated using HullRad (49).

3.3.4- *In vitro* production and purification of ZIKV terminal regions

Terminal region constructs were designed based on the sequence of the ZIKV Haiti/1225/2014 genome (genebank ID: KU509998.3). These terminal regions were designed to be the full-length terminal regions of 113 nts and 432 nts for the 5′ and 3′ terminal regions and were placed into pUC-GW-Kan constructs designed by Genewiz®, with the addition of an XbaI restriction cut site at the end of the transcript sequence. The sequences of the TRs are as follows:

ZIKV 5′ TR (113 nts)

5′GGGGUUGUUACUGUUGCUGACUCAGACUGCGACAGUUCGAGUUUGAAGC
GAAAGCUAGCAACAGUAUCAACAGGUUUUAUUUGGAUUUGGAAACGAGAG
UUUCUGGUCAGAUC 3′

ZIKV 3′ TR (432 nts)

5′UAAGCACCAAUCUUAAUGUUGUCAGGCCUGCUAGUCAGCCACAGCUUGG
GGAAAGCUGUGCAGCCUGUGACCCCCCCAGGAGAAGCUGGGAAACCAAGCC
UAUAGUCAGGCCGAGAACGCCAUGGCACGGAAGAAGCCAUGCUGCCUGUG
AGCCCCUCAGAGGACACUGAGUCAAAAAACCCCACGCGCUUGGAGGCGCAG
GAUGGGAAAAGAAGGUGGCGACCUUCCCCACCCUUCAAUCUGGGGCCUGA
ACUGGAGAUCAGCUGUGGAUCUCCAGAAGAGGGACUAGUGGUUAGAGGAG

ACCCCCCGGAAAACGCAAAACAGCAUAUUGACGCUGGGAAAGACCAGAGA
CUCCAUGAGUUUCCACCACGCUGGCCGCCAGGCACAGAUCGCCGAAUAGCG
GCGGCCGGUGUGGGGAAAUCCAUGGGUCUU 3′

These plasmids were then transformed into NEB5α E. coli cells, provided by New England Biolabs®. The expression plasmids were purified using a ThermoScientific™ GeneJET Plasmid Maxiprep kit, then digested with XbaI for 4 hours at 37 °C to linearize the plasmid. This linearized plasmid was used for *in vitro* transcription (IVT), incubated at 37 °C for 4 hours, and treated with DNase for 1 hour at 37 °C. After this incubation, RNA was purified via size exclusion chromatography (SEC) on a Superdex 200 Increase GL 10/300 (S200) (Global Life Science Solutions USA LLC, Marlborough, MA, USA) in Bis-Tris RNA Buffer (10 mM Bis-tris pH 5.5, 100 mM NaCl, 15 mM KCl, 5 mM MgCl2, 5% glycerol) using an ÄKTA pure FPLC system (Global Life Science Solutions USA LLC, Marlborough, MA, USA). Fractions containing RNA, as determined from the chromatogram, were run on a 2% agarose gel for 30 minutes at 100V and stained with Sybersafe™ to confirm homogeneity. The pure fractions were collected, vitrified in liquid nitrogen, and stored at -80 °C until downstream use.

3.3.5- Fluorescent labelling of ZIKV terminal regions and poly(U)

Fluorescent labelling was performed through reactive 5′ phosphate labelling using Alexa 488 fluorophore method previously mentioned in (20, 51). Poly(uridine) (poly(U)) was diluted from a powder stock (Sigma Aldrich) to a concentration of 1 mM; the RNAs were all resuspended in 7.5 µL of Bis-Tris RNA buffer, concentrating to roughly > 100 µM via ethanol precipitation. Following this, 20µL of 0.1 M imidazole (pH 6), 1.25 mg of 1-ethyl-3-(3-dimethylamino) propyl carbodiimide hydrochloride, and 10µL of Alexa 488 hydrazide were added to the resuspended RNA and incubated at room temperature for 4 hours. The TR RNA was then purified using SEC

on an S200 column, while the poly(U) was purified using an RNA cleanup kit (New England Biolabs, Canada). Labelled species were purified from unused fluorophore and degraded RNA, and pure, labelled RNA was stored at -80 °C until experimentation. The RNA labelling was tested using the Nanotemper Technologies Monolith NT.115 (Nanotemper Technologies, Munich, Germany), with auto-excitation power, to ensure that sufficient fluorescence was observed at the RNA concentrations used for microscale thermophoresis assays.

3.3.6- Electrophoretic Mobility Shift Assay (EMSA)

FXR1 $_{1\text{-}380}$ was taken at a concentration of 15μM and serially diluted twofold until a final concentration of 117nM. ZIKV 5′ or 3′ TR was then titrated in at a constant concentration of 250 nM. The interaction was incubated for 1 hour at 37 °C and then run on a 6% Tris-Native PAGE at 150V for 1 hour. The gel was stained with Sybrsafe^{TM} and imaged using an Amersham Typhoon.

3.3.7- Microscale Thermophoresis (MST)

A 2-fold serial dilution of FXR1$_{1\text{-}460,\ 1\text{-}380}$ was performed using FXR1 SEC buffer, starting at 10μM until the final concentration was 0.152 nM. A constant amount of the various fluorescent 5′ TR or 3′ TR RNA, at a concentration of 400 nM and 200 nM, respectively, was added to each serial dilution of the FXR1. Poly(U) was used at a constant concentration of 3.5 μM as a negative control. To the poly(U), 500 mM NaCl was added, along with additional FXR1$_{1\text{-}460}$, and the previously mentioned serial dilution was performed. The reaction was then incubated for 1 hour at 37 °C and subsequently placed into standard capillaries, which were then loaded into a Nanotemper Technologies Monolith NT.115 instrument (Nanotemper Technologies, Munich, Germany) for microscale thermophoresis measurements. Thermophoresis was performed using an 80% excitation power and heated with a medium MST IR laser power. Fluorescent migration used

to determine the dissociation constant (K_d) was measured from 4 to 5 seconds, which was normalized to the initial fluorescence. Assay was performed in triplicate (52, 53).

3.4- Results

3.4.1- FXR1 Purification

Initial purification of full-length FXR1 via nickel affinity chromatography is shown in **Figure 3.1A**. The SDS-PAGE analysis of early elution fractions (25 mL) revealed a band near the 66 kDa mark, aligning with the theoretical weight of 69.7 kDa for full-length FXR1 in **Figure 3.1 B**. Subsequent purification using anion exchange chromatography was attempted to remove any nucleic acid contamination. This purification is illustrated in **Figure 3.1 C**, where a large peak absorbing at 280 nm elutes from 5-10 mL, while significant absorption at 260 nm is observed from 30-40 mL. However, SDS-PAGE of these fractions, as seen in **Figure 3.1D**, displayed an absence of banding at the correct molecular weight.

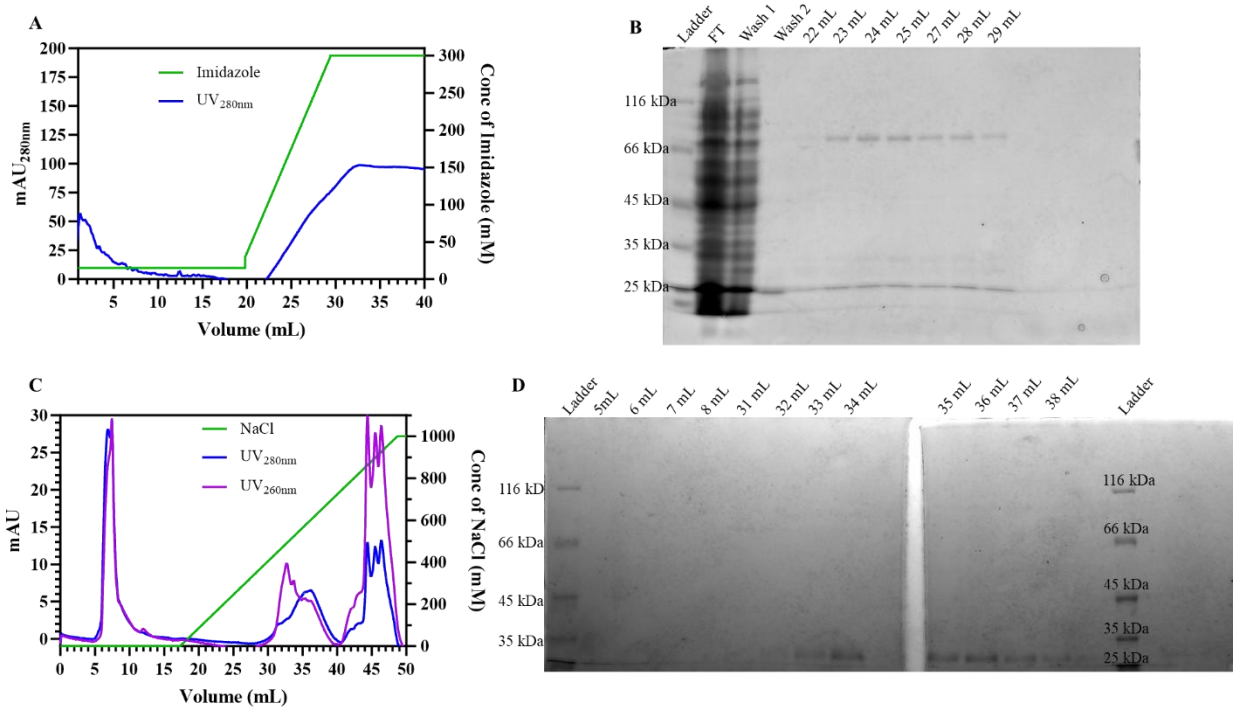

Figure 3.1: Purification of full-length FXR1. (A) Chromatogram of affinity purification (His-Trap FP) with a peak in absorbance of 280 nm beginning at 22 mL. **(B)** Represents the SDS-PAGE analysis of fractions 22-29 mL, corresponding with the elution profile. A band above 66 kDa can be observed, corresponding to the molecular weight of full-length FXR1 (69.7 kDa). Fractions from 23-29 mL were collected, and subsequent anion exchange (MonoQ) was performed in **(C)**. The SDS-PAGE analysis of the anion exchange purification in **(D)** displays no bands at the correct molecular weight, indicating loss of protein.

Due to the low affinity chromatography yields and the presence of bands at the correct molecular weight in the flow-through and wash, the initial full-length FXR1 construct was analyzed and redesigned. This redesigned construct is illustrated in **Figure 3.2B**, where the disordered C-terminal tail was truncated, retaining the RGG RNA-binding box for recognition, and the hexa-histidine tag was relocated to the N-terminus, resulting in a sequence of amino acids 1-460. Expression screening seen in **Figure 3.3** identified optimal expression conditions of 37 °C to 18 °C after induction using Lemo21 cells.

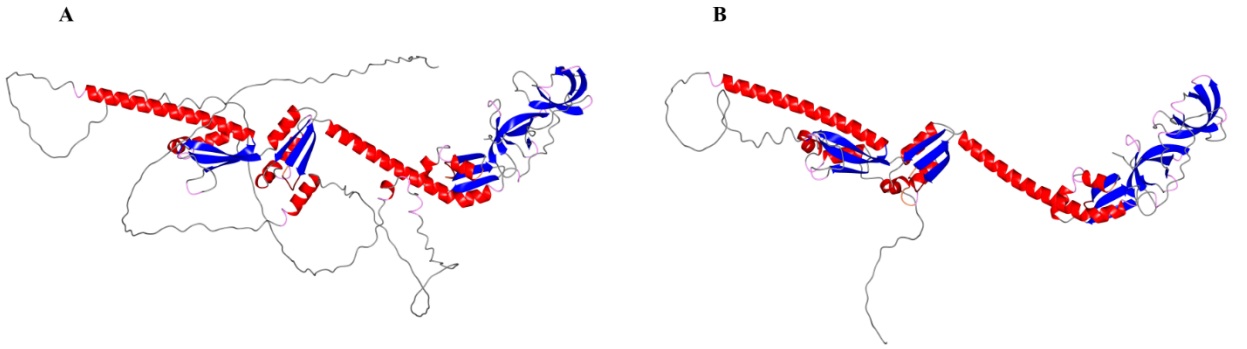

Figure 3.2: Predicted Models of full-length and redesigned FXR1. (A) A representation of the full-length FXR1 structure with amino acids 1-621. While the redesigned FXR1 is depicted in **(B)** with amino acids 1-460. A shorter, intrinsically disordered tail is observed in the redesigned construct. Models were generated using AlphaFold V2, and colours are representative of secondary structures with α-helices in red and β-sheets in blue.

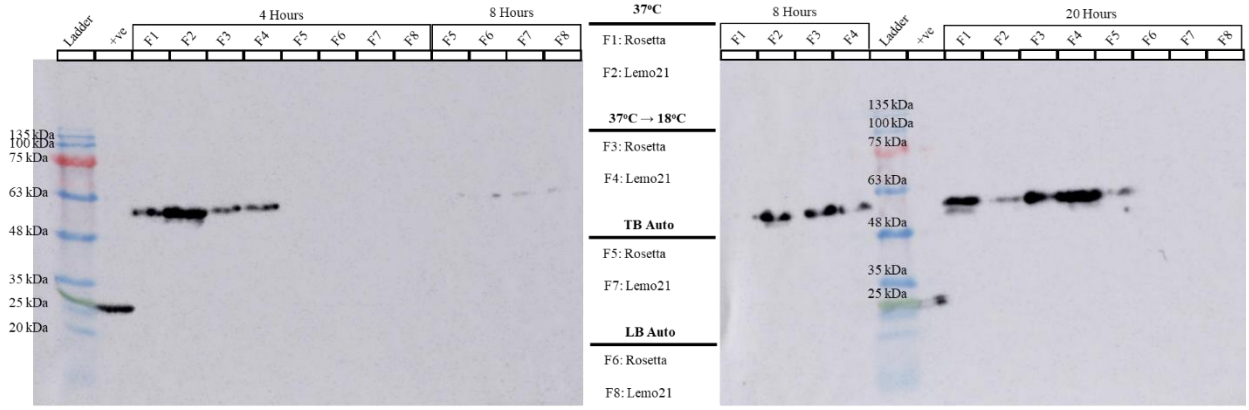

Figure 3.3: Expression Screening of FXR1$_{1\text{-}460}$. Following induction of protein expression at an OD of 0.6 using 1 mM IPTG, time points were taken at 4, 8, and 20 hours post-induction. Cells were pelleted at 10,000 xg for 10 minutes and subsequently lysed. The lysis was then run on an SDS-PAGE gel and transferred, and blotting was performed using a mouse anti-histidine antibody and a goat anti-mouse antibody. Conditions for 37 ^{o}C and 18 ^{o}C after induction have the most banding indicating effective expression.

During the purification of $FXR1_{1-460,}$ denaturing purification was employed, as protein was detected in the insoluble fraction, as shown in **Figure 3.4A**, yielding a 52 kDa band that matched the truncated construct. After purification by SEC, the elution profile is shown in **Figure 3.4B**, and the corresponding SDS-PAGE is presented in **Figure 3.4C**. The elution profile exhibited a varying number of peaks, and upon analysis on the gel, a band predominantly at 43 kDa was observed, while the band at 52 kDa was faint in comparison. To verify that this was still FXR1, the 43 kDa band was isolated and sent for mass spectroscopy. From this analysis, it was confirmed that the predominant species in that band was indeed FXR1. To avoid the need for denaturing

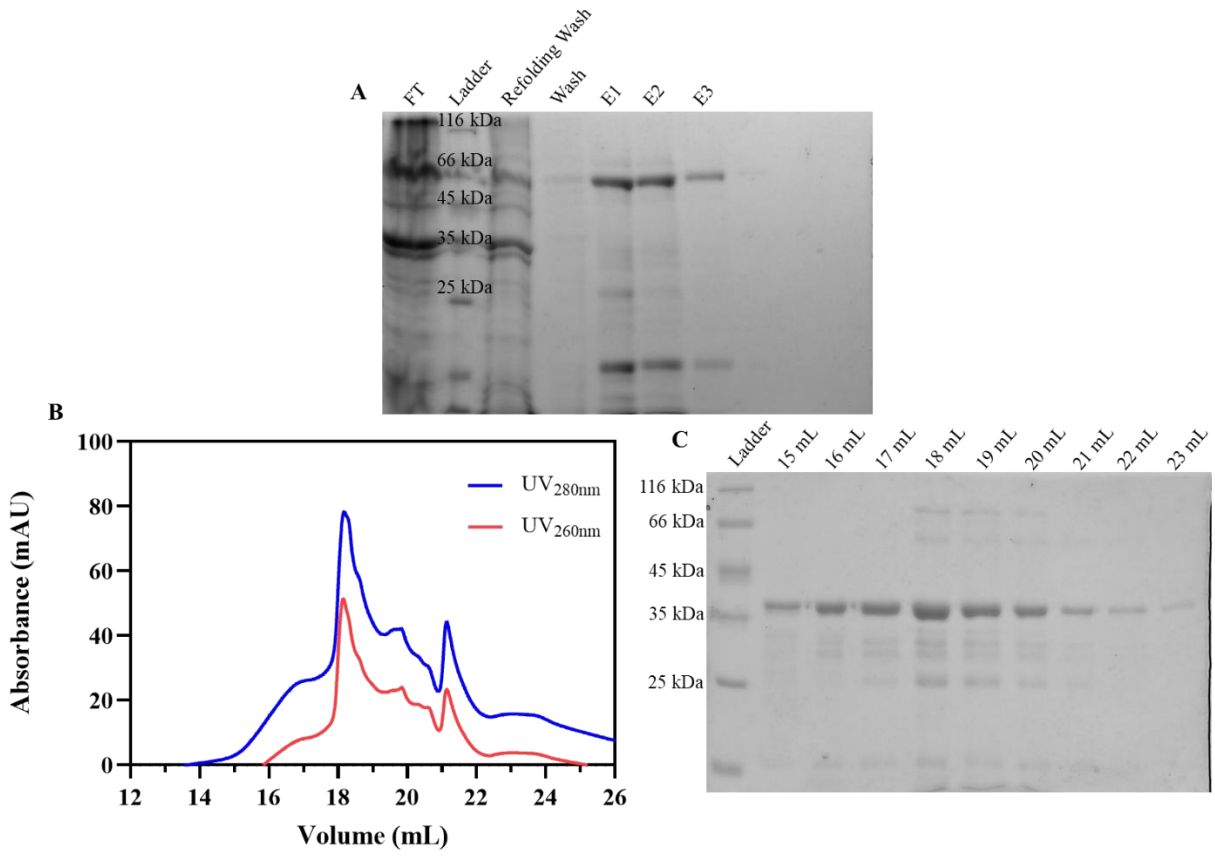

Figure 3.4: Denaturing Purification of $FXR1_{1-460}$. (A) The SDS-PAGE was performed following purification through affinity chromatography (His-Trap FP) of $FXR1_{1-460}$ under denaturing conditions. A distinctive band at ~52 kDa can be seen corresponding with the molecular weight of $FXR1_{1-460}$. Fraction E1-3 were collected and further purified using size exclusion (Superdex 200 increase gl 10/300) **(B)**. Peak fractions from 15- 23 mL were run on an SDS-PAGE, represented by **(C)**, depicting a prominent band above the 35 kDa mark. This corresponds to the further truncated form of FXR1, comprising amino acids 1-380, with a molecular weight of 43 kDa.

purifications, the concentration of IPTG was lowered during $FXR1_{1-460}$ expression, resulting in less total protein but preventing the sequestering of the protein in inclusion bodies. The affinity purification of this protein can be seen in **Figure 3.5A**, with bands present at the correct molecular weight in **Figure 3.5 B**. Following this, anion chromatography to remove nucleic acids was performed as seen in **Figure 3.5 C**, and the final samples from the elution peak from 5-10 mL were visualized on an SDS-PAGE in **Figure 3.5 D**. The bands present in samples 6-9 mL, matching the 52 kDa molecular weight, were selected and kept for further assays.

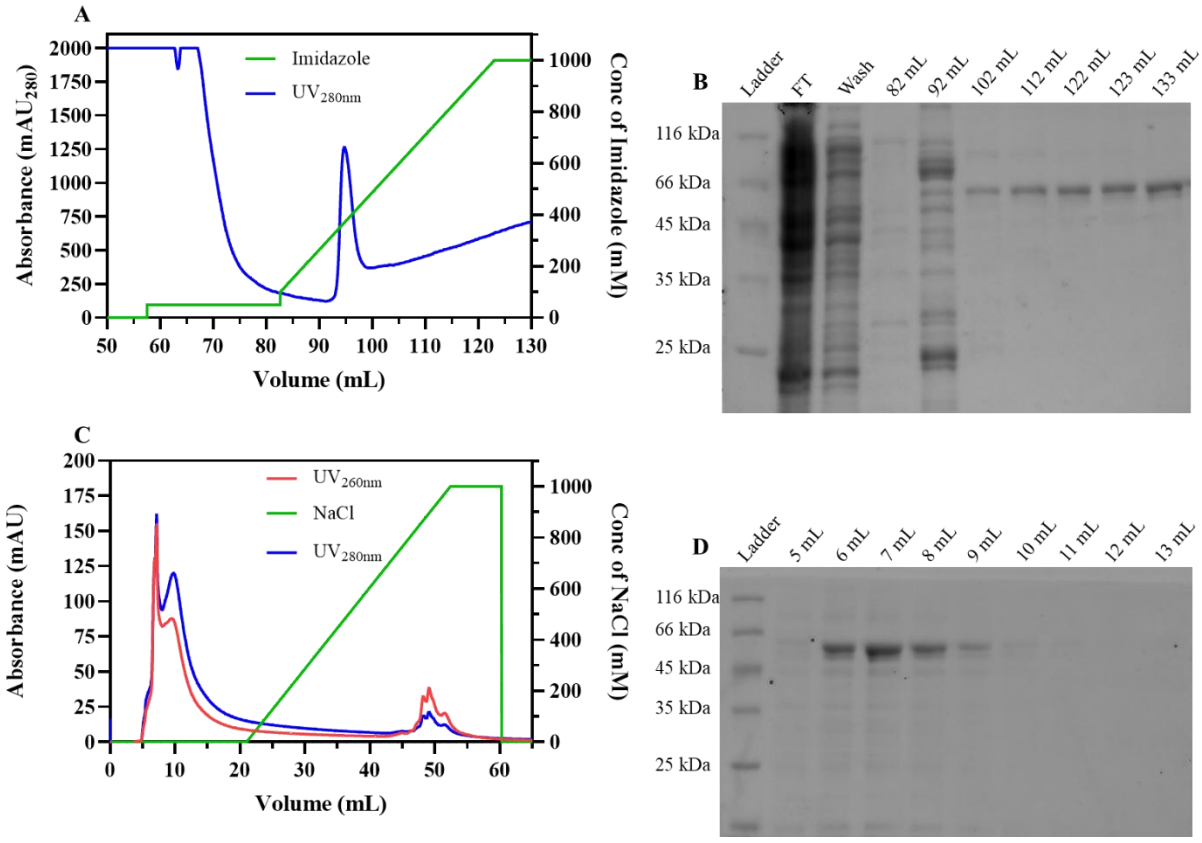

Figure 3.5: Optimized Purification of $FXR1_{1-460}$. (A) The elution profile after affinity purification (His-Trap FP) of $FXR1_{1-460}$, following soluble purification, shows an increase in absorbance during the elution from fractions 90- 130 mL. **(B)** Represents the SDS-PAGE analysis of the fractions with a clear band at 52 kDa. Fractions from 102-133 mL were collected, and subsequent anion exchange chromatography was performed with the elution profile seen in **(C)**. The prominent peak observed from 5- 10 mL was run on an SDS-PAGE, as seen in **(D),** with bands still present at the correct molecular weight of ~52 kDa, with fractions 6- 8 mL being kept for future assays

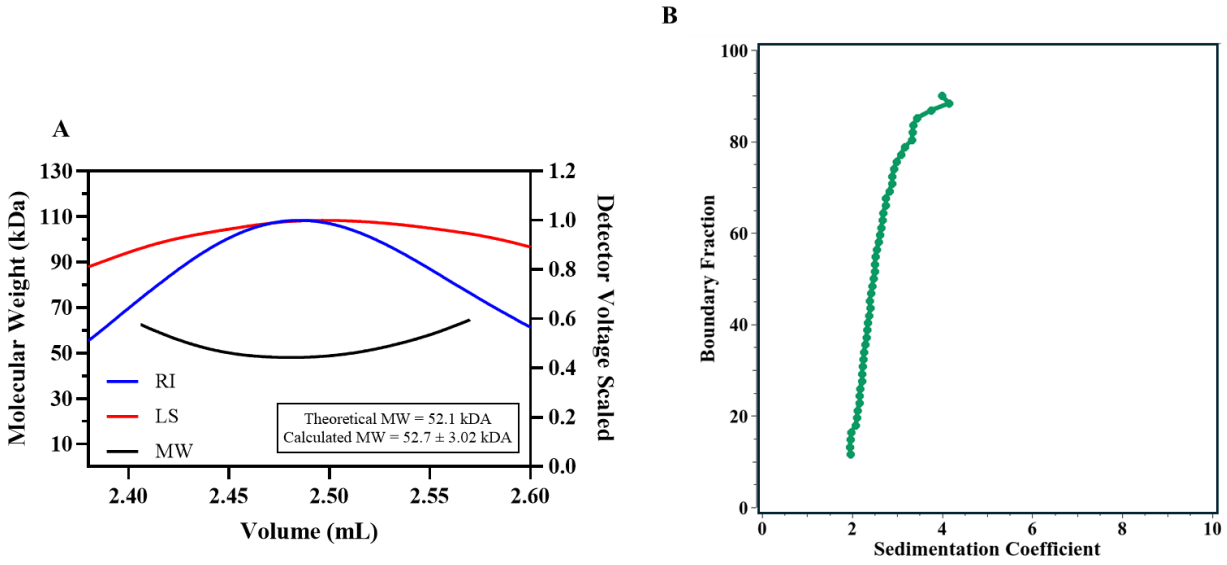

Figure 3.6: Biophysical characterization of purified FXR1$_{1\text{-}460}$. The purity of the collected FXR1$_{1\text{-}460}$ was verified using size exclusion multi-angle light scattering and analytical ultracentrifugation. The absolute molecular weight determination was calculated with the traces seen in **(A)**. The calculated molecular weight corresponds to that of the theoretical molecular weight, indicating a purified FXR1$_{1\text{-}460}$. Following sedimentation velocity experiments, the sedimentation coefficients of the sample were determined, and the distribution was plotted through a van Holde-Weichet plot, as seen in **(B)**. This distribution shows a sedimentation coefficient ranging from 2 to 3 S, accounting for 10-80% of the species present, which coincides with the estimated sedimentation coefficient of 2.5 S. The sedimentation coefficients were corrected for standard buffer conditions (20 °C in water).

This was then further tested through SEC-MALS to determine the homogeneity and monodispersity of FXR1$_{1\text{-}460}$. The calculated molecular weight determined through light scattering can be seen in **Figure 3.6 A**. By applying high centrifugal force through AUC and monitoring the sedimentation of FXR1$_{1\text{-}460}$, the sedimentation coefficient and the distribution of observed sedimentation coefficient can be seen in **Figure 3.6 B**. This distribution indicates a relative sedimentation coefficient of 2-3 S, which coincides with the estimated coefficient of 2.5 S.

3.4.2- Purification of ZIKV terminal regions

After purifying the IVTS using SEC, the elution's are visible in **Figure 3.7A**, with the traces of the emotions represented in blue and red for the 5′ TR and 3′ TR, respectively. The 5′ TR

eluted at around 12-13 mL, while the 3′ TR was seen to elute earlier, at a volume of 9-10 mL. These fractions were then visualized using the agarose gel, as shown in **Figure 3.7 B** and **C** for the 5′ TR and 3′ TR, respectively. The singular bands present within these fractions corresponding to the correct base pairing size were selected for further labelling and binding assays. The RNA that was concentrated and used for the labelling reaction was purified through SEC, which is observed in **Figure 3.8 A**, with the elution profile of both the 5′ TR and 3′ TR eluting at the same volumes as previously purified. These samples were then checked on an agarose gel to verify that the correct length of the species was still present and the RNA wasn't degraded due to the labelling reaction. Bands corresponding to the same length as previously observed on the agarose gel are visible in **Figure 3.8B**, indicating intact RNA transcripts after the labelling interaction.

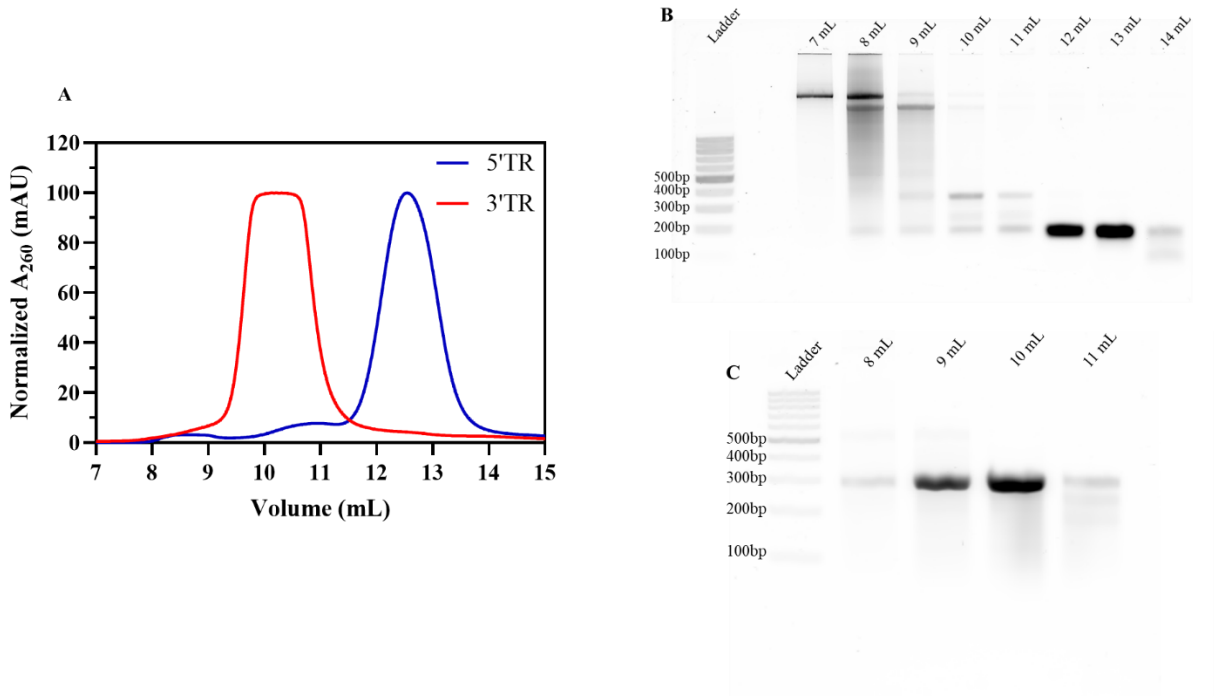

Figure 3.7: Purification of ZIKV UTR. Following *in vitro* transcription, RNA was purified through the use of size exclusion chromatography (Superdex 200), and the elution profiles can be observed in **(A)** with the 5′ TR (blue) eluting around 12-14 mL and the 3′ TR (red) eluting from 9- 11 mL. Fractions from these elution profiles were run on a 2% agarose to visualize RNA purity, with the fractions from the 5′ TR seen in **(B)** and the 3′ TR in **(C)**. Fractions of 12-13 mL were selected for the 5′ TR, as a homogeneous band around the 200 bp mark can be seen. Fractions 9-10 mL for the 3′ TR were selected for a single band around the 300 bp ladder. The migration of the RNA differs compared to the expected sizes of 113 nts and 432 nts for the 5′ and 3′ TR, respectively, due to the use of a DNA 100-1000 base pair ladder (BioBasic).

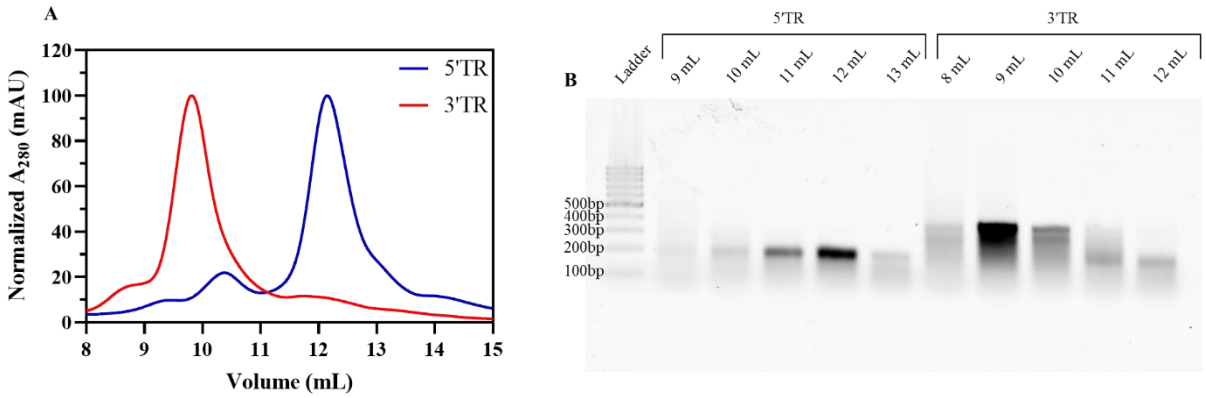

Figure 3.8: Fluorescent Labelling of TRs. After the purification of the RNA, the collected fractions were concentrated and used for labelling reactions. The purification of labelled RNA using size exclusion chromatography (Superdex 200) can be observed in **(A)**. The elution volumes of the 5′ TR (blue) and the 3′ TR (red) coincide with the previous purification. Fractions ranging from 9- 13 mL for the 5′ TR and 8- 12 mL for the 3′ TR were run on a 2% agarose gel, as seen in **(B)**. Homogeneous bands matching those of the previously determined size can be seen in fractions 11-12 mL for the 5′ TR and 9-10 mL for the 3′ TR; these fractions were retained for further assays.

3.4.3- Interaction of FXR1 and ZIKV terminal regions

Initial interactions with the truncated $FXR1_{1-380}$ were performed with the 5′ and 3′ TRs, with the electrophoretic mobility shift assay seen in **Figure 3.9 A** and **C**. A shift at high concentrations of $FXR1_{1-380}$ was observed with the 5′ TR, while no apparent shift was seen for the 3′ TR. This initial binding study was then replicated using microscale thermophoresis to determine the binding affinity and a K_d for the interactions. In **Figure 3.9 B** and **D**, it can be seen that the $FXR1_{1-380}$ binds to the 5′ TR with a K_d of 109 nM, while the binding to the 3′ TR has a K_d of 5.5 µM, respectively. After purification of the optimized $FXR1_{1-460}$ expression, an MST assay was performed again to determine the binding affinities for $FXR1_{1-460}$ to the TRs seen in **Figure 3.10 A** and **B**. The binding affinities for both TRs with $FXR1_{1-460}$ are seen to be closer than the previous MSTs, with a K_d of 2.8 µM and 4.9 µM for the 5′ and 3′ TRs, respectively. Using a poly(U) polynucleotide as a control, it is evident from Figure 3.10C that $FXR1_{1-460}$ also exhibits binding to

poly(U) with a Kd of 0.63 µM. However, the addition of 500 mM NaCl to the interaction results in no binding, as shown in **Figure 3.10D**.

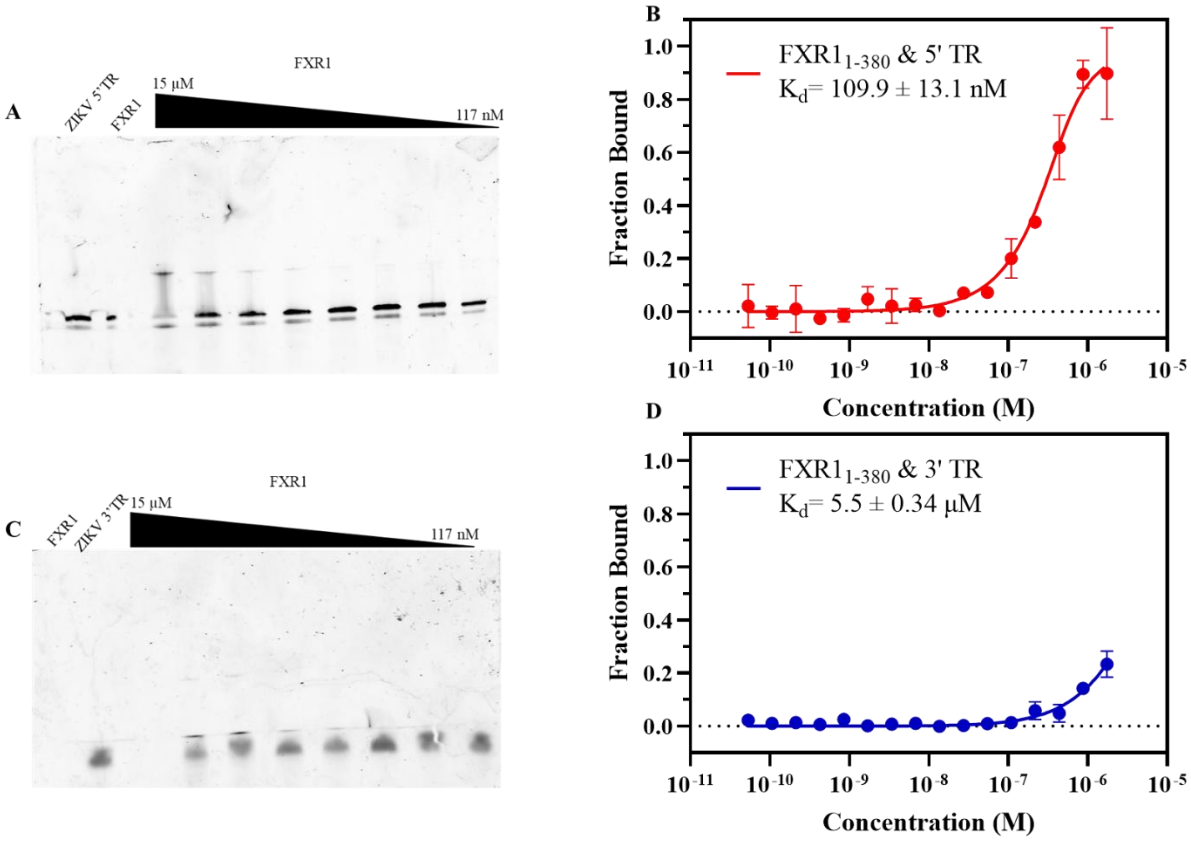

Figure 3.9: Interaction of FXR1$_{1-380}$ and ZIKV TRs. Using the purified FXR1$_{1-380}$ initial interaction studies were performed with the TRs of ZIKV. Electrophoretic mobility shift assays were performed using a 2-fold serial dilution of FXR1$_{1-380}$ from 15 µM to 117nm. The RNA was added at a constant concentration of 250 nM with the 5′ TR seen in **(A)** and the 3′ TR seen in **(C)**. A shift of the banding to a higher migration for the 5′ TR interaction is observed while no shift for the 3′ TR is seen. Microscale thermophoresis measurements were then performed for the 5′ TR **(B)** and the 3′ TR **(D)** interaction with FXR1$_{1-380}$. Protein was serially diluted from a starting concentration of 10 µM to 0.152 nM and constant amounts of fluorescently labelled RNA was added at concentrations of 400 nM and 200 nM for the 5′ and 3′ TRs respectively. Through MST measurements a dissociation constant was determined for the interactions with the TRs with a K_d of 109 nM for the 5′ TR with FXR1$_{1-380}$ (red) and a K_d of 5.5 µM for the 3′ TR and FXR1$_{1-380}$ (blue).

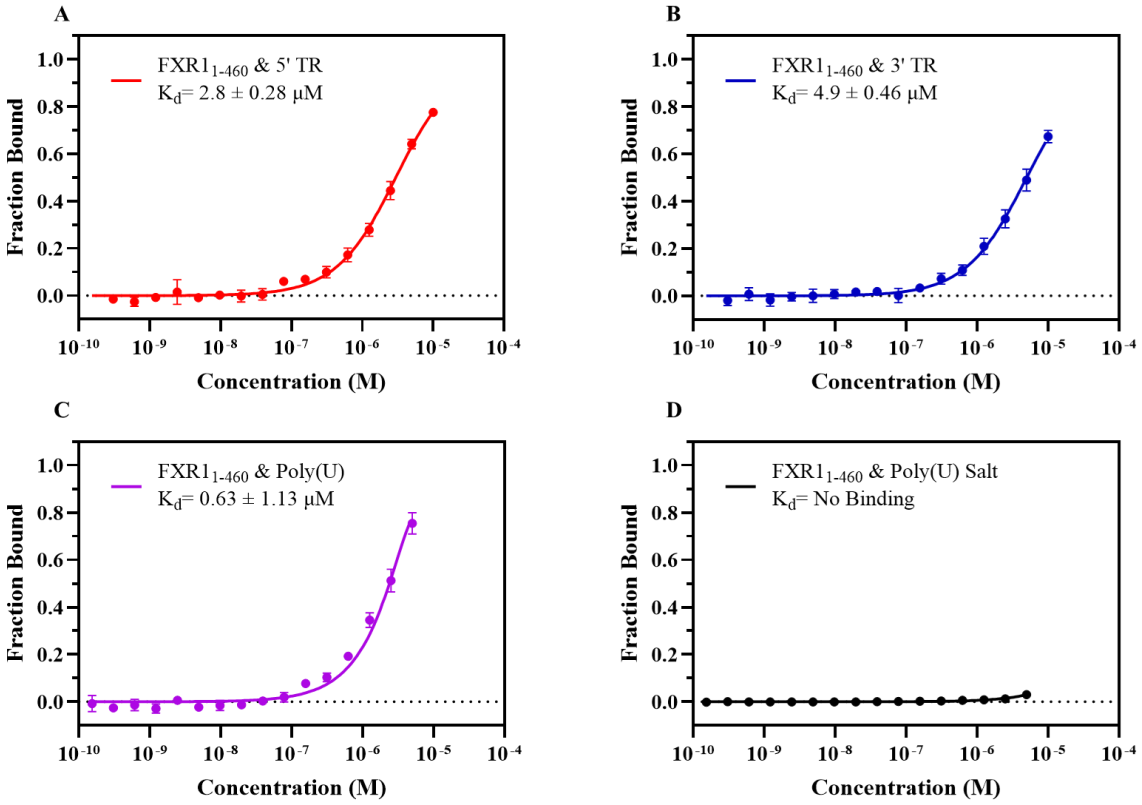

Figure 3.10: Interaction of FXR1$_{1-460}$ with TRs and poly(U). Using the optimized and purified FXR11-460, Microscale thermophoresis measurements were performed for the 5′ TR **(A)**, 3′ TR **(B)**, poly(U) **(C)**, and the poly(U) with 500 mM NaCl **(D)**. Protein was serially diluted from a starting concentration of 10 µM to 0.152 nM, with constant amounts of fluorescently labelled RNA added at 400 nM and 200 nM for the 5′ and 3′ TRs, respectively, while poly(U) was used at 3.5 µM. MST measurements determined dissociation constants (Kd) for the interactions: 2.8 µM for the 5′ TR (red), 4.9 µM for the 3′ TR (blue), and 0.63 µM for poly(U) (purple). The addition of 500 mM NaCl inhibited the binding between poly(U) and FXR11-460, showing no interaction (black).

3.5- Discussion

Initial purification attempts of full-length FXR1 yielded low protein recovery, with significant loss after MonoQ and no bands at the expected weight on SDS-PAGE **(Figure 3. 1D)**. Due to the challenges of initial purifications, the original construct was redesigned. A large portion of the intrinsically disordered region at the C-terminal was removed to reduce the potential formation of liquid-liquid phase separation condensates. Additionally, the hexa-histidine tag was relocated from the unstructured C-terminal, where it was likely lost due to tail fragmentation, to the structured N-terminal. This truncated construct is shown in **Figure 3.2B**, which reduced the overall disordered region, while the structure of the protein predicted by AlphaFold shows a very linear shape with long α-helices, likely contributing significantly to the hydrophobic interactions observed in FXR1 (33, 54). Despite these modifications to $FXR1_{1-460,}$ initial attempts resulted in the protein sequestering into inclusion bodies (55). This prompted the use of denaturing purification, which yielded bands at the correct molecular weight **(Figure 3. 4A)**. Further purification by size exclusion unexpectedly produced an even more truncated version, $FXR1_{1-380}$ **(**~43 kDa; **Figure 3. 4C)**, confirmed as FXR1 via mass spectrometry. This truncation is likely due to the loss of the disordered C-terminal tail, leaving amino acids 1-380. Unfortunately, this result was not reproducible, and denatured samples showed aggregation during concentration, probably due to refolding issues. This led to reducing the IPTG concentration to 0.1 mM, which lowered expression levels but caused less stress on the bacterial cells, allowing for FXR1 retrieval from the soluble fraction (55). This strategy proved optimal, eliminating the need for denaturation and refolding, thus preventing aggregation. The improved purification is shown in **Figure 3.5D**, where bands are visible at the correct molecular weight. This is further supported by SEC-MALS analysis of $FXR1_{1-460}$ **(Figure 3.6A)**, where the measured molecular weight via light scattering matches the

theoretical value. Additionally, SV-AUC experiments revealed a sedimentation coefficient of approximately 2-3 S, which aligns well with the calculated coefficient of 2.5 S based on an AlphaFold model of FXR $_{1-460}$ and HullRad, indicating the sample is relatively homogeneous with minor variations in sedimenting species.

During the purification process, FXR1$_{1-460}$ could not be further purified using size exclusion chromatography; the only instance of successful purification was achieved following cleavage of the remaining intrinsically disordered region, resulting in FXR1$_{1-380}$. The concentrating of FXR1$_{1-460}$ also caused challenges, as aggregation above 15 μM was prominent; this was theorized to be due to the formation of condensates, as the ability of FXR1 to form LLPS condensates was previously shown due to electrostatic and hydrophobic interactions (32, 35, 56). Previous research has also demonstrated aggregation due to the concentration of FXR1 using centrifugal force, as well as through storage (57). Further buffer optimization to limit the formation of these condensates included increasing the salt concentration from 100 mM to 250 mM, as well as the addition of the surfactant CHAPS at 0.3%. This modification was designed to inhibit excessive electrostatic and hydrophobic interactions, thereby preventing protein aggregation and the formation of condensates. Even with these modifications to the buffer, the storage and concentration of FXR1$_{1-460}$ were prone to aggregation. When comparing the UV absorbance before the AUC experimentation, an OD of 0.55 at 280 nm was observed. However, during the AUC experiment, the total absorbance decreased to 0.4 OD, indicating a loss of sample during the experimentation. This could be attributed to the time period before the first scan was collected, which had a sufficient delay at high rpm, leading to aggregation and subsequent sedimentation, resulting in a smaller sample concentration to be observed. While removing more of the

intrinsically disordered region would cause the loss of RGG RNA recognition (58), removing this region would reduce the complications due to LLPS and aggregation formation.

Initial interactions using EMSAs with the further truncated $FXR1_{1-380}$ indicated binding between the 5′ TR, as seen by the shift in the banding pattern in **Figure 3.9A**. In contrast, the 3′ TR in **Figure 3.9C** didn't show any shift in the band migration, indicating no interaction was occurring. This was then further verified through the use of microscale thermophoresis, where a K_d of 109 nM for the interaction with the 5′ TR was determined, while a K_d of 5.5 μM was determined for the 3′ TR **(Figure 3.9B** and **D)**. This observation aligns well with the EMSA results, where $FXR1_{1-380}$ bound preferentially to the 5′ TR. Purified $FXR1_{1-460}$ binding studies with the TRs were performed again to see if the additional RGG RNA box within the intrinsically disordered tail enabled a greater specificity for FXR1s binding. Through this further assay, it can be seen that by maintaining a larger portion of the intrinsically disordered region altered the binding affinities for both TRs, decreasing $FXR1_{1-460}$ affinity for the 5′ TR **(Figure 3.10A)** (109 nM to 2.8 μM) while increasing the affinity for the 3′ TR **(Figure 3.10B)** (5.5 μM to 4.9 μM) when compared to $FXR1_{1-380}$. Previous research has demonstrated that the RGG box, located within the intrinsically disordered region, induces specificity for RNA tertiary structures such as G-quadruplexes and kissing complexes, as well as interactions with poly(U) (58–63). This could account for the slight increase in affinity exhibited for the 3′ TR, as it has been identified to contain a G-quadruplex (20). Previous literature has also indicated that FXR1 interacts with the 3′ TR of ZIKV *in vivo,* consistent with what we have observed (41). In order to determine if $FXR1_{1-460}$ interacts with the TRs of ZIKV specifically, a poly(U) polynucleotide was used as a positive control. $FXR1_{1-460}$ displayed a high affinity for the poly(U) with a K_d of 0.63 μM **(Figure 3.10C)**, indicating a stronger affinity for the poly(U) in comparison to either TR or ZIKV.

The KH domains of $FXR1_{1-460}$ have been found to bind to the AU-rich elements of the 3′ TR of mRNA, and they have also exhibited binding to various poly(cytosine)s (59, 64). While other RNA recognition motifs can recognize varying lengths of RNA, the KH domains' binding cleft is designed to accommodate four nucleotides, indicating a higher selectivity (64). Although a large portion of the binding interaction between the KH domains is due to hydrophobic interactions with aromatics within the cleft, electrostatic forces play a role in the initial entry (64). Utilizing this requirement for electrostatic forces in the interaction initiation, a further assay with poly(U) was performed, increasing the NaCl concentration to 500 mM to inhibit any electrostatic charge attractions between the $FXR1_{1-460}$ KH domains and poly(U). This shielding of charge interactions then displayed no binding between $FXR1_{1-460}$ and poly(U) **(Figure 3.10D)**, thus indicating that the interactions observed between $FXR1_{1-460}$ and the TRs of ZIKV, as well as the poly(U), were due to binding interactions and not attributed to impeding of the fluorophore due to factors such as aggregates.

3.6- Conclusion and Future Directions

Through this study, we have developed a method for recombinantly expressing and purifying the fragile-X related protein 1 and examined its interactions with the terminal regions of Zika viruses. Although the interaction with the TRs appears to be less specific due to binding with poly(U), the interaction of various KH domains with RNA has dissociation constants determined to be approximately the same, with a K_d of 3 μM (64). Techniques such as surface plasmon resonance could be used to further characterise the interaction between the TRs and FXR1, as the protein can be fixed at relatively low concentrations, reducing aggregation issues (65, 66). While FXR1 can be purified, significant challenges remain. Aggregation during concentration and storage may complicate its use in various assays, often requiring repeated purifications. Removing the intrinsically disordered tail (FXR1 $_{1\text{-}380}$) might reduce aggregation by inhibiting LLPS driven by the disordered region. This could improve purification efficiency and protein stability, enabling concentration. However, this approach would likely decrease the specificity of the protein's binding to different RNA tertiary structures. Removing the tail would reduce FXR1's ability to distinguish between distinct RNAs, potentially limiting its biological relevance in assays that depend on precise molecular interactions.

While the results indicated reduced specificity for a particular terminal region, further investigation into the potential role FXR1 plays during viral infection is warranted. Employing knockdowns of FXR1 during viral replication would be valuable to clarify FXR1's specific contribution to this process. Given that ZIKV produces ROs along the ER (17) and considering FXR1's established role in facilitating RO formation in coronaviruses (35), FXR1 may contribute to the correct assembly of ZIKV's ROs. Furthermore, FXR1 has also been shown to facilitate viral replication in coronaviruses through interaction with its non-structural protein 3 (67). Investigating

this dual role in RO formation and direct viral protein interaction within the context of ZIKV is therefore essential. One potential mechanism is that, during ZIKV replication, FXR1 interacts with viral proteins, increasing its affinity for the TRs and promoting binding (68). Overall, this study provides initial insight into the potential interaction between FXR1 and ZIKV TRs and lays the foundation for future research into the importance of FXR1 within the viral life cycle.

3.7- References

1. R. Lowe, *et al.*, The zika virus epidemic in brazil: From discovery to future implications. *Int J Environ Res Public Health* **15** (2018).
2. A. Gulland, Zika virus is a global public health emergency, declares WHO. *BMJ* **352**, i657 (2016).
3. Zika virus disease – India. Available at: https://www.who.int/emergencies/disease-outbreak-news/item/2025-DON549 [Accessed 28 May 2025].
4. P. Brasil, *et al.*, Guillain-Barré syndrome associated with Zika virus infection. *The Lancet* **387**, 1482 (2016).
5. V. M. Cao-Lormeau, *et al.*, Guillain-Barré Syndrome outbreak associated with Zika virus infection in French Polynesia: A case-control study. *The Lancet* **387**, 1531–1539 (2016).
6. E. J. Rubin, M. F. Greene, L. R. Baden, Zika virus and microcephaly. *N. Engl. J. Med.* **374**, 984–985 (2016).
7. N. Zhang, *et al.*, Zika Virus Disrupts Neural Progenitor Development and Leads to Microcephaly in Mice. *Cell Stem Cell* **19**, 120–126 (2016).
8. I. Gladwyn-Ng, *et al.*, Stress-induced unfolded protein response contributes to Zika virus-associated microcephaly. *Nat Neurosci* **21**, 63–73 (2018).
9. P. Devhare, K. Meyer, R. Steele, R. B. Ray, R. Ray, Zika virus infection dysregulates human neural stem cell growth and inhibits differentiation into neuroprogenitor cells. *Cell Death & Disease 2017 8:10* **8**, e3106–e3106 (2017).
10. B. H. Song, *et al.*, Comparison of Three Chimeric Zika Vaccine Prototypes Developed on the Genetic Background of the Clinically Proven Live-Attenuated Japanese Encephalitis Vaccine SA14-14-2. *Int J Mol Sci* **26** (2024).
11. M. V. Mancini, *et al.*, Evaluation of an Engineered Zika Virus-Like Particle Vaccine Candidate in a Mosquito-Mouse Transmission Model. *mSphere* **8** (2023).
12. J. V. J. Silva, *et al.*, Current status, challenges and perspectives in the development of vaccines against yellow fever, dengue, Zika and chikungunya viruses. *Acta Trop* **182**, 257–263 (2018).
13. M. A. Garcia-Blanco, S. G. Vasudevan, S. S. Bradrick, C. Nicchitta, Flavivirus RNA transactions from viral entry to genome replication. *Antiviral Res* **134**, 244–249 (2016).
14. S. Denolly, *et al.*, Zika virus remodelled ER membranes contain proviral factors involved in redox and methylation pathways. *Nature Communications 2023 14:1* **14**, 1–20 (2023).
15. K. Van Den Elsen, J. P. Quek, D. Luo, Molecular insights into the flavivirus replication complex. *Viruses* **13** (2021).

16. J. D. Perlmutter, M. F. Hagan, Mechanisms of Virus Assembly. *Annu Rev Phys Chem* **66**, 217 (2014).

17. C. C. García, *et al.*, Cellular Organelles Reorganization During Zika Virus Infection of Human Cells. *Front Microbiol* **11**, 1558 (2020).

18. B. Cerikan, *et al.*, A Non-Replicative Role of the 3′ Terminal Sequence of the Dengue Virus Genome in Membranous Replication Organelle Formation. *Cell Rep* **32**, 107859 (2020).

19. W. C. Ng, R. Soto-Acosta, S. S. Bradrick, M. A. Garcia-Blanco, E. E. Ooi, The 5′ and 3′ Untranslated Regions of the Flaviviral Genome. *Viruses* **9**, 137 (2017).

20. D. L. Gemmill, *et al.*, The 3′ terminal region of Zika virus RNA contains a conserved G-quadruplex and is unfolded by human DDX17. *Biochemistry and Cell Biology* **102**, 96–105 (2024).

21. D. Bhella, Virus Proteins and Nucleoproteins: An Overview. *Subcell Biochem* **88**, 1–18 (2018).

22. Y. Wu, *et al.*, Zika virus evades interferon-mediated antiviral response through the co-operation of multiple nonstructural proteins in vitro. *Cell Discov* **3**, 1–14 (2017).

23. S. Sun, V. B. Rao, M. G. Rossmann, Genome packaging in viruses. *Curr Opin Struct Biol* **20**, 114–120 (2010).

24. L. Ye, *et al.*, RNA Structures and Their Role in Selective Genome Packaging. *Viruses* **13**, 1788 (2021).

25. B. S. Hollidge, S. R. Weiss, S. S. Soldan, The Role of Interferon Antagonist, Non-Structural Proteins in the Pathogenesis and Emergence of Arboviruses. *Viruses* **3**, 629 (2011).

26. A. Deb, *et al.*, Japanese encephalitis virus NS5 protein interacts with nucleolin to enhance the virus replication. *J Virol* **98** (2024).

27. P. S. Shah, *et al.*, Comparative Flavivirus-Host Protein Interaction Mapping Reveals Mechanisms of Dengue and Zika Virus Pathogenesis. *Cell* **175**, 1931-1945.e18 (2018).

28. P. S. Shah, *et al.*, Systems Biology of Virus-Host Protein Interactions: From Hypothesis Generation to Mechanisms of Replication and Pathogenesis. *Annu Rev Virol* **9**, 397 (2022).

29. A. T. Fishburn, O. H. Pham, M. W. Kenaston, N. S. Beesabathuni, P. S. Shah, Let's Get Physical: Flavivirus-Host Protein–Protein Interactions in Replication and Pathogenesis. *Front Microbiol* **13**, 847588 (2022).

30. M. Majumder, R. H. Johnson, V. Palanisamy, Fragile X-related protein family: A double-edged sword in neurodevelopmental disorders and cancer. *Crit Rev Biochem Mol Biol* **55**, 409 (2020).

31. F. A. Khan, N. Fang, W. Zhang, S. Ji, The multifaceted role of Fragile X-Related Protein 1 (FXR1) in cellular processes: an updated review on cancer and clinical applications. *Cell Death & Disease 2024 15:1* **15**, 1–16 (2024).

32. J. Y. Kang, *et al.*, LLPS of FXR1 drives spermiogenesis by activating translation of stored mRNAs. *Science (1979)* **377** (2022).

33. A. Agote-Aran, *et al.*, Spatial control of nucleoporin condensation by fragile X-related proteins. *EMBO J* **39** (2020).

34. A. Ramos, *et al.*, The structure of the N-terminal domain of the fragile X mental retardation protein: A platform for protein-protein interaction. *Structure* **14**, 21–31 (2006).

35. M. Li, *et al.*, LLPS of FXR proteins drives replication organelle clustering for β-coronaviral proliferation. *Journal of Cell Biology* **223** (2024).

36. Z. Hajikhezri, *et al.*, Fragile X-Related Protein FXR1 Controls Human Adenovirus Capsid mRNA Metabolism. *J Virol* **97** (2023).

37. J. Khlghatyan, *et al.*, Mental illnesses-associated Fxr1 and its negative regulator Gsk3b are modulators of anxiety and glutamatergic neurotransmission. *Front Mol Neurosci* **11** (2018).

38. Y. Zhang, *et al.*, The Fragile X Mental Retardation Syndrome protein interacts with novel homologs FXR1 and FXR2. *EMBO Journal* **14**, 5358–5366 (1995).

39. M. R. Akins, H. F. Leblanc, E. E. Stackpole, E. Chyung, J. R. Fallon, Systematic mapping of fragile X granules in the mouse brain reveals a potential role for presynaptic FMRP in sensorimotor functions. *Journal of Comparative Neurology* **520**, 3687–3706 (2012).

40. C. E. Bakker, *et al.*, Immunocytochemical and Biochemical Characterization of FMRP, FXR1P, and FXR2P in the Mouse. *Exp Cell Res* **258**, 162–170 (2000).

41. R. Soto-Acosta, *et al.*, Fragile X mental retardation protein is a Zika virus restriction factor that is antagonized by subgenomic flaviviral RNA. *Elife* **7** (2018).

42. J. A. Bornhorst, J. J. Falke, [16] Purification of Proteins Using Polyhistidine Affinity Tags. *Methods Enzymol* **326**, 245 (2000).

43. P. J. Wyatt, Light scattering and the absolute characterization of macromolecules. *Anal Chim Acta* **272**, 1–40 (1993).

44. J. Stetefeld, S. A. McKenna, T. R. Patel, Dynamic light scattering: a practical guide and applications in biomedical sciences. *Biophys Rev* **8**, 409–427 (2016).

45. A. K. Demeler, *et al.*, Integrative biophysical characterization of molecular interactions: A case study with the sfGFP–nanobody complex. *Anal Biochem* **703**, 115859 (2025).

46. B. Demeler, G. E. Gorbet, Analytical Ultracentrifugation Data Analysis with UltraScan-III. *Analytical Ultracentrifugation: Instrumentation, Software, and Applications* 119–143 (2016). https://doi.org/10.1007/978-4-431-55985-6_8.

47. E. Brookes, W. Cao, B. Demeler, A two-dimensional spectrum analysis for sedimentation velocity experiments of mixtures with heterogeneity in molecular weight and shape. *European Biophysics Journal* **39**, 405–414 (2010).

48. B. Demeler, K. E. Van Holde, Sedimentation velocity analysis of highly heterogeneous systems. *Anal Biochem* **335**, 279–288 (2004).

49. P. J. Fleming, K. G. Fleming, HullRad: Fast Calculations of Folded and Disordered Protein and Nucleic Acid Hydrodynamic Properties. *Biophys J* **114**, 856–869 (2018).

50. S. Tersteeg, T. Mrozowich, A. Henrickson, B. Demeler, T. R. Patel, Purification and characterization of inorganic pyrophosphatase for in vitro RNA transcription. *Biochem Cell Biol* **100**, 425–436 (2022).

51. R. F. Johnson, S. E. McCarthy, P. J. Godlewski, R. N. Harty, Ebola virus VP35-VP40 interaction is sufficient for packaging 3E-5E minigenome RNA into virus-like particles. *J Virol* **80**, 5135–5144 (2006).

52. T. Mrozowich, V. Meier-Stephenson, T. R. Patel, Microscale thermophoresis: warming up to a new biomolecular interaction technique. *Biochem (Lond)* **41**, 8–12 (2019).

53. M. Jerabek-Willemsen, *et al.*, MicroScale Thermophoresis: Interaction analysis and beyond. *J Mol Struct* **1077**, 101–113 (2014).

54. J. Jumper, *et al.*, Highly accurate protein structure prediction with AlphaFold. *Nature 2021 596:7873* **596**, 583–589 (2021).

55. A. Bhatwa, *et al.*, Challenges Associated With the Formation of Recombinant Protein Inclusion Bodies in Escherichia coli and Strategies to Address Them for Industrial Applications. *Front Bioeng Biotechnol* **9**, 630551 (2021).

56. G. Krainer, *et al.*, Reentrant liquid condensate phase of proteins is stabilized by hydrophobic and non-ionic interactions. *Nature Communications 2021 12:1* **12**, 1–14 (2021).

57. M. Edwards, M. Xu, S. Joseph, A simple procedure for bacterial expression and purification of the fragile X protein family. *Sci Rep* **10**, 15858 (2020).

58. M. N. Chowdhury, H. Jin, The RGG motif proteins: Interactions, functions, and regulations. *Wiley Interdiscip Rev RNA* **14**, e1748 (2022).

59. E. Bechara, *et al.*, Fragile X related protein 1 isoforms differentially modulate the affinity of fragile X mental retardation protein for G-quartet RNA structure. *Nucleic Acids Res* **35**, 299–306 (2007).

60. J. C. Darnell, C. E. Fraser, O. Mostovetsky, R. B. Darnell, Discrimination of common and unique RNA-binding activities among Fragile X mental retardation protein paralogs. *Hum Mol Genet* **18**, 3164–3177 (2009).

61. K. J. Zanotti, P. E. Lackey, G. L. Evans, M. R. Mihailescu, Thermodynamics of the fragile X mental retardation protein RGG box interactions with G quartet forming RNA. *Biochemistry* **45**, 8319–8330 (2006).

62. C. Schaeffer, *et al.*, The fragile X mental retardation protein binds specifically to its mRNA via a purine quartet motif. *EMBO J* **20**, 4803–4813 (2001).

63. A. Ramos, D. Hollingworth, A. Pastore, G-quartet-dependent recognition between the FMRP RGG box and RNA. *RNA* **9**, 1198–1207 (2003).

64. R. Valverde, L. Edwards, L. Regan, Structure and function of KH domains. *FEBS Journal* **275**, 2712–2726 (2008).

65. C. Di Primo, Surface Plasmon Resonance for Investigating Molecular Interactions with RNA. *Methods in Molecular Biology* **2113**, 73–88 (2020).

66. R. P. Sparks, J. L. Jenkins, R. Fratti, Use of Surface Plasmon Resonance (SPR) to Determine Binding Affinities and Kinetic Parameters Between Components Important in Fusion Machinery. *Methods Mol Biol* **1860**, 199 (2019).

67. D. H. Garvanska, *et al.*, SARS-CoV-2 hijacks fragile X mental retardation proteins for efficient infection. *bioRxiv* 2023.09.01.555899 (2023). https://doi.org/10.1101/2023.09.01.555899.

68. V. A. Golubeva, *et al.*, Network of Interactions between ZIKA Virus Non-Structural Proteins and Human Host Proteins. *Cells* **9**, 153 (2020).

Chapter 4: Conclusions

4.1- Overview

Through characterization of the interactions between the untranslated terminal regions (TRs) of the Zika Virus (ZIKV) and its genome, either through intramolecular or intermolecular interactions, during viral replication, we can gain a deeper insight into the mechanisms underlying the viral life cycle. During a time when we are more cognisant of the danger's viruses pose, flaviviruses like ZIKV have garnered increased attention due to past outbreaks, as well as the lack of an effective therapeutic or antiviral (1–5). While recent research has developed a foundation of how these TRs of ZIKV play a crucial role in viral replication, many of the interactions and processes that occur in relation to the TRs are poorly understood (6–8). My work aimed to investigate the interactions in which TRs participate, either with themselves or with host proteins, providing a further understanding of their role and potentially identifying a target for therapeutic development. Through the application of multiple biophysical techniques and assays, as well as cell culture studies, I have characterized the specificity of the cyclization interaction for ZIKV and established a method for the purification of fragile X-related protein 1 (FXR1), providing an initial basis for understanding the interaction.

Through the combination of biophysical techniques such as microscale thermophoresis and cell culturing replicon reporter assays, I have elucidated the specificity that the cyclization sequence confers (**Chapter 2**). Flaviviruses exhibit an intramolecular long-range RNA-RNA interaction between the TRs of their genome that is promoted through an 11-nucleotide sequence (9). Through this work, I have revealed that the cyclization sequence within ZIKV must be specific to the wild-type 11 nucleotides in order to promote the cyclization interaction. Through deletion and compensatory mutations, the interaction between the terminal regions was investigated *in*

vitro, where we demonstrated that only the wild-type TRs were capable of interacting. Further work in a cellular context using a replicon system showed that a mutation within the cyclization sequence was enough to drastically decrease viral replication. These results provide evidence that the cyclization interaction is sequence-specific within ZIKV, granting insight into a potential therapeutic target.

Focusing on the intermolecular interactions these TRs have during viral replication, I investigated the interaction between FXR1 and ZIKV TRs (**Chapter 3**). While ZIKV can produce viral proteins from its genome, the use of host proteins to aid in its replication is critical (8, 10). FXR1 has been identified to be essential for mRNA translational control and the formation of liquid-liquid phase separation condensates that regulate translation (11, 12). Interestingly, it has also been shown to promote viral replication through involvement in the formation of replication organelles within coronaviruses (13–15). Since FXR1 was identified through a pull-down assay as a potential interactor with ZIKV TRs, we wanted to investigate whether FXR1 similarly participates in ZIKV infection. Through recombinant protein expression, I was able to overexpress and purify a truncated form of FXR1($FXR1_{1\text{-}460}$). Using this purified $FXR1_{1\text{-}460}$, I found that $FXR1_{1\text{-}460}$ interacts with both TRs of ZIKV, though in what appears to be a non-specific manner. Although the interaction of $FXR1_{1\text{-}460}$ with poly(U) indicates less specificity for the TRs, other cellular factors could contribute to a higher specificity of FXR1 for the TRs. Further research is needed to clarify the interaction between FXR1 and ZIKV and to investigate the potential role of FXR1 during the replication process.

4.2- Future Directions

By establishing that the cyclization interaction is governed by a specific sequence, this creates a basis for future development of therapeutics aimed at targeting this sequence. Investigating the design of oligomers specific to those 11 nucleotides could be a promising approach. The binding of such oligomers to this sequence might inhibit the cyclization mechanism, thereby disrupting the virus's ability to regulate its transcription and translation, especially inhibiting transcription initiation. Previous research has explored how oligomers can suppress West Nile virus replication, another flavivirus, through binding to the cyclization sequence (16). Determining whether oligomers can similarly inhibit ZIKV replication would be significant in creating an antiviral strategy. Additional studies have shown that compensatory mutations can facilitate viral replication within cellular environments in other flaviviruses, such as Dengue and Kunjin virus (17, 18). Although these mutations enable replication, they do so at reduced efficiency. Further cloning of the ZIKV replicon systems to introduce compensatory mutations within the 3′ TR could reveal whether the lack of interaction observed *in vitro* can be overcome in a cellular context. This would further confirm the importance of sequence specificity in controlling the cyclization mechanism and could provide valuable insights for antiviral development.

While the initial interaction observed between $FXR1_{1-460}$ and the TRs of ZIKV suggested a non-specific interaction, additional methods could be used to better characterise this interaction. By applying other biophysical techniques such as surface plasmon resonance (SPR) or isothermal titration calorimetry, the binding affinity between $FXR1_{1-460}$ and the TRs of ZIKV can be examined (19–22). Both techniques allow the use of unlabelled molecules, ensuring that interaction analysis is not affected by fluorophore characteristics or artefacts of fluorophore movement. The use of SPR also enables the use of lower concentrations, limiting the aggregation observed with $FXR1_{1-}$

460. Small-angle X-ray scattering can be utilised as well, as it provides the ability to resolve low-resolution structures of interactions and facilitates the determination of binding orientation (23). Finally, to investigate the effects of FXR1 during viral replication in a cellular context, knockdowns can be performed. By examining the effects of FXR1 depletion on ZIKV replication, we can monitor replication efficiency and translation via replicon assays and assess transcription levels using qPCR. These cellular studies would help determine if FXR1 plays a crucial role in ZIKV replication, such as participating in the formation of replication organelles. Using these biophysical and cellular methods and assays would enhance our understanding of the implications FXR1 has during viral replication.

4.3- References

1. V. Sharma, *et al.*, Zika virus: An emerging challenge to public health worldwide. *Can J Microbiol* 66, 87–98 (2020).
2. B. H. Song, *et al.*, Comparison of Three Chimeric Zika Vaccine Prototypes Developed on the Genetic Background of the Clinically Proven Live-Attenuated Japanese Encephalitis Vaccine SA14-14-2. *Int J Mol Sci* 26 (2024).
3. R. Lowe, *et al.*, The zika virus epidemic in brazil: From discovery to future implications. *Int J Environ Res Public Health* 15 (2018).
4. M. V. Mancini, *et al.*, Evaluation of an Engineered Zika Virus-Like Particle Vaccine Candidate in a Mosquito-Mouse Transmission Model. *mSphere* 8 (2023).
5. M. A. McArthur, Zika Virus: Recent Advances towards the Development of Vaccines and Therapeutics. *Viruses* 9 (2017).
6. W. C. Ng, R. Soto-Acosta, S. S. Bradrick, M. A. Garcia-Blanco, E. E. Ooi, The 5′ and 3′ Untranslated Regions of the Flaviviral Genome. *Viruses* 9, 137 (2017).
7. C. S. Hahn, *et al.*, Conserved elements in the 3' untranslated region of flavivirus RNAs and potential cyclization sequences. *J Mol Biol* 198, 33–41 (1987).
8. M. A. Brinton, M. Basu, Functions of the 3′ and 5′ genome RNA regions of members of the genus Flavivirus. *Virus Res* 206, 108 (2015).
9. Z. Y. Liu, *et al.*, Viral RNA switch mediates the dynamic control of flavivirus replicase recruitment by genome cyclization. *Elife* 5 (2016).
10. D. L. Gemmill, *et al.*, The 3′ terminal region of Zika virus RNA contains a conserved G-quadruplex and is unfolded by human DDX17. *Biochemistry and Cell Biology* 102, 96–105 (2024).
11. J. Y. Kang, *et al.*, LLPS of FXR1 drives spermiogenesis by activating translation of stored mRNAs. *Science (1979)* 377 (2022).
12. A. Agote-Aran, *et al.*, Spatial control of nucleoporin condensation by fragile X-related proteins. *EMBO J* 39 (2020).
13. D. H. Garvanska, *et al.*, SARS-CoV-2 hijacks fragile X mental retardation proteins for efficient infection. *bioRxiv* 2023.09.01.555899 (2023). https://doi.org/10.1101/2023.09.01.555899.
14. Z. Hajikhezri, *et al.*, Fragile X-Related Protein FXR1 Controls Human Adenovirus Capsid mRNA Metabolism. *J Virol* 97 (2023).
15. M. Li, *et al.*, LLPS of FXR proteins drives replication organelle clustering for β-coronaviral proliferation. *Journal of Cell Biology* 223 (2024).

16. T. S. Deas, *et al.*, Inhibition of Flavivirus Infections by Antisense Oligomers Specifically Suppressing Viral Translation and RNA Replication. *J Virol* 79, 4599–4609 (2005).

17. A. A. Khromykh, H. Meka, K. J. Guyatt, E. G. Westaway, Essential Role of Cyclization Sequences in Flavivirus RNA Replication. *J Virol* 75, 6719 (2001).

18. W.-W. Chiu, R. M. Kinney, T. W. Dreher, Control of Translation by the 5′- and 3′-Terminal Regions of the Dengue Virus Genome. *J Virol* 79, 8303 (2005).

19. A. L. Feig, Review: Applications of isothermal titration calorimetry in RNA biochemistry and biophysics. *Biopolymers* 87, 293–301 (2007).

20. A. L. Feig, Studying RNA-RNA and RNA-Protein Interactions by Isothermal Titration Calorimetry. *Methods Enzymol* 468, 409 (2009).

21. C. Di Primo, Surface Plasmon Resonance for Investigating Molecular Interactions with RNA. *Methods in Molecular Biology* 2113, 73–88 (2020).

22. R. P. Sparks, J. L. Jenkins, R. Fratti, Use of Surface Plasmon Resonance (SPR) to Determine Binding Affinities and Kinetic Parameters Between Components Important in Fusion Machinery. *Methods Mol Biol* 1860, 199 (2019).

23. Y. Chen, L. Pollack, SAXS studies of RNA: structures, dynamics, and interactions with partners. *Wiley Interdiscip Rev RNA* 7, 512–526 (2016).